

Functional Van der Waals Heterostructures of Low-Dimensional Materials for High-Performance Sensors

By

© 2021

Mohammed Alamri

Submitted to the graduate degree program in Department of Physics and Astronomy and the Graduate Faculty of the University of Kansas in partial fulfillment of the requirements for the degree of Doctor of Philosophy.

Chair: Prof. Judy Wu

Prof. Philip Baringer

Prof. Hui Zhao

Dr. Wai-Lun Chan

Dr. Karen Nordheden

Date Defended: 03 / 23 /2021

The dissertation committee for Mohammed Alamri certifies that this
is the approved version of the following dissertation:

**Functional Van der Waals Heterostructures of Low-Dimensional
Materials for High-Performance Sensors**

Chair: Prof. Judy Wu

Date Approved: 04 / 15 /2021

Abstract

Low-dimensional materials including zero-dimensional (0D), one-dimensional nanomaterials (1D) nanomaterials, and two-dimensional (2D) materials, have become promising candidates for functional devices. The electronic states of these materials are confined for at least one dimension, like quantum dots (QD) for 0D, carbon nanotubes (CNT) for 1D, graphene and transitional metal dichalcogenides (TMDCs) for 2D. Due to the quantum confinement of the charge carriers as a result of reduced dimensionality, low-dimensional materials exhibit unique properties including ultrahigh carrier mobility, excellent optical transparency, and thermal conductivity which can be distinctively different from their bulk materials. This thesis explores new applications of vdWs heterostructures of low dimensional materials for various types of sensors, particularly biosensors, photodetectors, and gas sensors. First, we applied the graphene/MoS₂ heterostructure with plasmonic AuNPs on the top as substrates for surface-enhanced Raman spectroscopy (SERS). SERS enables single molecule through two enhancement mechanisms: electromagnetic (EM) enhancement and chemical enhancement (CM). Yet the microscopic mechanism of CM is still not well understood. Assembling the 2D heterostructures by stacking different 2D materials is an efficient approach for enhancing the Raman signals of adsorbed molecules. We demonstrated that the graphene/TMDCs heterostructure as an efficient substrate for SERS. Also, adding plasmonic AuNPs on top of the graphene/TMDCs heterostructure can further enhanced Raman signal due to EM enhancement. The interface dipole–dipole interaction in the heterostructure increases electron delocalization at the interface and increases the charge transfer probability between the Rhodamine 6G (R6G) molecule and the heterostructure which enhance the CM contribution to SERS signatures. R6G was used as an SERS probe molecule with a SERS sensitivity of 5×10^{-8} M using a nonresonance 633 nm laser, which is an order of magnitude higher than that reported on the

AuNPs/graphene substrate using the same excitation. A higher SERS sensitivity of 5×10^{-10} M was obtained using resonance 532 nm laser excitation.

Likewise, the 2D WS₂/graphene vdW heterostructure is a promising platform for photodetection. On account of the limited light absorption in atomically thin layered materials, hybrid structures or heterostructures based on 2D materials can be employed to enhance the light absorption and the photoresponsivity. 2D materials are necessary to overcome the limitations of conventional bulk materials for optoelectronics applications. Due to the limited light absorption in atomically thin layered materials, hybrid structures or heterostructures based on 2D materials can be employed to enhance the light absorption and the photoresponsivity. Combining the high carrier mobility of graphene with a strong light absorbing material, such as semiconductor quantum dots (QDs) or other 2D materials like TMDCs, offer complementary to graphene that lacks the light absorption. In this type of two different combined materials, the incident light produces electron-hole pairs in light-absorbers such as semiconductor TMDCs, with one of the two types of carriers transferred to graphene and another one trapped in the TMDCs layer and gate the graphene channel. The type of carrier transferred to graphene can recirculate many times from source to drain before recombining with the trapped carrier and hence produce ultrahigh gain and photoresponsivity. However, light absorption in TMDC/graphene vdW heterostructures is still limited due to the small thickness of the TMDC as the photosensitizer. We demonstrated a photodetector based on a plasmonic WS₂ nanodisks (NDs) with a lateral dimension of 200–400 nm on graphene vdW heterostructure. A strong localized surface plasmonic resonance (LSPR) can be generated in the WS₂-NDs upon light illumination, enabling significantly enhanced photoresponsivity as compared to the case of continuous 2D WS₂ layer. The photoresponsivity of 6.4 A/W on the WS₂-NDs/graphene photodetectors is about seven times higher than that (0.91

A/W) of the WS₂-CL/graphene vdW heterostructures at an incident 550 nm light intensity of 10 μW/cm².

Also, we combined this heterostructure (WS₂-NDs/graphene) with plasmonic AgNPs to enable not only superposition of the plasmonic effects from the WS₂-NDs and AgNPs, but also effective coupling of the plasmons and excitons in WS₂-NDs upon optical illumination. This leads to a high responsivity of 11.7 A/W on the graphene/WS₂ nanodisks/AgNP-metafilm under an incident illumination power of 5.5×10^{-8} W at 450 nm, which represents a 500% enhancement over that of the counterpart without the AgNP-metafilm.

Finally, we combined graphene with CNTs for gas sensing, and examined the effectiveness of the UV irradiation to improve the performance of the fabricated Pt/SWCNTs/graphene H₂ sensors. Due to their chemical properties and large surface area, carbon nanostructures (graphene and CNTs), are widely used in gas sensing. A colorless and inflammable hydrogen gas with a concentration of 4% in ambient air is potentially explosive. Therefore, designing a highly sensitive gas sensor has become a primary concern. Carbon nanostructures require a functionalization with platinum (Pt) because Pt can dissociate the H₂ molecules into H atoms to enhance the detection through the change in the electrical properties due to adsorption of H atoms. We developed a Pt-NPs/SWCNTs/graphene for H₂ gas sensor. Also, we demonstrated the effectiveness of the UV irradiation to enhance the performance of the fabricated Pt/SWCNTs/graphene H₂ sensors. The H₂ gas response was enhanced by up to 4.3 fold, together with an enhanced response speed by 3.6 times as compared to that of the as-made Pt-NPs/SWCNTs/Gr sensors before the UVC irradiation.

These results demonstrate that vdW heterostructures of low-dimensional materials are promising for scalable high-performance electronics applications.

Acknowledgements

First , I would like to express my deepest gratitude to my advisor, Distinguished Professor Judy Wu, for supervising me. Without her continuous guidance and suggestions, this thesis would have taken far longer to complete. She has been a great mentor for me since the first day I joined her group. I appreciate her continued support and guidance throughout the course of my research.

Many thanks also go to my Dissertation Committee: Prof. Philip Baringer, Prof. Hui Zhao, Dr. Wai-Lun Chan, and Dr. Karen Nordheden for their commitment to evaluate my work. I appreciate the time that they dedicated to reading my dissertation and providing helpful suggestions that supported me in improving my dissertation.

Thanks to my theoretical collaborators, Dr. Ridwan Sakidia and Dr. Seyed Sadeghi. They provided valuable simulations for my experimental work. Dr. Ridwan Sakidia assisted with calculating the electronic structure of the AuNPs/MoS₂/graphene 2D vdW heterostructure. Dr. Seyed Sadeghi helped by providing a simulation to calculate the electromagnetic field distribution around a AgNP in the graphene/WS₂-ND/AgNP-metofilm nanohybrid.

I would also like to thank my colleagues for their invaluable assistance and encouragement.

I am grateful to my wonderful parents, my wife, and my sisters and brothers for their continuous encouragement and support. I am also thankful to my spouse's parents for keeping me motivated during my PhD studies.

I extend my sincere gratitude to my excellent high school physics teacher, Omar, who inspired me to pursue this field. Also, I gratefully acknowledge Umm Al Qura University in Saudi Arabia for providing a full scholarship for my scientific profession. In addition, I acknowledge the additional financial support from the University of Kansas.

List of Publications

1. **Lateral graphene p-n junctions realized by nanoscale bipolar doping using surface electric dipoles and self-organized molecular anions**

Yong Zhang, Guangliang Hu, Maogang Gong, Mohammed Alamri, Chunrui Ma, Ming Liu, and Judy Z. Wu. *Advanced Materials Interfaces*, 6(1), 1801380

2. **High-sensitivity light detection via gate tuning of organometallic perovskite/PCBM bulk heterojunctions on ferroelectric $\text{Pb}_{0.92}\text{La}_{0.08}\text{Zr}_{0.52}\text{Ti}_{0.48}\text{O}_3$ gated graphene field effect transistors**

*Liping Wu, Liang Qin, Yong Zhang, Mohammed Alamri, Maogang Gong*Maogang Gong,* *ACS Appl. Mater. Interfaces* 2018, 10, 15,

3. **Scalable Graphene-on-Organometal Halide Perovskite Heterostructure Fabricated by Dry Transfer**

Liang Qin, Bhupal Kattel, Tika R. Kafle, Mohammed Alamri, Maogang Gong, Mohan Panth, Yanbing Hou, Judy Wu, and Wai-Lun Chan, *Advanced Materials Interfaces*, 6(1), 1801419

4. **Probing the relationship of cations-graphene interaction strength with self-organization behaviors of the anions at the interface between graphene and ionic liquids**

Guangliang Hu, Radhika S. Anareddy, Mohammed Alamri, Qingfeng Liu, Gaiind P. Pandey, Chunrui Ma, Ming Liu, Scott K. Shaw, Jun Li, and Judy Z. Wu. *Applied Surface Science* 479 (2019) 576–581

5. **Extraordinary Sensitivity of Surface-Enhanced Raman Spectroscopy of Molecules on MoS₂ (WS₂) Nanodomes/Graphene van der Waals Heterostructure Substrates**
Samar Ghopry, Mohammed Alamri, Ryan Goul, Ridwan Sakidja, and Judy Wu, Adv. Optical Mater. 2019, 1801249
6. **Plasmonic Au Nanoparticles on 2D MoS₂/graphene van der Waals Heterostructures for High-Sensitivity Surface Enhanced Raman Spectroscopy**
Mohammed Alamri, Ridwan Sakidja, Ryan Goul, Samar Ghopry, and Judy Z. Wu, ACS Appl. Nano Mater. 2019, 2, 3, 1412–1420
7. **Using Silver Nanoparticles Embedded Silica Metafilms as Substrates to Enhance Performance of Perovskite Photodetectors**
Bo Liu, Rithvik R. Gutha, Bhupal Kattel, Mohammed Alamri, Maogang Gong, Seyed M. Sadeghi, Wai-Lun Chan, and Judy Z. Wu. ACS Appl. Mater. Interfaces 2019, 11, 35, 32301–32309
8. **Plasmonic WS₂ Nanodiscs/Graphene van der Waals Heterostructure Photodetectors**
Mohammed Alamri, Maogang Gong, Brent Cook, Ryan Goul, and Judy Z. Wu, ACS Appl. Mater. Interfaces 2019, 11, 36, 33390–33398
9. **Localized Surface Plasmon Resonance Enhanced Light Absorption in AuCu/CsPbCl₃ Core/Shell Nanocrystals**
Maogang Gong, Mohammed Alamri, Dan Ewing, Seyed Sadeghi, and Judy Wu, Advanced Materials, 2020, 2002163.
10. **Au Nanoparticle/WS₂ Nanodome/Graphene van der Waals Heterostructure Substrates for Surface-Enhanced Raman Spectroscopy**

Samar Ghopry, Mohammed Alamri, Ryan Goul, Brent Cook, Seyed Sadeghi, Rithvik R. Gutha, Ridwan Sakidja, and Judy Z. Wu. ACS Appl. Nano Mater. 2020, 3, 3, 2354–2363

11. Cation- π Interaction Assisted Molecule Attachment and Photocarrier Transfer in Rhodamine/Graphene Heterostructures

Bo Liu, Luis E. López-González, Mohammed Alamri, Enrique F. Velázquez-Contrera, Hisila Santacruz-Ortega, and Judy Z. Wu. Advanced Materials Interfaces, 2020, 7.16: 2000796

12. Enhanced Photoresponse of WS₂ Nano Disc/graphene van der Waals Heterostructures on Plasmonic Ag Nanoparticles-Embedded Silica Metafilms

Mohammed Alamri, Bo Liu, Seyed M. Sadeghi, Dan Ewing, Amy Wilson, Jennifer L. Doolin, Cindy L. Berrie, and Judy Wu, ACS Appl. Nano Mater. 2020, 3, 8, 7858–7868

13. Zinc Oxide Nanowire Array/Graphene Nanohybrid on a Flexible PET Substrate for Static and Dynamic Piezoelectric Strain Sensing

Mohan Panth, Brent Cook, Mohammed Alamri, Dan Ewing, Amy Wilson, and Judy Z. Wu, ACS Omega 2020, 5, 42, 27359–27367

14. Development of ALD-Pt@ SWCNT/graphene 3D nanohybrid architecture for hydrogen sensing

Bo Liu, Mohammed Alamri, Michael Walsh, Jennifer L. Doolin, Cindy L. Berrie, and Judy Z. Wu, ACS Appl. Mater. Interfaces 2020, 12, 47, 53115–53124

15. Intermixed WS₂+MoS₂ Nanodisks/Graphene van der Waals Heterostructures for Surface-Enhanced Raman Spectroscopy Sensing

Samar Ghopry, Seyed Sadeghi, Yasmine Farhat, Cindy Berrie, Mohammed Alamri, and Judy Wu. ACS Appl. Nano Mater. 2021, 4, 3, 2941–2951

16. Ultraviolet-activation improved H₂ gas sensing using ALD Pt decorated 3D carbon nanostructures

Mohammed Alamri, Bo Liu, Michael Walsh, Jennifer L. Doolin, Cindy L. Berrie and Judy Z. Wu. under review

Table of Contents

Chapter 1: Introduction	1
1.1 Overview of Low-Dimensional Materials	1
1.2 Graphene	2
1.3 Carbon Nanotubes (CNTs)	5
1.4 Transition Metal Dichalcogenides (TMDCs)	8
1.5 Van der Waals (vdW) heterostructures of low-dimensional materials	9
1.6 Plasmonic nanostructures.....	11
1.7 Remaining Critical Issues and Motivation of his Thesis	14
2 Chapter 2: Experiment	16
2.1 Materials Synthesis and Characterization	16
2.1.1 Graphene	16
2.1.2 Transition Metal Dichalcogenides (TMDCs)	18
2.1.3 Carbon Nanotube (CNTs).....	20
2.2 Devices Fabrication and Characterization:	21
2.2.1 The SERS MoS ₂ /graphene 2D vdW Heterostructure Substrate	21
2.2.2 The WS ₂ -NDs/graphene photodetector.....	23
2.2.3 The WS ₂ -NDs/graphene/AgNPs-metafilm photodetector	25
2.2.4 Atomic layer deposition (ALD) Pt-NPs @ SWCNTs/graphene H ₂ Gas Sensor	

2.3	Simulation	36
2.3.1	The Density Function Theory (DFT) simulation	36
2.3.2	Finite difference time-domain (FDTD) simulation.....	37
3	Chapter 3: Plasmonic Au Nanoparticles on MoS₂/graphene for Surface Enhanced Raman Spectroscopy	38
3.1	Background and mechanism	38
3.2	Current research on SERS	39
3.3	Plasmonic Au Nanoparticles on 2D MoS ₂ /Graphene vdW Heterostructures.....	41
3.3.1	Results and Discussions.....	42
3.3.2	Conclusion	55
4	Chapter 4: WS₂ Nanodisks /Graphene van der Waals Heterostructure Photodetectors	57
4.1	Photodetection background.....	57
4.1.1	Photodetection mechanism	57
4.2	2D materials and their heterostructures for photodetection.....	58
4.3	WS ₂ Nanodisks /Graphene van der Waals Heterostructure Photodetectors	60
4.3.1	Results and Discussions.....	60
4.3.2	Conclusion	70
5	Chapter 5: WS₂ Nano Disk/Graphene on plasmonic Ag Nanoparticles for Photodetection	72

5.1	Strategies to enhance light-matter interaction in the 2D materials for optoelectronic applications	72
5.2	WS ₂ Nano Disk/Graphene on plasmonic Ag Nanoparticles for Photodetection	76
5.2.1	Results and Discussions	76
5.2.2	Conclusion	86
6	Chapter 6: Enhanced H₂ sensitivity in ultraviolet-activated Pt nanoparticle/SWCNT /graphene nanohybrids.....	88
6.1	An Overview of Carbon nanostructure-based gas sensor	88
6.2	Ultraviolet-activation improved H ₂ gas sensing using ALD Pt decorated 3D carbon nanostructures	89
6.2.1	Results and Discussions	90
6.2.2	Conclusion	101
7	Chapter 7: Conclusions and future perspectives	103
8	References	106

List of Figures

Figure 1.2.1 (a) Graphene can be wrapped up into 0D-buckyball, rolled into 1D-carbon nanotube, or stacked into 3D-graphit [5]. (b) Bonding in graphene Sigma bond and pi bond formed by sp^2 hybridization. (c) The lattice structure of graphene. (d) Corresponding Brillouin zone. (e) Electronic dispersion in the honeycomb lattice [5]..... 3

Figure 1.2.2 (a) Ambipolar electric field effect in single-layer graphene [4]. The insets show its conical low-energy spectrum $E(k)$. (b) Light transmission as a function of the number of graphene layers [3]. (c) Intraband and interband transitions in graphene. 5

Figure 1.3.1 Graphene rolled up to form different types of SWCNT, armshair, zigzag, and chiral [10]..... 7

Figure 1.4.1 (a) Crystal structure of a single-layer TMDC. (b) Real-space representation of an exciton in 2D TMDC monolayer, ϵ_{2D} dielectric constants and the ϵ_0 vacuum permittivity. (c) Band structures of bulk and monolayer of MoS_2 [16]..... 9

Figure 1.5.1 (a) Concept of building 2D heterostructures as analogous to Lego Block [20]. (b) Schematic of band alignment of type-II of typical MoX_2/WX_2 heterostructure. 11

Figure 1.6.1 (a) Schematics of the EM field of surface plasmons propagating along at a metal and dielectric interface. (b) Schematic of a localized surface plasmon of a metal nanoparticle illustrating the displacement of the electron charge cloud relative to the nuclei..... 13

Figure 2.1.1 (a) Graphene growth on the Cu using the CVD method. (b) Temperature and gas flow rate profiles used for the graphene growth as a function of the processing time..... 17

Figure 2.1.2 Schematic illustration of the wet transfer process of graphene from Cu to SiO_2/Si . 18

Figure 2.1.3 Schematic of TMDCs growth using the CVD..... 19

Figure 2.1.4 Schematic of the CNT thin film preparation process using the filtration method.... 20

Figure 2.2.1 (a) Optical image and (b) Raman spectra of the MoS₂/ graphene and, (c) SEM of AuNPs on the MoS₂/graphene substrate. 23

Figure 2.2.2 (a) Optical image of WS₂-NDs/graphene; (b) Raman spectra of WS₂-CL (black), and WS₂-ND (red) on graphene; (c) Raman spectra of graphene with WS₂-NDs (red), with a WS₂-CL (black), and without WS₂ (green). (d) 10x10 μm² Raman mapping images for the E¹_{2g} peak of WS₂-NDs. The dashed square in (a) is the area used for the Raman map of WS₂-NDs; (e) Height profile of WS₂-NDs. Inset: AFM image of WS₂-NDs. (f) A 3D image for a WS₂-ND with thickness of ~ 5 nm and lateral dimension of ~ 200 nm. 25

Figure 2.2.3 Schematic illustration of the graphene/WS₂-NDs/AgNP-metafilm heterostructure device fabrication process: (a) stacking PMMA/graphene on pre-grown WS₂-NDs on SiO₂/Si substrate; (b) etching SiO₂ using diluted HF acid; (c) lift off the PMMA/graphene/WS₂-NDs; (d) transferring the PMMA/graphene/WS₂-NDs to SiO₂/Si with pre-deposited AgNPs-metafilm between the Au electrodes; and (e) completing the graphene/WS₂-NDs/AgNP-metafilm heterostructures device after removal of PMMA. Inset shows a zoom-in view of the device cross section with a WS₂-ND on top of 20 nm thick SiO₂ spacer over an AgNP. 27

Figure 2.2.4 UV-vis absorption spectra of AgNPs-metafilm before (solid line) and after (dashed line) exposure to the sulfur vapor at 450 °C for 1 hour. 28

Figure 2.2.5 (a) Optical and (b) Raman image of WS₂-NDs (c) Height profile of WS₂-NDs. Inset: AFM image of WS₂-NDs. (d) Raman spectra of graphene on SiO₂/Si (black) and graphene on SiO₂/Si with AgNPs-metafilm (green). 31

Figure 2.2.6 (a) UV-vis absorption spectra of AgNPs-metafilm (blue) and graphene/WS₂-NDs (green), and graphene/WS₂-NDs/AgNPs-metafilm (purple). (b) SEM image of the AgNPs (c) The 1.0 μm × 1.0 μm area AFM image of SiO₂(20 nm)/AgNPs. 32

Figure 2.2.7 (a-c) Schematic illustration of the ALD Pt-NPs @ SWCNT/Gr H ₂ gas sensor fabrication process. The yellow spheres represent the ALD Pt-NPs formed on the 3D SWCNTs/Gr heterostructure electrode. The inset illustrates the conformal coating of SWCNTs with PtNPs (d) The fabricated device irradiated with UVC.	34
Figure 2.2.8 (a) Raman spectra of the grahene (blue) and SWCNTs (red), respectively. Inset shows RBM peak of the SWCNTs. (b) SEM image of an Pt-NPs/SWCNTs/Gr sensor. (c) 5 μm x 5 μm AFM image of Pt-NPs/SWCNTs/Gr sensor. (d) EDS spectrum of 20C Pt on SWCNTs.	36
Figure 3.1.1 Jablonski diagrams illustrating (a) the Rayleigh and (b-c) Raman scattering processes.	39
Figure 3.3.1 (a) The atomic layer stacks of Au/MoS ₂ hybrid heterostructures with different numbers of Au layers of 1L, 3L, 5L and 6L on monolayer MoS ₂ . The interface distance between the two materials is also illustrated. The atomic layer stacks of 2L Au/ The atomic la atomic layer stacks of 2L Au/2L MoS ₂ hybrid heterostructures (b) without graphene layer, and (c) with graphene layer.	44
Figure 3.3.2 The 3D ELF plots of the same hybrid AuNP/ MoS ₂ heterostructures shown in Figure 3.3.1a.	45
Figure 3.3.3 Comparison on the local DOS of Au atoms for (a) 1L, (b) 2L from the different types of occupied d orbitals, namely d _{xy} , d _{xz} , d _{yz} , d _z ² is minimally occupied. The total DOS and each atom-specific contribution for 1L is also shown in (c) The zero point for the energy range is Fermi Energy E _{Fermi}	47
Figure 3.3.4 (a) Vertical MoS ₂ /graphene bilayer heterostructure. (b) Electron Localization Function (ELF) of the MoS ₂ /graphene vdW heterostructure.	48

Figure 3.3.5 (a) Optical transmittance spectra of multiple materials on fused silica. (a) AuNPs/MoS ₂ /graphene, (b) graphene, and (c) MoS ₂ /graphene.....	49
Figure 3.3.6 R6G Raman spectra of 5x10 ⁻⁵ M concentration with different substrates: AuNPs/MoS ₂ /graphene (purple), AuNPs/graphene (green), MoS ₂ /graphene (blue), graphene(red), and MoS ₂ (black).	50
Figure 3.3.7 Raman spectra of the R6G taken by the 633 nm laser with different laser powers (0.05 mW to 10mW).	51
Figure 3.3.8 Raman spectra of the R6G molecules with different concentrations cast on the AuNPs/MoS ₂ /graphene hybrid using (a) 633 nm laser and (b) 532 laser. Spectra of concentrations 5x10 ⁻⁹ M and 5x10 ⁻¹⁰ M were multiplied by factor of 3.	53
Figure 3.3.9 Raman spectra of the R6G molecules with different concentrations cast on the AuNPs/MoS ₂ hybrid using (a) 532 laser. Spectra of concentrations 5x10 ⁻⁸ M and 5x10 ⁻⁹ M were multiplied by factor of 5. (b) 633 nm laser.	54
Figure 3.3.10 The intensities of the Raman peaks as a function of the R6G concentrations. at (a,d) 612 cm ⁻¹ , (b,e) 769 cm ⁻¹ , and (c,f) 1184 cm ⁻¹ for the AuNPs/MoS ₂ /graphene substrates using both 633 nm laser (red) and 532 nm laser (green). (d, e, f) was plotted using a logarithmic scale.	55
Figure 4.3.1 (a) Schematic illustration of the photodetector based on WS ₂ -NDs/graphene vdW heterostructure. (b) A zoom-in view of the WS ₂ -NDs/graphene photodetector with an illustration of the charge transfer process at the vdW interface. (c) Electron band diagram of p doped graphene and the WS ₂ -NDs (E _f : the Fermi level, CB: conduction band, and VB: valence band).	62
Figure 4.3.2 (a) I–V characteristics measured in the dark and upon 550 nm illumination at V _{sd} = 0-6 V. (b) Photoresponse of the device at various bias voltages under various incident optical	

power. (c) Dynamic photocurrent measured in response to 550 nm light ON and OFF for WS₂-NDs/graphene photodetector. (d) The enlarged part of (c)..... 63

Figure 4.3.3 (a,c,e) Optical and (b,d,f) Raman mapping images of WS₂ with smaller and denser WS₂-NDs in WS₂-NDs/graphene (orange); larger and more dilute WS₂-NDs WS₂-NDs/graphene (purple) samples, and WS₂-CL/graphene (blue). (g) The corresponding dynamic photocurrents measured in response to 550 nm light on and off and (h) photoresponsivity as a function of the incident light intensity on the three devices..... 65

Figure 4.3.4 Photoresponsivity and photocurrent as a function of the incident light intensity of (a) the WS₂-NDs/graphene heterostructure photodetector; and (b) WS₂-CLs/graphene photodetector. (c) The dynamic photoresponse of the WS₂-NDs/graphene heterostructure photodetector (red) and WS₂-CLs/graphene photodetector (black) measured in response to 550 nm. (d) Spectral photoresponsivity of the WS₂-NDs /graphene photodetector (red) and WS₂-CLs /graphene photodetector (black). 67

Figure 4.3.5 (a) Dynamic photoresponse of the WS₂-NDs/graphene heterostructure photodetector measured in response to 550 nm light on and off with different incident light powers; (b) The Detectivity and the EQE as a function of the incident light intensity..... 69

Figure 5.1.1 (a) QD/graphene hybrid and (b) TMDCs /graphene vdW) heterostructures [114]. (c) Scanning photovoltage maps for excitations at 785 nm [120] (d) Spectral response of graphene device integrated with a Micro-optical-cavity [127]. 75

Figure 5.2.1 Dynamic photocurrent in response to light on/off with three incident light wavelengths of: 650 nm (red), 550 nm (green), and 450 nm (blue). 78

Figure 5.2.2 (a) Photocurrent response of the photodetectors with (red) and without (black) AgNPs-metafilm at 450 nm and light intensity of 0.15 mW/cm² under 0.8V bias. (b)

Photoresponsivity as a function of wavelength for graphene/WS₂-NDs photodetector photodetectors with (red) and without (black) the AgNPs-metafilm. The source-drain bias voltage was 0.8V for both devices..... 80

Figure 5.2.3 (a) photoresponsivity of graphene/WS₂-NDs photodetectors with (red) and without (blue) the AgNPs-metafilm at different intensities of the 450 nm illumination. The source-drain bias was 0.8 V. (b) Photoresponsivity enhancement as a function of light intensity. (c) Photocurrent enhancement as a function of wavelength. (d) The measured external quantum efficiency (EQE) and detectivity D^* as a function of the wavelength under $V_{sd} = 0.8V$ 82

Figure 5.2.4 Photoresponsivity of graphene/WS₂-NDs/AgNPs-metafilm nanohybrid photodetectors at different irradiated power and different bias voltages, $\lambda=450$ nm. 83

Figure 5.2.5 (a) Diagram of the structure adopted for FDTD simulations of plasmonic response of the AgNP. The AgNP (semisphere) has the radius of r and embedded on SiO₂. The thin layer on the top with thickness of $D=6$ nm represents the WS₂-ND and graphene. (b) Absorption cross section of the structure shown in (a) for different radius values of 10,20,40, and 60 nm of the AgNP, r (legends in nm). 85

Figure 5.2.6 FDTD simulated electromagnetic field mode profiles of a AgNP with $r = 60$ nm (a, b) and 10 nm (c). 86

Figure 6.2.1 (a) The normalized dynamic H₂ response (responsivity (UV/pristine)) of the Pt-NPs/SWCNTs/graphene gas sensor as function of UV light exposure at room temperature before (black) and after UV irradiation for different time of 2, 5, 10, 15, and 20 minutes. (b) The maximum response (blue) and response time as a function of UV light exposure time..... 92

Figure 6.2.2 (a-b) Sensitivity of Pt-NPs @ SWCNTs/graphene H₂ gas sensor as a function of the H₂ concentration ranging from 1% to 10%..... 93

Figure 6.2.3 (a) Dynamic H₂ Response of the Pt-NPs/SWCNTs/Gr gas sensor as function of UV light exposure at room temperature before (black) and after UV irradiation for different time of 2, 5, 10, 15, and 20 minutes. 94

Figure 6.2.4 Raman spectra of (a) SWCNT film and (b) graphene after different UVC irradiation for different periods of 2, 5, 10, 15 and 20 minutes. (c) The I_D/I_G ratio as function of the UVC irradiation time on SWCNTs (d) The I_{2D}/I_G (red) and I_D/I_G (blue) ratio as function of the UVC irradiation time on graphene. 97

Figure 6.2.5 Schematic illustration of photo-activated desorption of residual molecules, such as O₂ and H₂O, molecules from the SWCNTs and graphene with (a) zero (b) less than 10 minutes, and (c) more than 10 minutes of the UVC irradiation. In the case (c), oxidation of SWCNTs and graphene is illustrated with defects formation and oxygen (red spheres) binding to SWCNTs and graphene. 99

Figure 6.2.6 (a) XPS spectra taken on SWCNT/graphene samples without (black) and with (red) UV irradiation treatment. (b) and (c) are C 1s peak high-resolution scan on the two SWCNT/graphene samples Red dashed lines represent the fitted C1s peaks, and the C 1s peak 101

List of Tables

Table 1 Comparison of the performance of photodetectors composed of graphene, 2D TMDC layers and their heterostructures.	70
---	----

Chapter 1: Introduction

1.1 Overview of Low-Dimensional Materials

Low-dimensional materials, including zero-dimensional (0D) like quantum dots (QDs), one-dimensional (1D), as carbon nanotubes (CNTs), and two-dimensional (2D) nanomaterials, such as graphene, have attracted international attention. This is due to their outstanding properties and great potential in a wide range of applications such as optoelectronics and electronics devices. Graphene and CNTs are the most well-known examples of carbon nanostructured materials. Graphene, a single layer of sp^2 bonded carbon atoms arranged in a hexagonal lattice, was discovered in 2004 by Geim and Novoselov. It has numerous unique properties such as large surface-to-volume ratio and excellent electrical, and thermal conductivity. Almost like graphene, CNTs also possess outstanding electrical, mechanical, thermal properties. However, commonly, graphene has some advantages over CNTs. For instance, graphene has higher electrical conductivity (up to 3 times) [1, 2] and a larger specific surface area than CNTs. CNTs are primarily classified as single-wall carbon nanotubes (SWCNTs) and multi-wall carbon nanotubes (MWCNTs) because they were discovered a decade before graphene discovery [3]. Later on, the large family of 2D materials has grown significantly after the discovery of graphene. Among the 2D materials are the transition metal dichalcogenides (TMDCs) that have become one of the most interesting 2D materials. Their in-plane atoms are held together by strong chemical bonds whereas the out-plane layers held by weak van der Waals (vdW) forces enable the exfoliation of a monolayer or a few layers. Each monolayer of the TMDCs layers is comprised of transition metal atoms sandwiched between two layers of chalcogen atoms (M-X-M). These atoms have a strong covalent bond between them, while the adjacent layers are weakly held together by van der Waals forces. TMDCs with sizable band gaps are complementary to the zero-bandgap graphene. Bulk

(3D) TMDCs transform from indirect-bandgaps to direct-bandgaps in their single layer (2D) and that enhances the quantum confinement and reduced dielectric screening [4]. Other properties of the low dimensional materials will be discussed in following sections.

1.2 Graphene

Graphene is a single layer of carbon atoms arranged in a honeycomb crystal lattice. It can be stacked into 3D graphite, rolled into 1D-carbon-nanotube, or wrapped into 0-D buckyballs (C60), Figure 1.2.1a. The π -bonds are responsible for a weak van der Waals interaction between graphene layers in graphite and the high electrical and thermal conductivity of graphene. The strong in-plane σ bonds are responsible for the excellent mechanical properties of graphene Figure 1.2.1b. A single layer of graphene forms a 2D hexagonal crystal lattice with a primitive cell containing a triangular lattice with a basis of two inequivalent carbon atoms, A and B, per unit cell. The lattice structure and first Brillouin zone of graphene is shown in Figure 1.2.1c-e.

The lattice vectors are given by [1]

$$\vec{a}_1 = \frac{a}{2}(3, \sqrt{3}) \quad , \quad \vec{a}_2 = \frac{a}{2}(3, -\sqrt{3}) \quad (1)$$

Where $a = 1.42 \text{ \AA}$ is the carbon-carbon distance and the reciprocal-lattice vectors are given by

$$\vec{b}_1 = \frac{2\pi}{3a}(3, \sqrt{3}) \quad , \quad \vec{b}_2 = \frac{2\pi}{3a}(3, -\sqrt{3}) \quad (2)$$

The positions in momentum space of the two points (Dirac points) K and K' at the corners of the graphene Brillouin zone (BZ) are given by

$$\vec{K} = \left(\frac{2\pi}{3a}, \frac{2\pi}{3\sqrt{3}a} \right) \quad , \quad \vec{K}' = \left(\frac{2\pi}{3a}, -\frac{2\pi}{3\sqrt{3}a} \right) \quad (3)$$

The three nearest-neighbor vectors in real space are given by

$$\vec{\delta}_1 = \frac{a}{2}(1, \sqrt{3}), \quad \vec{\delta}_2 = \frac{a}{2}(1, -\sqrt{3}), \quad \vec{\delta}_3 = -a(1,0) \quad (4)$$

The dispersion relation is linear at the six corners of BZ, which leads to zero effective mass for carriers where they behave like relativistic particles described by the Dirac-like Hamiltonian while the carriers in semiconductors or metals obey the Schrödinger equation [1].

$$\hat{H} = \hbar v_F \begin{pmatrix} 0 & k_x - ik_y \\ k_x + ik_y & 0 \end{pmatrix} = \hbar v_F \vec{\sigma} \vec{k} \quad (5)$$

where \vec{k} is the quasiparticle momentum, $\vec{\sigma}$ the 2D Pauli matrix, v_F is the Fermi velocity, and \hbar is Planck's constant.

That means the charge carriers' mobility in graphene are extremely high ($\sim 200,000 \text{ cm}^2 \text{ V}^{-1} \text{ s}^{-1}$) [2]. Therefore, graphene is an excellent material for communication and for high-frequency circuits applications. However, the absence of band gap limits its applications in optoelectronics.

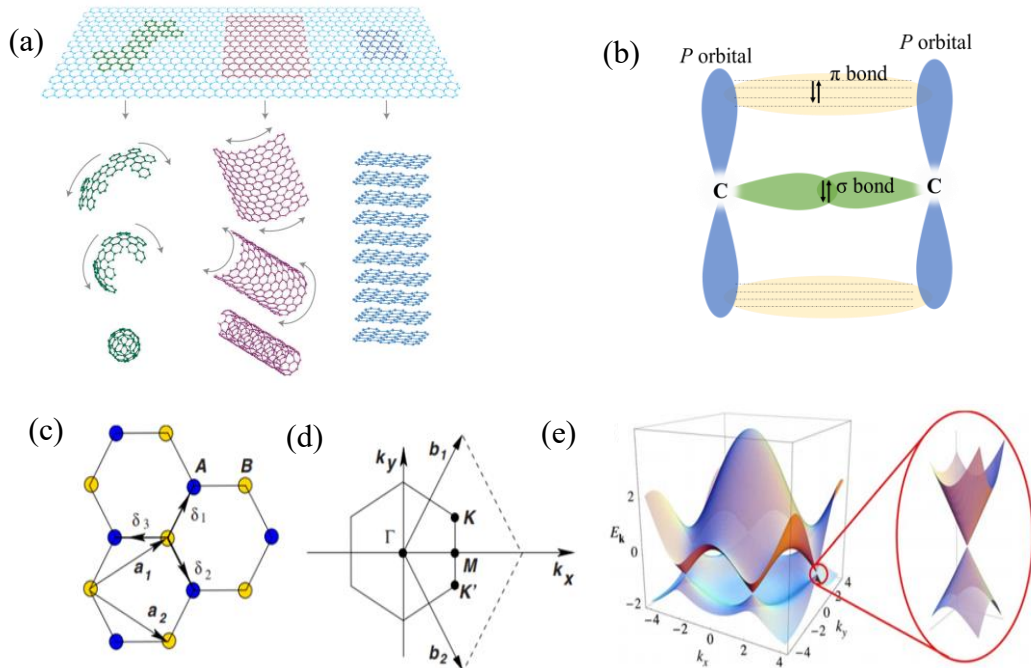


Figure 1.2.1 (a) Graphene can be wrapped up into 0D-buckyball, rolled into 1D-carbon nanotube, or stacked into 3D-graphit [5]. (b) Bonding in graphene Sigma bond and pi bond formed by sp^2 hybridization. (c) The lattice structure of graphene. (d) Corresponding Brillouin zone. (e) Electronic dispersion in the honeycomb lattice [5].

Graphene has the ambipolar field effect, i.e. doping of charge carriers can be obtained via application of a positive (or negative) gate field to induce hole (or electron) doping. For intrinsic graphene, the Fermi level is located at the Dirac point, however, this Fermi level can be tuned by applying a vertical electric field to a graphene field-effect transistor (GFET) as shown in Figure 1.2.2a. Carriers in graphene (Dirac fermion) have a ballistic transport with average free path up to 1 μm [5]. The conductivity (σ) in graphene depends on carrier mobility (μ) and their density (n) as described by equation (6):

$$\sigma = ne\mu \quad (6)$$

Where μ is charge carrier mobility, n is charge carrier density, and e is the elementary charge.

As a result of the the unique electronic structure, a monolayer of graphene can absorb about 2.3% of incident white light Figure 1.2.2b. Its optical transmittance T and reflectance R are given by,

$$T = (1 + \frac{1}{2} \pi\alpha)^{-2} \quad \text{and} \quad R = \frac{1}{4} \pi^2 \alpha^2 T \quad \text{for the normal light incidence with a negligible}$$

reflectance ($<0.1\%$). Its transparency depends only on the fine-structure constant $\alpha = \frac{e^2}{\hbar c} = 1/137$

(c , speed of light) [3]. Two transition processes are responsible for the optical absorption in graphene, the intraband (free-carrier) and interband transitions in Figure 1.2.2c. In the far-infrared, the intraband transition is dominated while interband transition contributes to the absorption from mid-infrared to ultraviolet [6]. The intraband absorption is enhanced by tuning the holes or the electrons concentration in graphene. However, the interband absorption that originates from the transitions between the valence and conduction bands, occurs when the photon energy ($\hbar\omega$) is larger than twice the graphene Fermi level $2E_F$ [6]. Therefore, the interband transition is forbidden when the photon energy is less than $2E_F$ due to Pauli blocking.

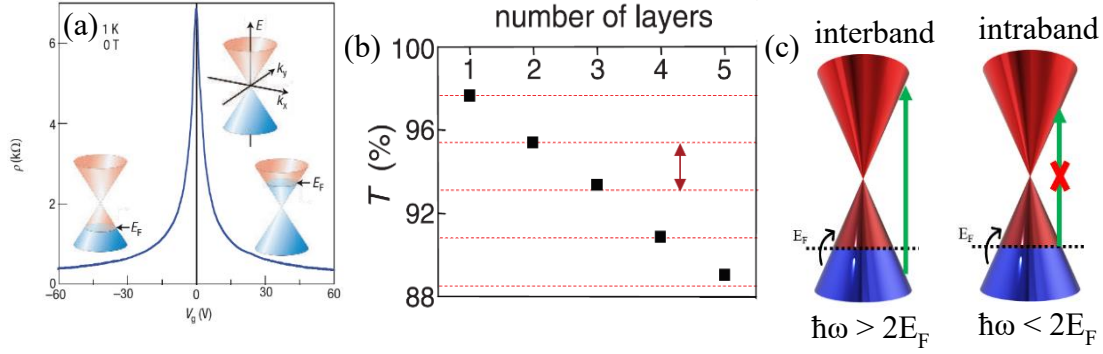


Figure 1.2.2 (a) Ambipolar electric field effect in single-layer graphene [4]. The insets show its conical low-energy spectrum $E(k)$. (b) Light transmission as a function of the number of graphene layers [3]. (c) Intraband and interband transitions in graphene.

Carbon atoms in graphene are held together by the covalent σ bonds (the strongest chemical bonds). From measurements taken, graphene has a breaking stress 200 times greater than steel, with a 2D a breaking strength of 340 N/m (Young's modulus about 1000 GPa) [7]. It possesses an extremely high thermal conductivity as result of these strong covalent σ bonds. Thermal conductivity of freely suspended graphene at room temperature can reach up to 5000 W/mK. However, this value could be decreased to ~ 600 W/mK for graphene supported by SiO_2 due to phonon leakage across the graphene substrate interface [8].

1.3 Carbon Nanotubes (CNTs)

A single-walled carbon nanotube (SWCNT) is a rolled-up sheet of graphene. CNTs are either metallic or semiconducting depending on the diameter and chirality (the rolling angle), the armchair forms metallic CNTs, whereas chiral or zigzag make a semiconductor CNTs [9]. This chirality has a strong influence on the CNTs electronic properties. The chiral vector is represented by a pair of indices, (n,m) , where these two integers correspond to the number of unit vectors along the two directions in the honeycomb crystal lattice of graphene. When $n=0$ the nanotube is called

“zigzag”, when $n=m$ the nanotube is called “armchair”, and all other states are chiral as shown in Figure 1.3.1 [10]. The typical diameter of the CNTs is 1-5 nm with the length up to several hundred microns. The diameter of a CNT can be determined by

$$d = \frac{a\sqrt{n^2+nm+m^2}}{\pi} \quad (8)$$

where $a = 1.42\sqrt{3}$ (the lattice constant).

CNTs have extraordinary mechanical properties due the strength of the carbon-carbon bonds. They are one of the strongest and stiffest known materials. Numerous experimental and theoretical studies have been reported to determine the mechanical properties of CNTs. For example, the Young’s modulus of CNTs is in the range of 1 TPa, which is approximately five times higher than that of steel, and their strength is as high as 170 GPa [11, 12]. Besides the excellent mechanical properties, CNTs possess exceptional electrical and thermal conductivity. At room temperature, the resistivity in the individual SWCNT can be as low as $10^{-6} \Omega \text{ cm}^{-1}$, which exceeds conventional conductive metals. The lower resistivity of $5 \times 10^{-6} \Omega \text{ cm}^{-1}$ was reported for MWCNT due to the larger diameters than SWCNTs [13]. The intrinsic mobility of semiconductor CNTs can exceed $1 \times 10^5 \text{ cm}^2 \text{ V}^{-1} \text{ s}^{-1}$ at room temperature. The commonly observed mobilities for a metallic nanotube is in the range of $\mu = 1-5 \times 10^4 \text{ cm}^2 \text{ V}^{-1} \text{ s}^{-1}$ for tube diameters of 1 - 5 nm [14]. Electrically, CNTs behave as either a metal or a semiconductor depending on the type of CNTs. 1/3 of the nanotubes are metallic and 2/3 are semiconducting depending on their indices (n, m). For instance, armchair ($n=m$) tubes are always metallic, and the others are semiconductors with different widths of bandgaps depending on the tube diameter. Semiconducting CNTs have a bandgap that is inversely proportional to the CNT diameter ($E_g = 1/d$). Therefore, some types of CNTs have conductivities higher than that of copper.

Also, extremely high thermal conductivity of 6600 W/m K has been predicted for CNTs at room temperature [15] which is comparable to the thermal conductivity of a hypothetical isolated graphene monolayer and much larger than thermal conductivity of copper (~ 400 W/m K).

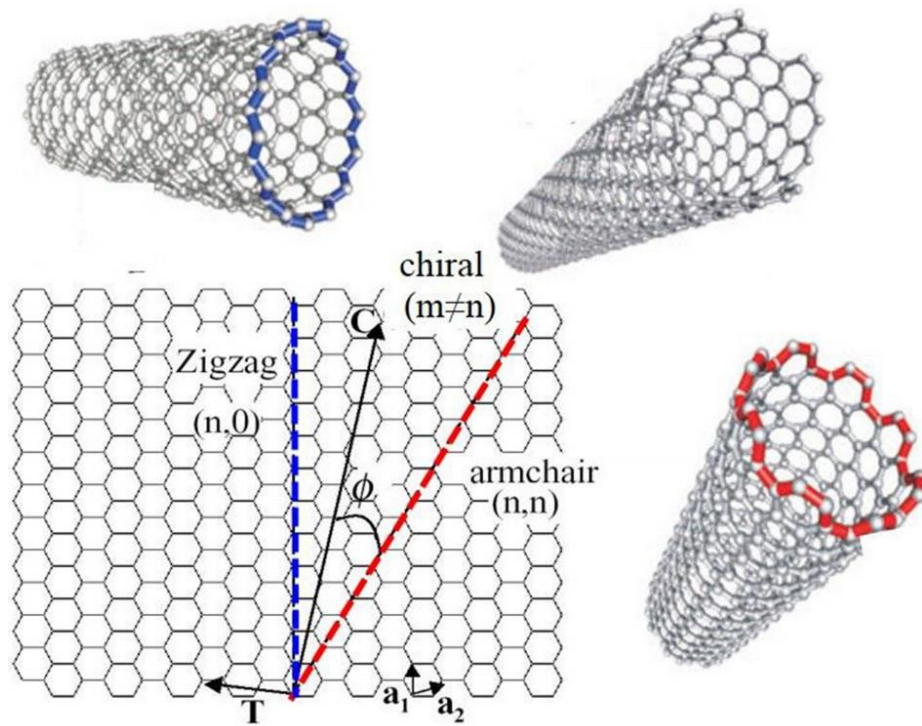


Figure 1.3.1 Graphene rolled up to form different types of SWCNT, armchair, zigzag, and chiral [10].

1.4 Transition Metal Dichalcogenides (TMDCs)

TMDCs family is a large class of 2D layered materials consisting of MX_2 , where M is the transition metal atoms (e.g Mo and W) and X is the chalcogen atoms such as S, Se and Te [16]. Unlike graphene, TMDC layer is a three-atom-thick, where an atomic plane of transition metals is sandwiched between two atomic planes of chalcogen atoms (X-M-X) as shown in Figure 1.4.1a. Due to the quantum confinement and significantly reduced dielectric screening, the Coulomb interactions, between charge carriers in TMDC monolayer, are strongly enhanced in comparison to bulk TMDC, as shown in Figure 1.4.1b. Typical examples of TMDCs are MoS_2 and WS_2 which are semiconducting materials that demonstrate a transition from an indirect gap in their bulk form to direct gap in monolayer form. The band gap of MoS_2 and WS_2 , when they are thinned down to one single sheet, are about 1.9 eV and 2.1eV, respectively [17]. The exciton binding energies in those 2D monolayers are more than an order of magnitude compared to their bulk. This results in strong optical absorption by monolayer TMDC. The indirect transition in bulk TMDCs is a result of the transition between the valence band (VB) maximum at the Γ point to the conduction band (CB) minimum halfway between the Γ and K points Figure 1.4.1c. Despite the atomic thickness of TMDC layer, it exhibits strong light-matter interactions where a single layer of TMDC can absorb up to 10% of incident light [18]. Therefore, TMDCs are excellent candidates for optoelectronic applications such as photodetectors, light emitting devices (LEDs) and photovoltaics [19].

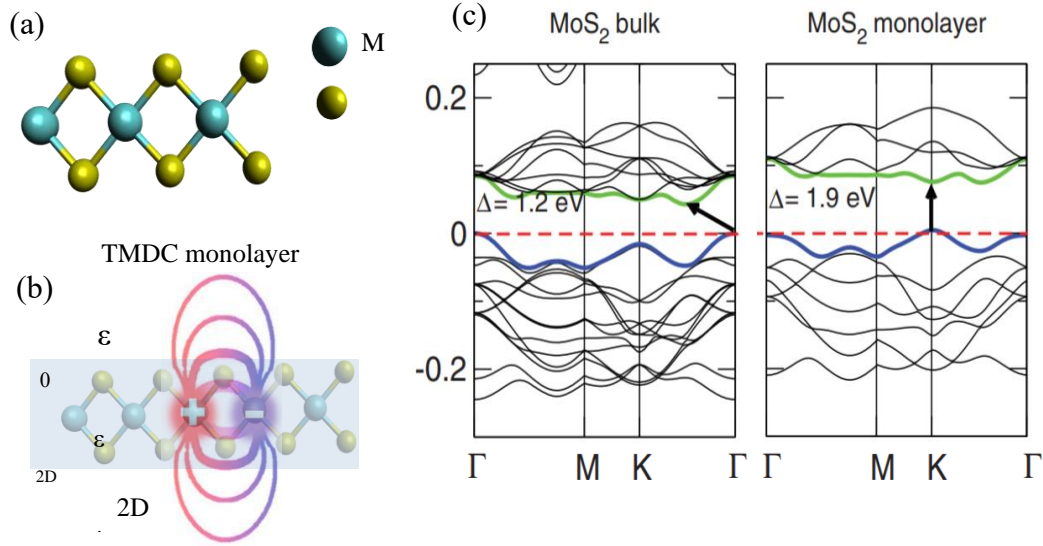


Figure 1.4.1 (a) Crystal structure of a single-layer TMDC. (b) Real-space representation of an exciton in 2D TMDC monolayer, ϵ_{2D} dielectric constants and the ϵ_0 vacuum permittivity. (c) Band structures of bulk and monolayer of MoS_2 [16].

1.5 Van der Waals (vdW) heterostructures of low-dimensional materials

It is possible to stack different low-dimensional materials on top of each other to form vertical heterostructures that are held by vdW forces (Figure 1.5.1a) [20, 21]. Unlike conventional heterostructures, vdW heterostructures of low-dimensional materials can produce high-quality interface without lattice match constraints and no dangling bonds. The thickness of produced heterostructures is in atomic-scale with large interface area between the two layers. Interlayer exciton (e and h separated to different layers) in this vdW heterostructure still experience strong Coulomb interaction due to the small interlayer separation between two stacked layers. For example, the vdW heterostructures of semiconducting MX_2 layers are possibly stacked to form type-II heterojunctions which result in the formation of the interlayer exciton [22, 23]. In this type of heterostructure, the lowest-energy electron states and the lowest-energy holes states are spatially separated in two different monolayers [24] (Figure 1.5.1b). The lifetime of excitons in such

heterostructure is found to be longer (up to an order of magnitude) than intralayer excitons confined in individual 2D layer [25]. The graphene/*h*BN heterostructures were originally constructed in 2010 where *h*BN can serve as an excellent substrate for graphene [26]. A high ON/OFF current ratio is an important parameter in the logic applications, however, the lack of bandgap in graphene leads to a very low ON/OFF current ratio. The TMDCs, such as MoS₂ and WS₂, with large and direct band gaps, and graphene can be vertically stacked for higher on/off current ratio. A vertically stacked TMDC/TMDC heterostructure forms a heterojunction with type-II band alignment [27-29]. Optically excited electrons and holes are spatially separated into opposite layers to form a tightly bound interlayer exciton (the electron and hole are located in different layers). In The oscillator strength of this interlayer exciton is two orders of magnitude lower than intralayer [27]. Graphene/TMDC vdW heterostructure are widely used where the TMDC layer is utilized for superior light-absorption and graphene for ultrafast charge mobility for various applications. The atomically sharp and clean interface between graphene and TMDC facilitates the photo-excited carrier (in the TMDC) to transfer across their interface. In addition, graphene and CNTs have superior properties such as large surface-to-volume ratios, electrical and thermal transport. Therefore, it is beneficial to combine them to form graphene/CNTs vdW heterostructures that can compensate for their shortcomings. All these unique properties of low-dimensional materials vdW heterostructures open the possibility to design various novel devices for different applications. We utilized graphene/TMDC vdW heterostructure to enhance the performance of SERS and photodetectors as we will discuss in chapters 3-5. In chapter 6, we discuss the application of graphene/CNTs vdW heterostructures in H₂ gas sensor.

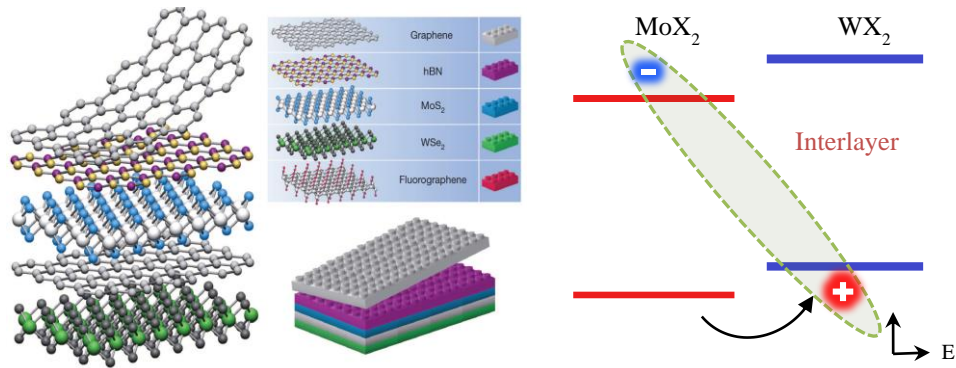


Figure 1.5.1 (a) Concept of building 2D heterostructures as analogous to Lego Block [20]. (b) Schematic of band alignment of type-II of typical MoX₂/WX₂ heterostructure.

1.6 Plasmonic nanostructures

Surface plasmons (SPs) are coherent oscillations of conduction electrons on a metal surface excited by electromagnetic radiation at a metal-dielectric interface [30]. Plasmonic is a field that studies the surface plasmons (light-metal interactions). There are two types of SPs: (1) propagating surface plasmon polaritons (SPPs) and, (2) Localized (non-propagating) Surface Plasmons (LSP). In SPPs, plasmons propagate along the planar of metal-dielectric interface, for distances on the order of tens to hundreds of microns, and decay exponentially in the perpendicular direction as shown in Figure 1.6.1a. The LSP is non-propagating excitations of the conduction electrons of metallic nanostructures coupled to the electromagnetic field (EM), Figure 1.6.1b. Metallic nanoparticles with sizes smaller than the wavelength of incident electromagnetic field exhibit strong dipolar excitations as a localized surface plasmon resonances (LSPR). The conduction electrons in noble metal nanoparticles can be displaced from their nuclei. The opposite charges build up on the surface of the particle and act as a restoring force for the oscillating electrons. The resonance

condition is only met when the frequency of the incident EM matches the frequency of the oscillating electrons on the surface of the nanoparticle as in Equation 8.

$$\omega_{LSPR} = \sqrt{\frac{\omega_p^2}{1 + 2\varepsilon_m} - \gamma^2} \quad (8)$$

where ε_m is the dielectric constant of the surrounding medium, γ is related to carrier damping due to scattering of the free carriers, and ω_p is plasma frequency.

$$\omega_p = \sqrt{\frac{ne^2}{\varepsilon_0 m^*}} \quad (9)$$

where e is electric charge, ε_0 is the permittivity of free space, n the carrier density, and effective mass m^* of the carriers.

Therefore, changes in the carrier density will lead to changes of ω_p and consequently will cause changes in the ω_{LSPR} of the collective plasma oscillation. Noble metals such as Ag and Au have carrier densities in the range of 10^{23} cm^{-3} and show LSPRs in the UV-visible range of the electromagnetic spectrum [31]. LSPRs are not limited to noble metals, but possibly occur in semiconductor nanostructures as well. The LSPRs of semiconductor nanostructures show similar size and shape tunability of LSPRs as metals. In addition, the LSPR can be tuned in semiconductors by varying charge carrier concentrations through changing dopant concentration.

Assuming that the size of the metal nanoparticle is smaller than the incident wavelength (Mie's theory), the phase will be constant over the volume of the nanoparticle (the phase change over the volume of the nanoparticle is negligible), that will induce a polarization (induced dipole) with dipole moment \vec{P} :

$$\vec{P} = \varepsilon_m \alpha \vec{E} \quad (10)$$

Here α is

$$\alpha = 4\pi \epsilon_0 a^3 \frac{\epsilon - \epsilon_m}{\epsilon + 2\epsilon_m} \quad (11)$$

where α is the static polarizability of the sphere, ϵ is the sphere dielectric constant of metal, \vec{E} is the electric field of the light, and a is the diameter of the NP.

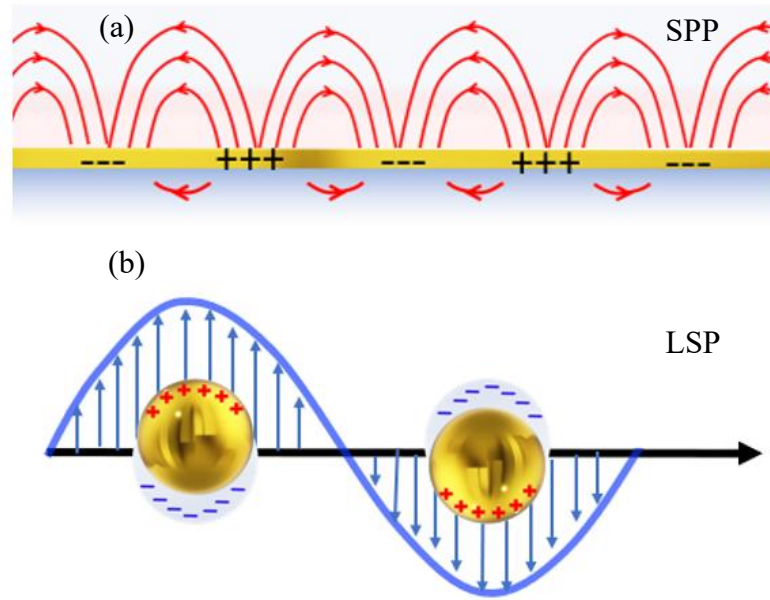


Figure 1.6.1 (a) Schematics of the EM field of surface plasmons propagating along at a metal and dielectric interface. (b) Schematic of a localized surface plasmon of a metal nanoparticle illustrating the displacement of the electron charge cloud relative to the nuclei.

In chapters 3-5, we will exploit the LSPR, in metal and semiconductor nanostructures, to enhance light-matter interaction for enhanced optoelectronic devices based on 2D vdW heterostructures.

1.7 Remaining Critical Issues and Motivation of his Thesis

Despite the remarkable progress that has been made on low dimensional applications, several challenges remain to be addressed. First, the large-scale synthesis of 2D materials is a great challenge for practical applications. Numerous methods, including liquid and mechanical exfoliation, have been explored for 2D materials synthesis and they are only suitable for fundamental research. These methods can only produce small flakes which significantly hinder the 2D materials commercialization. The chemical vapor deposition (CVD) method has a great potential for large-scale production of 2D materials at low cost. In this thesis, the CVD method was used for the synthesis of centimeter-scale graphene and TMDCs.

In SERS applications, it is a challenge to design SERS substrate that are able to detect analytes with higher sensitivity and selectivity. Plasmonic metal nanostructures on SERS substrate generate significant EM enhancement of the local electromagnetic field that can enhance Raman signal of probe molecules. However, a new design of the 2D vdW heterostructure should be developed for higher sensitivity through enhanced CM effect which could be added on top of the EM effect. Plasmonic metal nanostructures enhance the incident electromagnetic (EM) fields near their surfaces due to the collective oscillations of high-density conduction electrons. By integrating the 2D materials or their vdW heterostructures with plasmonic metal nanostructures, the high-intensity EM fields around plasmonic metal nanostructures dramatically improve the light-matter interaction in 2D materials. Consequently, the synergic effect of EM and CM enhancement might be achieved. Fabricating the 2D vdW heterostructures need to be optimized to eliminate the contaminations at the interface that may be introduced during the transfer process for enhanced SERS and photodetection.

Thirdly, photodetectors based on 2D vdW heterostructures with graphene can have broadband absorption and high photoresponsivity by combining the strong light-solid interaction of the TMDC and the high carrier mobility of graphene. However, slow photoresponse speed has been an issue due to contaminated graphene/TMDC interface as charge traps during the exciton dissociation and charge transfer at the interface. Understanding the correlation of the vdW interface quality and the photodetector performance is therefore important for the development of 2D vdW heterostructure photodetectors with both high sensitivity and fast response speed. In addition, light absorption in TMDC/graphene vdW heterostructures is still limited because of the small thickness of the TMDC as the photosensitizer. In fact, the limited light absorption issue represents a fundamental challenge in optoelectronic devices that only use a thin layer of sensitizer, such as quantum dots of typical diameter of a few nanometers and 2D materials of thickness in the similar range or smaller. Therefore, development of new approaches for light trapping is critical to enhance the performance of these devices.

Finally, H₂ sensing is an important research topic in gas sensing due to the safety concerns in H₂ gas storage and utilization. H₂ concentrations higher than 4% is flammable and explosive. Therefore, developing sensitive H₂ sensors is essential for H₂ applications. For H₂ gas sensing, a strong interaction between the CNTs and H₂ gas is necessary for high-efficiency H₂ detection. Air molecules can be adsorbed on the carbon surface when the carbon nanostructure gas sensors are in ambient. For example, the O₂ adsorption not only induces electronic structure change via hole doping, but also affects H₂ interaction with the carbon surface, resulting in degraded H₂ sensitivity and response speed. Therefore, effective and non-destructive technique is required for desorbing the air molecules on the carbon nanostructure surface for further enhancement of the H₂ sensor performance in terms of both sensitivity and response time.

2 Chapter 2: Experiment

This chapter reviews the relevant experimental methods that have been used in our work for materials synthesis and devices fabrication using a variety of approaches including the chemical vapor deposition (CVD) and vacuum filtration. The characterization techniques, including optical microscopy, Raman spectroscopy, scanning electron microscope (SEM), Atomic force microscopy (AFM), were utilized to characterize our samples.

2.1 Materials Synthesis and Characterization

2.1.1 Graphene

We synthesized graphene using the CVD system. For our work, we were able to synthesize CVD graphene using Cu as a metal catalyst and synthesize graphene without metal catalyst that directly grown on SiO₂/Si substrate (Transfer-Free).

2.1.1.1 Transfer-Free CVD Graphene Synthesis:

The synthesis of graphene was carried out into a quartz tube reactor (25 mm in diameter) inside of a horizontal CVD furnace [32]. A clean SiO₂/Si substrate was inserted into the center of the quartz tubular reactor. Then, H₂ (120 sccm) was introduced in the reactor while increasing the temperature until the desired temperature (1065 °C) was reached. Thereafter, CH₄ (30 sccm) was fed into the reactor to start graphene growth directly on the SiO₂/Si substrate. The growth time was maintained for 3 hours. Finally, after graphene growth, the furnace was naturally cooled to room temperature under the protection of H₂.

2.1.1.2 CVD Graphene Synthesis on Cu Foil and Transfer Graphene to Different Substrates:

The synthesis of graphene also was carried out in a quartz tube reactor (25 mm in diameter) inside of a CVD system, Figure 2.1.1a. A 25 μm thick polycrystalline Cu foil (Alfa Aesar) strip was inserted into the center of the quartz tubular reactor. H_2 (40 sccm) was introduced into the CVD system while increasing the sample temperature to the desired temperature of 1050 $^\circ\text{C}$. The Cu foil was annealed for 1 hour at 1050 $^\circ\text{C}$ to remove atmospheric absorbed molecules and to increase the grain size of the Cu. After 1 hour of annealing at 1050 $^\circ\text{C}$, H_2 was reduced to 7 sccm and CH_4 (40 sccm) was introduced to initiate the graphene growth for 30 minutes. After the graphene growth was completed, the furnace was turned off and the sample was naturally cooled to room temperature under the protection of H_2 Figure 2.1.1b.

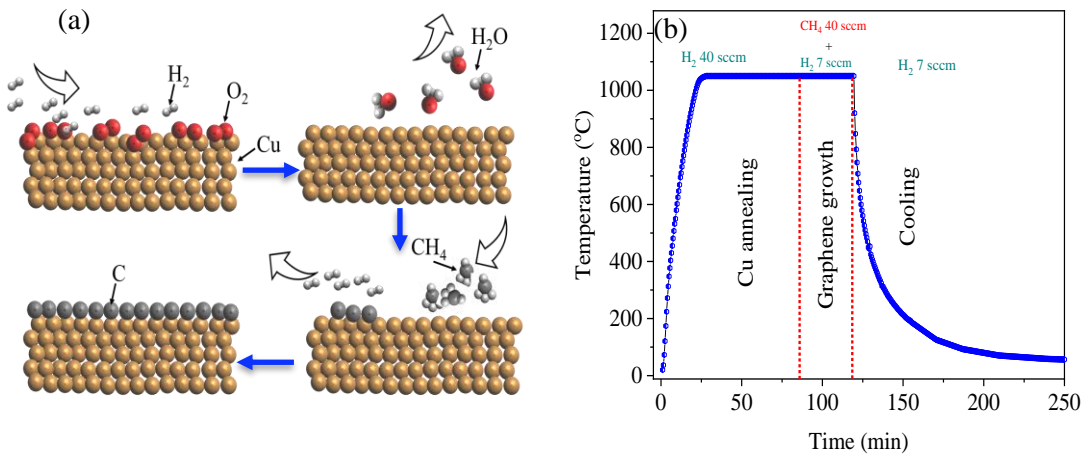


Figure 2.1.1 (a) Graphene growth on the Cu using the CVD method. (b) Temperature and gas flow rate profiles used for the graphene growth as a function of the processing time.

Graphene on Cu foil has to be transferred to insulating substrate such SiO_2/Si . In transfer process, poly(methyl methacrylate) (PMMA) spin-coated (3000 rpm) on graphene/Cu and then baked at 120 $^\circ\text{C}$ for 5 min to enhance the adhesion between graphene and the PMMA. Afterword, the Cu

foil was etched in FeCl_3 solution in about 40 minutes. The suspended graphene/PMMA layer was then washed with deionized (DI) water several times. The graphene/PMMA then was transferred onto the SiO_2/Si . The PMMA layer is removed using acetone and rinsed with isopropanol (IPA), then dried with N_2 gas. Finally, the graphene is annealed at $450\text{ }^\circ\text{C}$ in Ar/H_2 gas (500 sccm/300 sccm) environment for 1 hour to clean the PMMA residues from graphene, Figure 2.1.2.

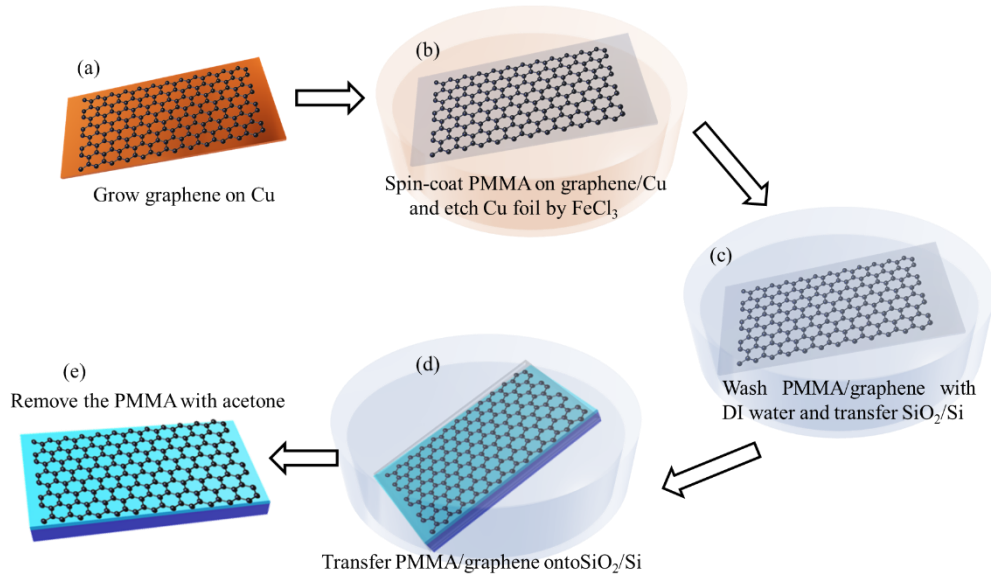


Figure 2.1.2 Schematic illustration of the wet transfer process of graphene from Cu to SiO_2/Si .

2.1.2 Transition Metal Dichalcogenides (TMDCs)

The CVD TMDCs were synthesized using the thermal decomposition technique, Figure 2.1.3. In this technique, ammonium tetrathiomolybdate ($(\text{NH}_4)_2\text{MoS}_4$) or ammonium tetrathiotungstate ($(\text{NH}_4)_2\text{WS}_4$) were thermally decomposed to produce MoS_2 and WS_2 , respectively. A 10 mg of the $(\text{NH}_4)_2\text{MoS}_4$ or $(\text{NH}_4)_2\text{WS}_4$ powder were dissolved in 10 mL of N,N-dimethylformamide (DMF) to make precursor solution with a concentration of 0.1 wt%. After sonication of the precursor

solution for 20 min. SiO₂/Si substrate was immersed into the precursor solution of (NH₄)₂MoS₄ or (NH₄)₂WS₄, followed by spin coating at 3000 rpm for 1 min [33]. Afterward, the substrate was placed in a quartz tube CVD furnace and heated to 450 °C under a 40 sccm flow of Ar and a 10 sccm of H₂ in the presence of the sulfur vapor. The pressure in the CVD system was maintained at 50 mTorr for 1 hour for MoS₂ or WS₂ growth. For TMDCs-Nanodisks (NDs), one dip coating followed by immediate spin coating at 3000 rpm, will result in a very thin layer of the precursor that segregated into NDs with small diameter (~ 200-400 nm). Increasing the number of dipping times (~1-5 times) into the precursor lead to different morphology for the WS₂ from NDs, large islands, to continuous layers.

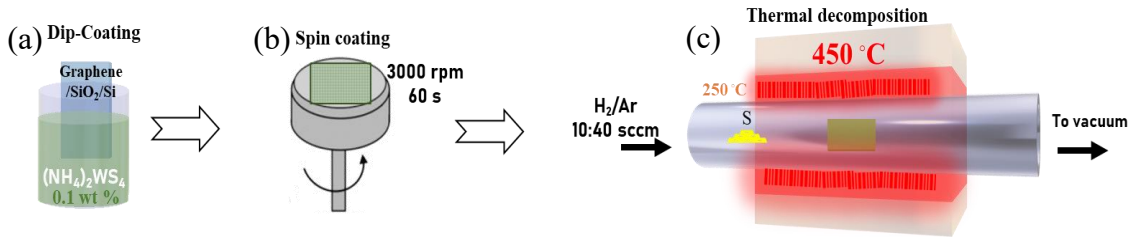


Figure 2.1.3 Schematic of TMDCs growth using the CVD.

2.1.3 Carbon Nanotube (CNTs)

CNT films were synthesized using a vacuum filtration method [34, 35] from CNT suspension as shown in Figure 2.1.4. To prepare the CNT suspension, a commercial purified CNT (90 wt.%) powder synthesized using the CVD process (CheapTubes, Inc) was dispersed in DI water with assistance of Triton X-100 surfactant as a dispersing agent. The suspension was sonicated for 40 minutes using an ultrasonic probe (Cole-Parmer) at 750 W power at 30% amplitude for 1 hour to obtain well-dispersed CNTs in the suspension. For fabrication of the CNT films, a home-built vacuum filtration system was used. For the CNT films used in this work, a 25 mL CNT suspension was pulled through a mixed cellulose ester (MCE) filter membrane (Millipore, diameter 47 mm) with the aid of a vacuum pump. Since the CNT film thickness can be controlled by the amount suspension used in the filtration process, 25 mL was selected to obtain a CNT film of ~500 nm thickness. After the filtration, the CNT film on the membrane was cleaned multiple times with DI water to remove residues of chemical agents especially the Triton X-100 surfactant from the CNT film.

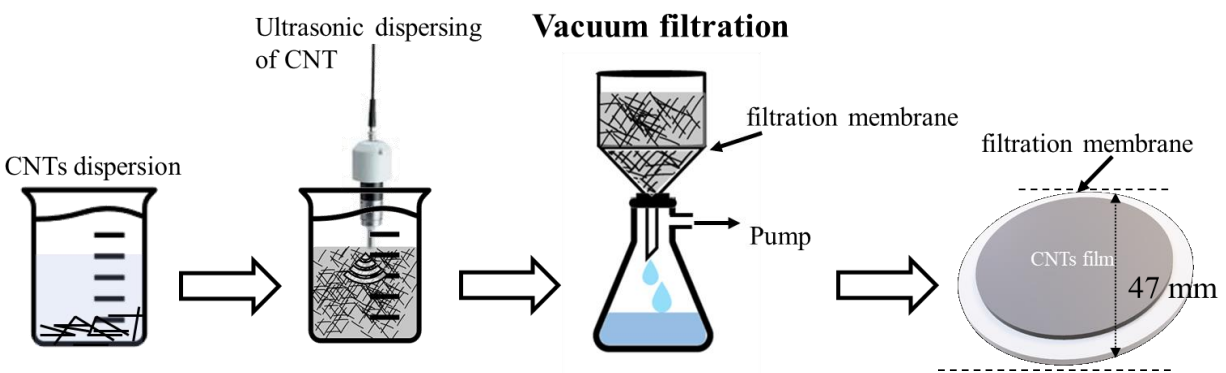


Figure 2.1.4 Schematic of the CNT thin film preparation process using the filtration method.

2.2 Devices Fabrication and Characterization:

2.2.1 The SERS MoS₂/graphene 2D vdW Heterostructure Substrate

The MoS₂/graphene 2D vdW heterostructure samples were fabricated in a layer-by-layer, transfer-free process on commercial SiO₂/Si substrates. First, the transfer-free graphene was synthesized directly on SiO₂/Si substrates as described in section 2.1.1.1. For synthesis of MoS₂ layers on the graphene/SiO₂/Si substrate, the thermal decomposition method (described in section 2.1.2) was used. It should be noted that the direct growth of graphene on SiO₂/Si substrates can eliminate the cumbersome graphene transfer process and it produces graphene with no contaminations that may have left after using PMMA and other chemicals during the graphene transfer process. The annealing of (NH₄)₂MoS₄ layer under low temperatures in the range 450-500 °C further clean the interface of MoS₂/graphene. The interface of the transfer-free MoS₂/graphene heterostructure is cleaner than that of the similar heterostructure on transferred graphene, which is important to attachment of the probe molecules for Raman spectroscopy. In order to decorate AuNPs on the MoS₂/graphene heterostructures, electron-beam evaporation was employed to coat 12 nm thick (nominal thickness) Au in high vacuum of 10⁻⁶ Torr at 300 °C. AuNPs therefore formed in situ on MoS₂/graphene heterostructures. This method provides additional advantages of a clean interface with the underneath layer [36-38]. Scanning electron microscopy (SEM, LEO 1550) was used for morphological characterization of the AuNPs. A R6G solution of the concentration 5x10⁻⁵ M was prepared by adding solid phase R6G (Sigma Life Science) to deionized (DI) water. The concentration of 5x10⁻⁵ M was further diluted for lower concentrations by mixing with DI water to obtain the desired concentration of the R6G. For Raman study, a single droplet (~10 μL) of selected concentrations of R6G solution was casted on the SERS substrate, followed with baking on a hotplate at 70 °C for 1 hour before Raman characterization. Raman spectra were collected

using a Witec Alpha300 Confocal microRaman Microscope. The non-resonant excitation (633nm) and resonant excitation (532 nm) lasers were both used in Raman measurements. A Horiba iHR550 spectrometer was used for optical transmittance measurements. The integration time for each collected Raman spectrum was 3s and typically 4-5 spectra were taken to reduce the noise and enhance the S/N ratio.

Figure 2.2.1a displays an optical image of a representative MoS₂/graphene vdW heterostructure, which is uniform in a large area. The top part of the sample (above the dashed line) was purposely not coated with MoS₂ for convenience of the characterization. Figure 2.2.1b shows Raman spectra of graphene (above the dashed line in Figure 2.2.1a) and MoS₂/graphene vdW heterostructure (below the dashed line in Figure 2.2.1a). In both spectra, the Raman characteristic peaks at ~1586 cm⁻¹ and 2722 cm⁻¹ correspond to the G and 2D bands of graphene, respectively [39-41]. The G peak corresponds to the E_{2g} phonon at the Brillouin zone center and the 2D peak is the second order harmonic of the D peak that corresponds to A_{1g} breathing mode [39]. High-quality single-layer graphene is confirmed by the high ratio of the 2D and G band intensities (I_{2D}/I_G ~ 1.7) and the negligible intensity of D the peak associated to the defects in pristine graphene and graphene after MoS₂ growth. The two characteristic peaks of MoS₂ are clearly visible in Figure 2.2.1b at 384 cm⁻¹ and 406 cm⁻¹ corresponding to the in-plane E_{2g} mode and out of plane A_{1g} mode. The frequency difference between the two modes is ~ 23 cm⁻¹ indicates that the synthesized MoS₂ on graphene is an ultrathin layer (~ 2-3 layers) [42, 43]. The morphology and distribution of the AuNPs on MoS₂/graphene heterostructure were characterized using SEM as shown in Figure 2.2.1c. The AuNPs size range is 40-100 nm in diameter.

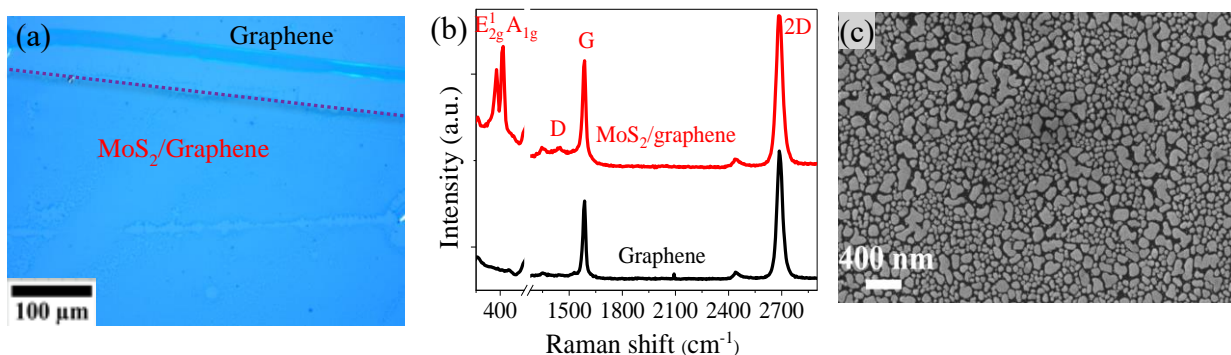


Figure 2.2.1 (a) Optical image and (b) Raman spectra of the MoS₂/ graphene and, (c) SEM of AuNPs on the MoS₂/graphene substrate.

2.2.2 The WS₂-NDs/graphene photodetector

For the WS₂-NDs/graphene photodetector fabrication, the metal electrodes (source and drain) of Au (40 nm)/Ti (10 nm) were deposited on transfer-free graphene using electron-beam evaporation through a metal shadow mask. The distance between the electrodes (graphene channel length) is about 250 μm. Then, the substrate was dipped into the precursor solution followed with the spin-coating for a uniform layer covering the entire sample including the electrodes. Afterward, the substrate was placed in the CVD furnace for WS₂ growth. Raman spectra and Raman maps of graphene and WS₂ were collected using a Witec Alpha300-Confocal Raman Microscope. Atomic force microscopy (AFM) on the same Witec system was employed to characterize the morphology and dimension of the WS₂-NDs. Current–voltage (I–V) characteristics of the photodetectors were measured using a CHI660D electrochemical workstation. The temporal photoresponse measurements, at 550 nm illumination with different powers and different bias voltage, were performed using an Oriel Apex monochromator illuminator.

Figure 2.2.2a displays an optical image of WS₂-NDs/graphene vdW heterostructure. The sample looks fairly uniform in large area. The two characteristic peaks of WS₂-NDs, at 357.16 cm⁻¹ and 421.9 cm⁻¹, are shown in the Raman spectrum (red) in Figure 2.2.2b. These two peaks correspond to the in-plane E_{2g}¹ mode and out of plane A_g¹ mode of WS₂ [44, 45]. The full width at half maximum (FWHM) of E_{2g}¹ and A_g¹ Raman peaks are about 18.95 cm⁻¹ and 8.55 cm⁻¹, respectively, illustrating good crystallinity with moderate defects. However, these FWHM values of WS₂-NDs are relatively larger than that reported for the crystalline exfoliated WS₂ of 11.17 cm⁻¹ and 4.67 cm⁻¹, [46] which suggests the presence of growth defects in the WS₂-NDs. Consequently, the WS₂-NDs may be doped due to the presence of the defects, which may contribute to the LSPR effect as to be discussed in chapter 4. The Raman spectrum of the WS₂-CL (black) is also included in Figure 2.2.2b. The slight blue-shift of the E_{2g}¹ mode to 360.26 cm⁻¹ could be attributed to the smaller number of layers of the WS₂ (2-3 layers) as opposed to that WS₂-NDs (4-7 layers). The optical absorption spectra of the WS₂-NDs with different size and density were taken in the wavelength range of 400–900 nm. The Raman characteristic G and 2D peaks of graphene at ~ 1609.00 cm⁻¹ and 2689.01 cm⁻¹, respectively, are clearly seen in Figure 2.2.2c: graphene (green), graphene with WS₂-NDs (red) and graphene with WS₂-CL (black). It should be noted that the total amount of the WS₂ material is much more in the WS₂-CL/graphene as compared to the WS₂-NDs/graphene samples because of thicker coating of the precursor in the former. The larger number of the WS₂ layer number may be attributed to the segregation of the very thin WS₂ into WS₂-NDs in the latter case. The G peak corresponds to the E_{2g}¹ phonon at the Brillouin zone center and the 2D peak is the second order of the D peak that corresponds to A_g¹ breathing mode [39, 40]. The low intensity of D peak for the graphene at 1357.12 cm⁻¹ on graphene and graphene with WS₂-NDs indicates the high quality of the transfer-free graphene that remain intact after the growth of WS₂-NDs. As

shown in Figure 2.2.2c, the G and 2D peaks of graphene with the WS₂-NDs (red) are enhanced by 2.2 and 3 times, respectively, as compared to that on graphene without the WS₂-NDs (green).

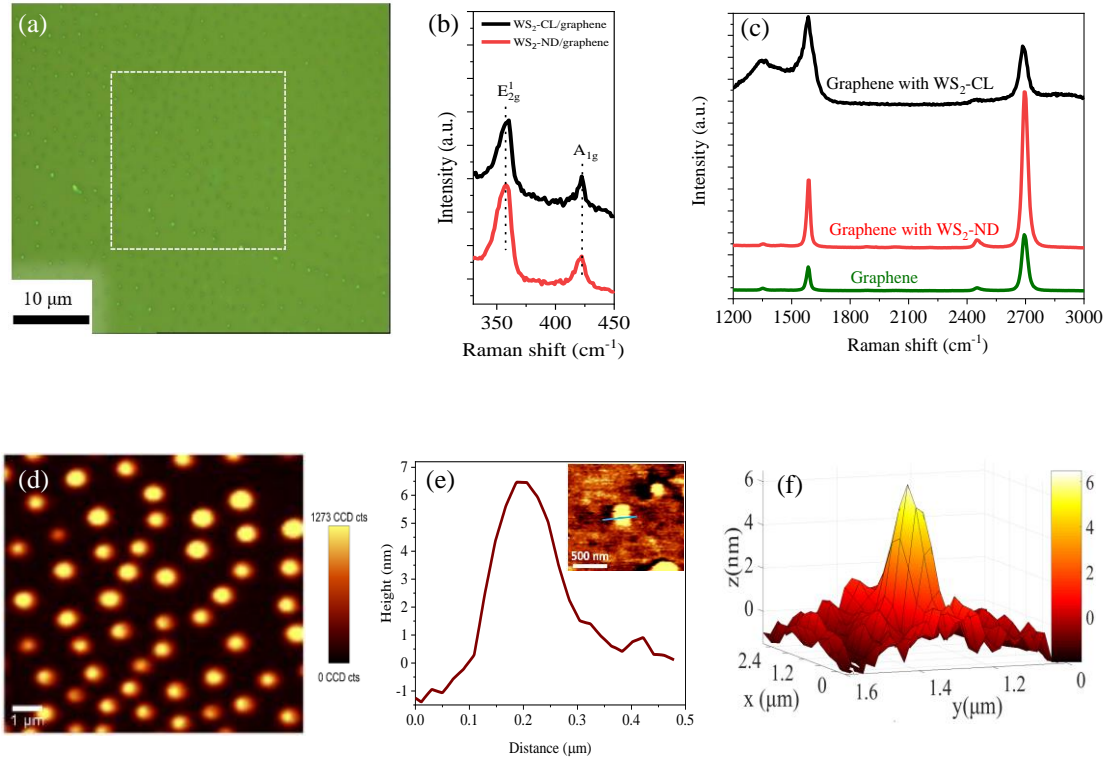


Figure 2.2.2 (a) Optical image of WS₂-NDs/graphene; (b) Raman spectra of WS₂-CL (black), and WS₂-ND (red) on graphene; (c) Raman spectra of graphene with WS₂-NDs (red), with a WS₂-CL (black), and without WS₂ (green). (d) 10x10 μm² Raman mapping images for the E¹_{2g} peak of WS₂-NDs. The dashed square in (a) is the area used for the Raman map of WS₂-NDs; (e) Height profile of WS₂-NDs. Inset: AFM image of WS₂-NDs. (f) A 3D image for a WS₂-ND with thickness of ~ 5 nm and lateral dimension of ~ 200 nm.

2.2.3 The WS₂-NDs/graphene/AgNPs-metafilm photodetector

To fabricate the WS₂-NDs/graphene/AgNPs-metafilm photodetector, first, we fabricated graphene/WS₂-NDs samples that can be transferred onto other surfaces such as the AgNP-

metafilms, a new process was developed in this work that takes two major steps as illustrated in Figure 2.2.3. In the first step, a thoroughly cleaned CVD graphene with the supporting PMMA layer after removal of the Cu foil was placed on top of a WS₂-NDs/SiO₂/Si sample with graphene in contact with the WS₂-NDs. The entire sample assembly was then heated on a hot plate at 80 °C for 1 hour to enhance the adhesion of graphene to the WS₂-NDs. In the second step, the entire sample assembly was soaked in diluted (45-48%) hydrofluoric acid (HF) in DI water for 5 minutes at room temperature to etch the SiO₂ (500 nm in thickness) on the SiO₂/Si substrates. The PMMA/graphene/WS₂-NDs released from the SiO₂/Si substrates was cleaned thoroughly with DI water and was ready for transfer. This sample is different from the WS₂-NDs/graphene photodetector with the WS₂-NDs being directly grown on the graphene/SiO₂/Si without transfer since the latter would have a cleaner interface with minimal residues left in the wet transfer process [47].

Second, the source and drain electrodes of Au/Ti (40 nm/10 nm) for the photodetectors were deposited on other SiO₂/Si substrates using electron-beam evaporation through a metal shadow mask. The separation between the two electrodes (or the channel length) is about 250 μm. The AgNPs-metofilm was in situ fabricated using electron-beam evaporation of Ag of a nominal thickness of 8 nm at an elevated temperature of ~ 300°C under high vacuum (~10⁻⁶ Torr or better) for 30 minutes to obtain AgNPs through in situ self-organization followed with an in situ evaporation of a SiO₂ layer with a thickness of 20 nm to form the AgNPs-metofilm. In order to prevent formation of electrical shorts between the AgNPs and the Au/Ti electrodes, the AgNPs-metofilm was deposited within the channel area with a 200 μm spacing to the Au/Ti source and drain electrodes using a shadow mask.

Finally, the graphene/WS₂-NDs was placed face-down (with the WS₂-NDs towards the AgNPs-metafilm) on the new SiO₂/Si substrates with prefabricated Au electrodes and AgNPs-metafilm. PMMA was then removed using acetone to complete the fabrication of the graphene/WS₂-NDs/AgNPs-metafilm photodetectors.

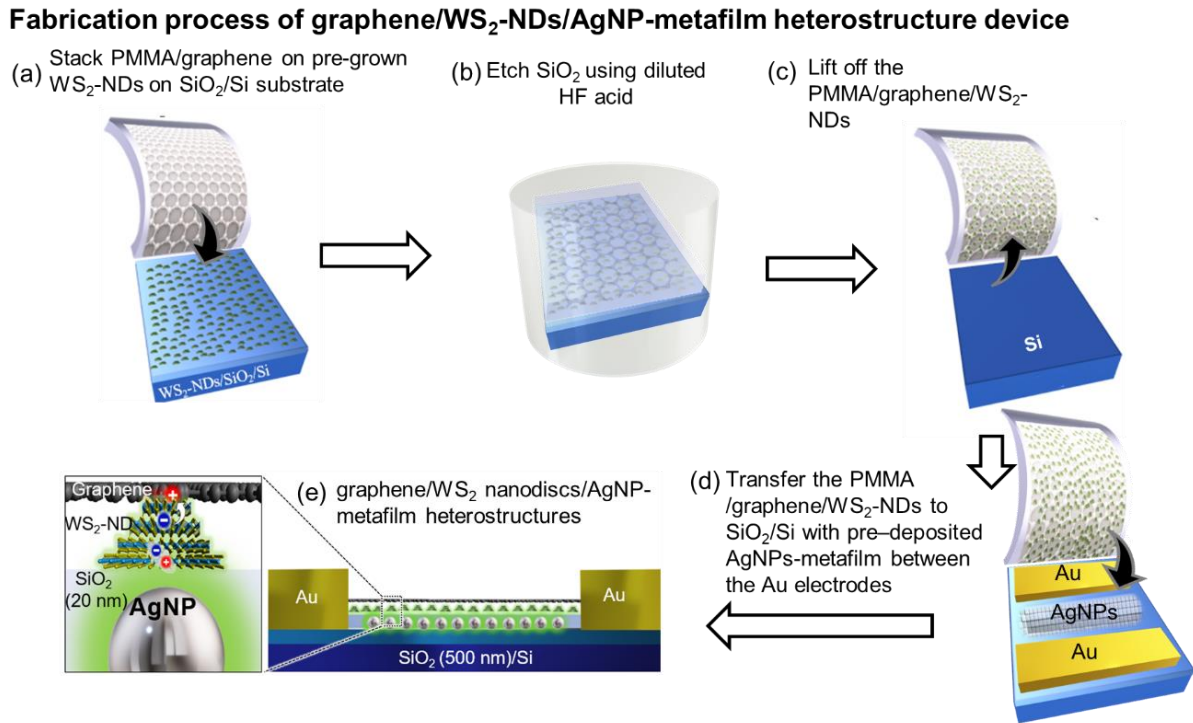


Figure 2.2.3 Schematic illustration of the graphene/WS₂-NDs/AgNP-metafilm heterostructure device fabrication process: (a) stacking PMMA/graphene on pre-grown WS₂-NDs on SiO₂/Si substrate; (b) etching SiO₂ using diluted HF acid; (c) lift off the PMMA/graphene/WS₂-NDs; (d) transferring the PMMA/graphene/WS₂-NDs to SiO₂/Si with pre-deposited AgNPs-metafilm between the Au electrodes; and (e) completing the graphene/WS₂-NDs/AgNP-metafilm heterostructures device after removal of PMMA. Inset shows a zoom-in view of the device cross section with a WS₂-ND on top of 20 nm thick SiO₂ spacer over an AgNP.

This robust method, especially the process for fabrication of the transferrable graphene/WS₂-NDs, is unique and advantageous in terms of preventing degradation of the LSPR effect of the AgNPs due to the exposure to sulfur vapor used for WS₂-NDs growth. In fact, significant degradation of the LSPR effect of the AgNPs (without the SiO₂ over-layer) and AgNPs-metafilms (with the 20

nm thick SiO₂ over-layer) has been confirmed in our experiment (Figure 2.2.4) as we shall discuss in chapter 5. The 20 nm thick SiO₂ layer can effectively and uniformly block the electrical current leakage between the graphene/WS₂-NDs and the AgNPs-metofilm. Based on the FDTD simulation, the evanescent field in the AgNPs-metofilm could extend tens of nm to reach the graphene/WS₂-NDs layer even with the addition of the SiO₂ coating. It should be pointed out that replacing evaporated SiO₂ layer (typically defective) with a less defective dielectric may allow an even smaller distance between the AgNPs-metofilm and graphene/WS₂-NDs photodetector and hence stronger coupling between the plasmons and excitons from the AgNPs and WS₂-NDs, respectively.

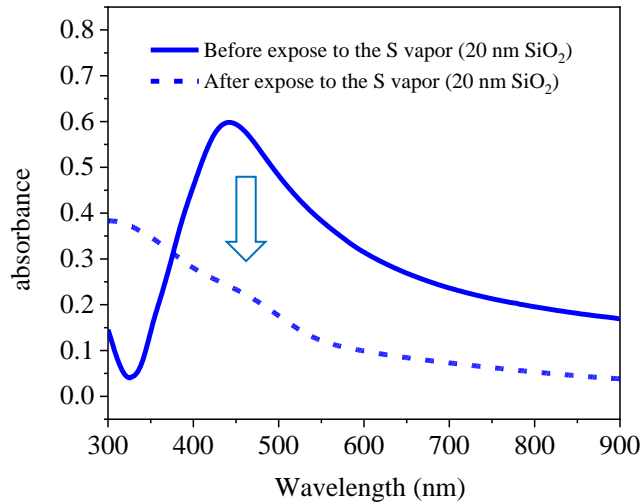


Figure 2.2.4 UV-vis absorption spectra of AgNPs-metofilm before (solid line) and after (dashed line) exposure to the sulfur vapor at 450 °C for 1 hour.

Optical images of the samples were taken using a Nikon Eclipse LV 150 optical microscope with a CCD camera. Raman spectra and Raman maps of graphene and WS₂-NDs were collected using a Witec Alpha300 Confocal Raman Microscope. Atomic Force Microscope (AFM, Witec Alpha300) was used to analyze the vertical and lateral dimensions of the WS₂-NDs. AFM images of the SiO₂ (20 nm)/Ag-NP films were collected in contact mode at a scan rate of approximately 1.0 Hz using a Multimode AFM with a Nanoscope IIIA controller from Digital Instruments. Standard silicon nitride probe tips (Bruker, NP-S, k~0.06 N/m) were used for imaging. All images were collected with the same probe tip. Three different representative regions between the two electrodes were imaged at scan sizes of 10 x 10 μm², 2.0 x 2.0 μm², and 1.0 x 1.0 μm². Average surface roughness (R_a) was measured using the Nanoscope software in the AFM for each of the scans. In addition, images were collected for a sample without the SiO₂ coating over the Ag-NPs. SEM images were taken using a JEOL JSM-6380 scanning electron microscope to characterize the morphology of the AgNPs-metafilm including the shape and size of the AgNPs. The current–voltage (I–V) characteristics of the photodetectors were measured using a CHI660D electrochemical workstation. An Oriel Apex monochromatic illuminator was used to measure the temporal photoresponse at selected wavelengths. To measure the optical absorption spectra, the graphene/WS₂-NDs heterostructures were transferred onto transparent fused silica substrates with and without the pre-fabricated AgNPs-metafilm on the substrates. An ultraviolet/visible spectrophotometer (Perkin Elmer, LAMBDA 35) was used to collect the optical absorption spectra in the visible range for our samples.

Figure 2.2.5 shows an optical image of a representative WS₂-NDs sample fabricated on a SiO₂/Si substrate and the uniform distribution of the WS₂-NDs on the entire sample can be clearly seen. The Raman intensity map of the WS₂ E_{2g}¹ mode is displayed in Figure 2.2.5b, demonstrating the

morphology and lateral dimensions of the WS₂-NDs, with sizes on the order of a few hundred nm. Figure 2.2.5c shows the AFM height profile measured along the green line in the AFM image (shown in the inset). Quantitatively, the lateral dimension of the WS₂-NDs is in the range of 200-300 nm that is consistent with the range revealed in the Raman map in Figure 2.2.5b. The height of the WS₂-NDs is in the range of 4-8 nm. Considering the approximately circular shape, large lateral dimension and small vertical dimension of the WS₂ nanostructures revealed in Figure 2.2.5b,c , WS₂ nanodisks or WS₂-NDs are used to regard the WS₂ nanostructures in this work. The Raman spectra of graphene on SiO₂/Si (black) and on AgNPs-metafilm/SiO₂/Si (green) substrates are illustrated in Figure 2.2.5c. In the former, the two graphene signature peaks at ~ 1614.11 cm⁻¹ and 2719.19 cm⁻¹ are assigned to the G and 2D bands, respectively. The absence of the graphene D peak (associated with defects) confirms the high quality of the CVD graphene in this work. The Raman spectrum of graphene on the AgNPs-metafilm shows an overall enhancement in the intensity that can be attributed to the LSPR effect by the plasmonic nanostructures such as the AgNPs-metafilm in this specific case. Comparing the two spectra shown in Figure 2.2.5d, the G and 2D Raman peaks of graphene with AgNPs are enhanced by 16 and 3 times, respectively. This plasmonic enhancement is consistent with that reported previously [48-51]. It should be noted that the Raman enhancement factors of the graphene peaks depend on the frequencies of the vibrational modes [52]. Therefore, the enhancement factors of the graphene G and 2D peaks are anticipated to be different. In addition, the intense plasmonic EM field of the AgNPs could cause the lattice deformation of graphene and consequently enhance the D peak of graphene at 1387.26 cm⁻¹ [53].

Both G and 2D peak of graphene on AgNPs-metafilm are slightly red-shifted by $\sim 22 \text{ cm}^{-1}$. This red shift may be attributed to tensile strain after graphene is transferred onto the AgNPs-metafilm.

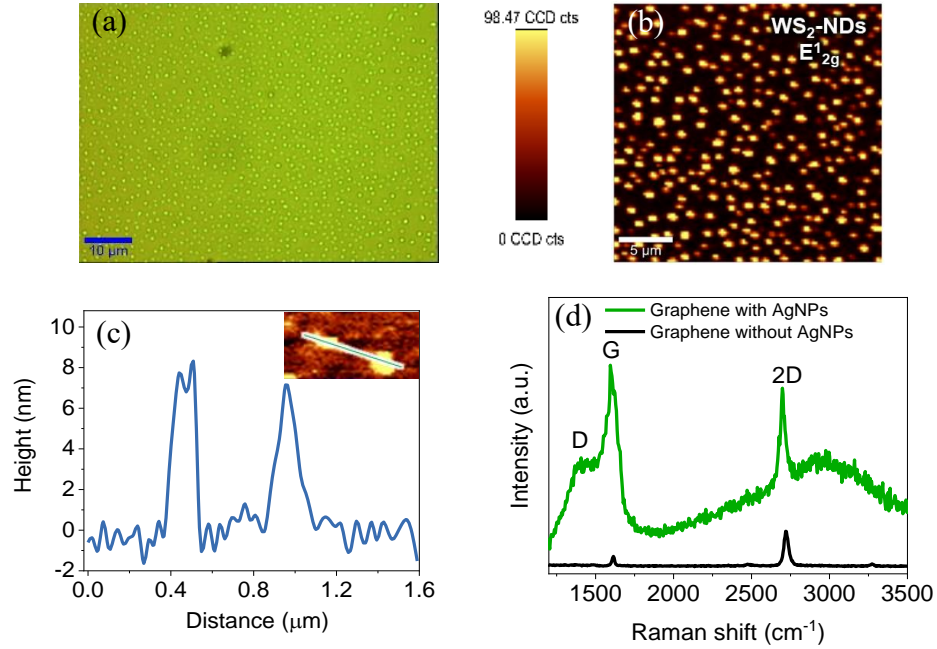


Figure 2.2.5 (a) Optical and (b) Raman image of WS_2 -NDs (c) Height profile of WS_2 -NDs. Inset: AFM image of WS_2 -NDs. (d) Raman spectra of graphene on SiO_2/Si (black) and graphene on SiO_2/Si with AgNPs-metafilm (green)

The absorption spectra for the AgNPs-metafilm (blue), graphene/ WS_2 -NDs (green), and graphene/ WS_2 -NDs/AgNPs-metafilm (purple) are illustrated in Figure 2.2.6a. The maximum absorbance (the LSPR peak) for the AgNPs-metafilm is at the wavelength of 442 nm, which is consistent with that reported previously [38]. The absorption spectrum of the graphene/ WS_2 -NDs shows broadband absorption from 400 nm to 700 nm with a small hump at $\sim 640 \text{ nm}$ (band gap $\sim 1.94 \text{ eV}$ for WS_2). On the absorption spectrum for the graphene/ WS_2 -NDs/AgNPs-metafilm sample, the AgNP's LSPR peak intensity is reduced and slightly red shifted ($\sim 19 \text{ nm}$), which could be ascribed to the damping in graphene as a semimetal as reported previously [32, 38].

Interestingly, an enhanced absorption in a broadband of 400-700 nm can be observed on the graphene/WS₂-NDs/AgNPs-metafilm sample, which can be attributed to the enhanced absorption by the WS₂-NDs with assistance of the LSPR evanescent field enabled by the AgNPs-metafilm. The high AgNPs density may cause a red shift for the plasmonic peak due to an inter-particle coupling. On the other hand, multiple layers of AgNPs may not increase the evanescent EM field at the graphene/WS₂-NDs photodetectors considering the increased distance between the lower AgNPs layers to the graphene/WS₂-NDs photodetectors. An SEM image taken on a representative AgNPs/SiO₂/Si sample is displayed in Figure 2.2.6 b. The AgNPs exhibit irregular shapes. The average lateral dimension of the AgNPs is ranging from 20 nm to 120 nm with mean diameter of 68 ± 27 nm. Representative AFM images of the SiO₂ (20 nm)/AgNPs- metafilm sample at 10 μm^2 and 1.0 μm^2 scan sizes are presented in Figure 2.2.6 c. They show the expected nanoparticles along with a small number of defects. The topographical images of all regions of the sample showed consistently sized nanoparticles. The average roughness for the 10 x 10 μm^2 scans for all three areas was 12 ± 3 nm. A roughness of 11 ± 1 nm was measured for the 1.0 x 1.0 μm^2 scans. The topography and roughness of the sample without the SiO₂ coating was not significantly different than that for the SiO₂ (20 nm)/AgNPs- metafilm sample. The AFM images in Figure 2.2.6c and Figure 2.2.8c were taken by our collaborator Dr. Cindy Berrie group, at the Department of Chemistry, University of Kansas.

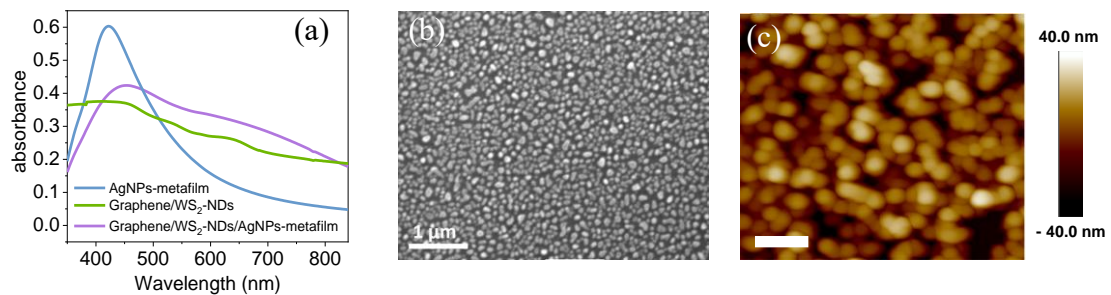


Figure 2.2.6 (a) UV-vis absorption spectra of AgNPs-metafilm (blue) and graphene/WS₂-NDs (green), and graphene/WS₂-NDs/AgNPs-metafilm (purple). (b) SEM image of the AgNPs (c) The 1.0 $\mu\text{m} \times 1.0 \mu\text{m}$ area AFM image of SiO₂(20 nm)/AgNPs.

2.2.4 Atomic layer deposition (ALD) Pt-NPs @ SWCNTs/graphene H₂ Gas Sensor

SWCNT films were synthesized using a vacuum filtration method [35] from SWCNT suspension as described in section 2.2.3. In order to fabricate the ALD Pt-NPs @ SWCNTs/graphene sensor, the SWCNT films of 5 x 10 mm² dimension were cut off from the SWCNT film/filtration membrane and these SWCNT films were ready to be transferred to the functional substrates for device applications. Schematic illustration of the Pt-NPs/SWCNT/graphene H₂ gas sensor fabrication process is shown in Figure 2.2.7.

The Pt-NPs were conformably coated on SWCNT/graphene heterostructures in our home-built in vacuo ALD system [54, 55]. ALD of Pt is ligand-exchange process on the sample surface based on the well-defined chemistry between alternating precursor pulses of MeCpPtMe₃ (pulse duration of 3 seconds) and oxygen (pulse duration of 1 second) at 300 °C. Between different precursor pulses, the ALD chamber was purged with ultrahigh-purity N₂ (99.99%) for 60 seconds. The same N₂ gas was used as the precursor carrier gas (5 sccm). To increase the vapor pressure, the MeCpPtMe₃ precursor was heated to 60 °C during the ALD process. For this work, 20 ALD cycles were used for coating Pt-NPs on the 3D SWCNT/graphene electrodes.

The metal electrodes of Au (40 nm)/Ti (10 nm) were deposited on SiO₂ (500 nm)/Si substrates using electron-beam evaporation through a metal shadow mask. The sensor channel length (distance between the two electrodes) is 250 μm and the channel width is about 4 mm. The PMMA/graphene was then transferred on the SiO₂ (500 nm)/Si substrates with pre-fabricated Au/Ti electrodes, followed with removal of the PMMA using acetone and IPA, then dried with N₂ gas. The PMMA residues were removed by thermal annealing for 1 hour at 450 °C under Ar/H₂ (500 sccm/300 sccm). After graphene transfer, the SWCNT film was transferred onto graphene to form the 2D SWCNTs/graphene heterostructure electrode. The ALD coating of the Pt-NPs was

carried out on the SWCNTs/graphene to complete the ALD Pt-NPs @ SWCNTs/graphene sensor fabrication. Raman spectra and optical images of SWCNTs and graphene were taken using a Witec Alpha300-Confocal Raman Microscope. SEM image was taken using a JEOL JSM-6380 scanning electron microscope to characterize the morphology of the samples. The average thickness of the SWCNT film was measured using a surface profiler (P.16, KLA-Tencor). An UV Ozone Cleaner (ProCleaner™, with two emission wavelengths of 185 nm and 254 nm) was used as the source for the UVC irradiation. For a comparison, an UV source in the UVA spectrum (360-400 nm) was also used in a similar test. The H₂ response of the device was measured using a CHI660D electrochemical workstation. During the measurement, the ALD Pt-NPs @ SWCNTs/graphene sensor was placed inside a vacuum chamber with a constant flow of N₂ gas (180 sccm) with different concentrations of the H₂.

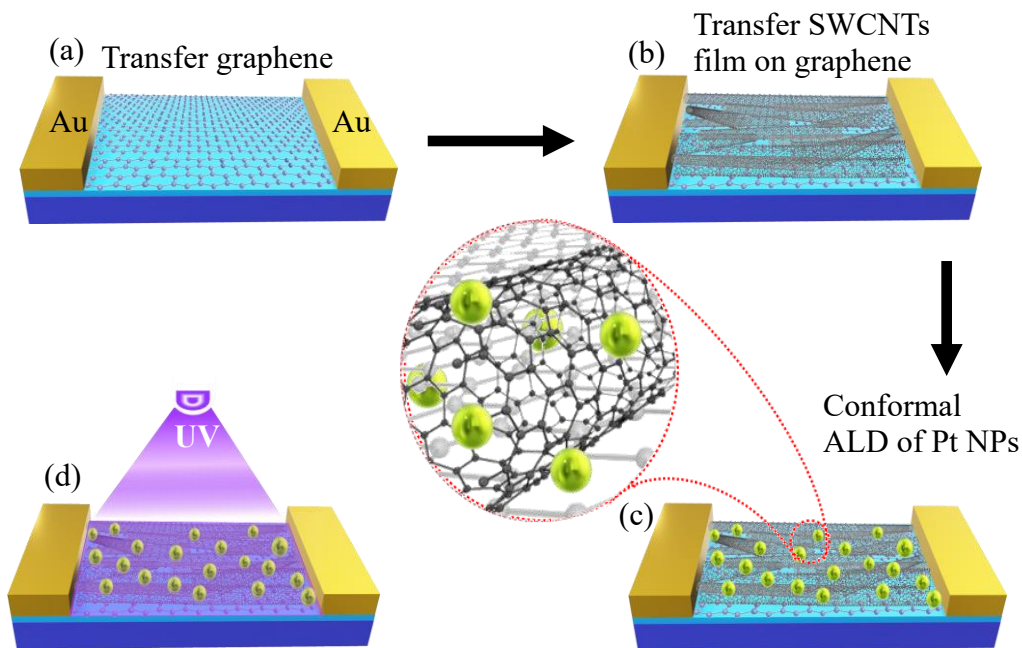


Figure 2.2.7 (a-c) Schematic illustration of the ALD Pt-NPs @ SWCNT/Gr H₂ gas sensor fabrication process. The yellow spheres represent the ALD Pt-NPs formed on the 3D SWCNTs/Gr heterostructure electrode. The inset illustrates the conformal coating of SWCNTs with PtNPs (d) The fabricated device irradiated with UVC.

In Figure 2.2.8 a, displays Raman spectra of graphene (blue) and the SWCNT/graphene (red). The Raman spectrum of graphene showed the typical G peak at $\sim 1604.9 \text{ cm}^{-1}$ and 2D peak at $\sim 2692.5 \text{ cm}^{-1}$. These two peaks are due to the doubly degenerate zone center E_g^2 mode and the second order of zone-boundary phonons, respectively [56]. The absence of the D peak at $\sim 1352.5 \text{ cm}^{-1}$ and the high ratio of 1.8 for the 2D/G peak intensities confirm the high quality of the monolayer CVD graphene. On the SWCNTs, the G peak is separated into two peaks (G^- and G^+ peaks) at 1584.9 cm^{-1} and 1609.0 cm^{-1} due to the curvature of the graphene sheet in the SWCNTs [57, 58]. Another distinctive peak is located at $\sim 2689.01 \text{ cm}^{-1}$ corresponding to the 2D-band for SWCNTs [59], which is slightly shifted with respect to the graphene's 2D peak. The D peak at 1356.6 cm^{-1} associated to the presence of in-plane defects on SWCNTs, possibly the growth defects occurred during CVD synthesis of SWCNTs, is visible with low intensity, suggesting the defects are minor [60]. An additional peak at 192.4 cm^{-1} (the inset of Figure 2.2.8a) can be assigned to the radial breathing mode (RBM) of the SWCNTs [61, 62].

In Figure 2.2.8 b and 2c, show representative SEM and AFM images, respectively, of a Pt-NPs/SWCNTs/graphene H_2 gas sensor. The SEM image shows Pt-NPs (bright particles) scattered uniformly over a film of randomly networked SWCNTs. Bundles of SWCNTs are clearly visible in both the SEM and AFM images, while only relatively large Pt-NPs are visible in the AFM image. Detailed cross-sectional analysis of AFM images, without correction for tip convolution, of these Pt-NPs/SWCNTs/graphene sensors was previously reported by our group [63]. Briefly, the SWCNT bundles form a porous covering over the surface. The diameter and height of these SWCNT bundles were measured to be $43 \pm 13 \text{ nm}$ and $10 \pm 7 \text{ nm}$, respectively. These dimensions are significantly larger than that of the ingredient SWCNTs ($1 - 2 \text{ nm}$). It should be noted that bundling of SWCNTs is not uncommon due to their very large aspect ratio [26]. Energy Dispersive

Spectroscopy (EDS) spectrum is shown in Figure 2.2.8 d. The EDS spectrum confirms the presence of Pt on the SWCNTs/graphene nanohybrid.

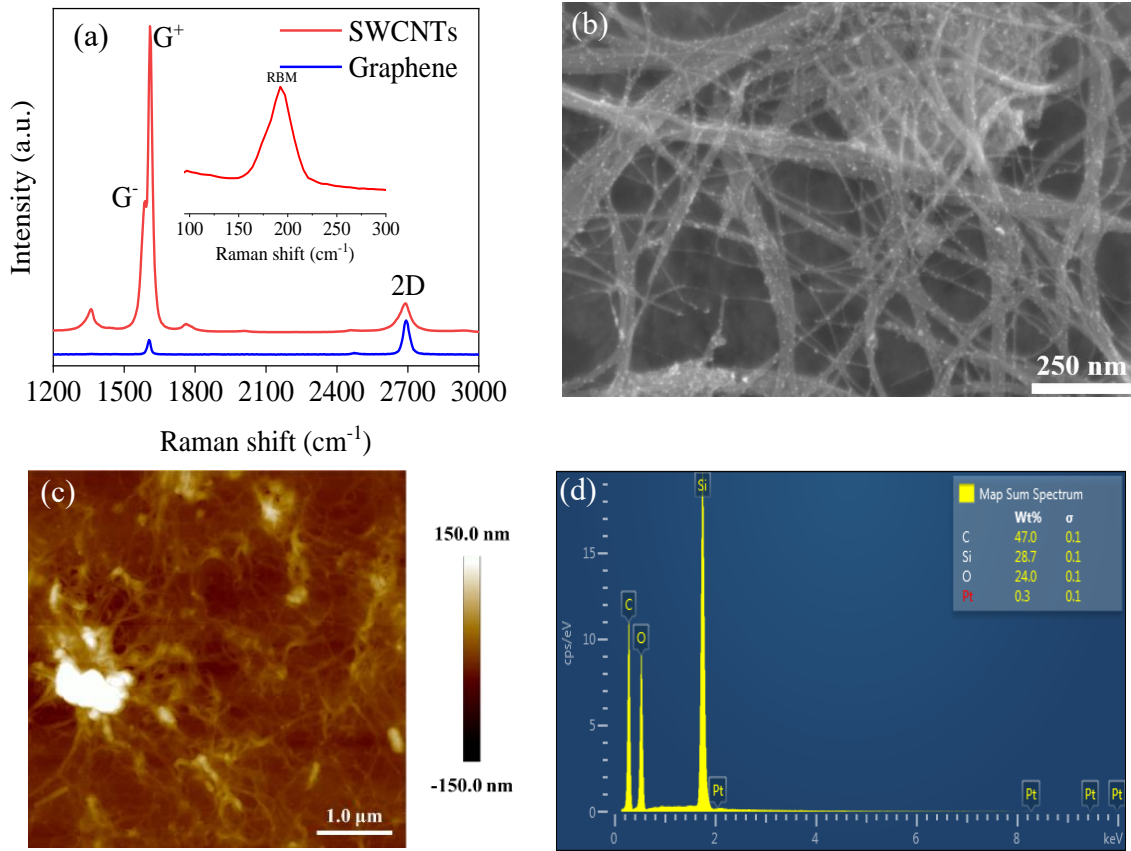


Figure 2.2.8 (a) Raman spectra of the graphene (blue) and SWCNTs (red), respectively. Inset shows RBM peak of the SWCNTs. (b) SEM image of an Pt-NPs/SWCNTs/Gr sensor. (c) 5 μm x 5 μm AFM image of Pt-NPs/SWCNTs/Gr sensor. (d) EDS spectrum of Pt on SWCNTs.

2.3 Simulation

2.3.1 The Density Function Theory (DFT) simulation

The electronic structure of the AuNPs/MoS₂/graphene 2D vdW heterostructure was calculated using the density functional theory (DFT) method. This work was done with the collaboration of Dr. Ridwan Sakidja at Department of Physics, Astronomy and Materials Science, Missouri State University. The AuNPs/MoS₂/graphene 2D vdW heterostructures consist of a combination of a

continuous 2D layer of MoS₂ and multilayers of Au of different thicknesses. This structure was chosen to probe the interface between an AuNP of 10 nm or larger in dimensions positioned on top of a 2D MoS₂ sheet. Considering the lateral dimensions of the Au NP and the 2D MoS₂ sheet are both large, the edge effect will be negligible on the bonding mechanism at the interface, and thus a continuous layer represents a good approximation. The number of Au (111) layers was varied from $n = 1$ (monolayer) up to $n = 6$ to elucidate the effect of the Au thickness on the interface coupling.

2.3.2 Finite difference time-domain (FDTD) simulation

To study plasmonic mode profiles of the AgNPs and their impact on the device performance, the Lumerical Finite Difference Time-Domain (FDTD) solutions software (2020a Finite Different IDE) was deployed to calculate the electromagnetic field distribution around a AgNP in the graphene/WS₂-NDs/AgNPs-metafilm nanohybrid. This work was done in collaboration with Dr. Seyed Sadeghi at Department of Physics and Astronomy, the University of Alabama. Specifically, the Device Mutliphysics Simulation Suite of this software was used by setting up different components to replicate the system of the graphene/WS₂-NDs on the AgNPs-metafilm as closely as possible. The mesh sizes were varied between 1 to 0.5 nm to accommodate different sizes of the AgNPs. The source configuration was set up such that light reached the layer representing the graphene/WS₂-NDs first and then the AgNPs-metafilm.

3 Chapter 3: Plasmonic Au Nanoparticles on MoS₂/graphene for Surface Enhanced Raman Spectroscopy

3.1 Background and mechanism

Raman spectroscopy is a technique based on measuring the frequency shift of inelastic scattered light from the sample. The scattered photon has a lower frequency (Stokes scattering) than the original photon or higher frequency (Anti-Stokes scattering). Only a small fraction of photons scatters inelastically, and most of the scattered photons have the same wavelength as the incident photons (Rayleigh scatter), Figure 3.1.1 a-c. The shift in wavelength depends on the chemical structure of the molecules which can provide quantitative and qualitative information about the individual compounds. The inelastic scattering of photon (Raman effect) was first discovered by C. V. Raman in 1928 and awarded the Nobel prize in Physics in 1930 for this discovery. The extremely low Raman cross sections could limit its sensitivity. Therefore, surface-enhanced Raman spectroscopy (SERS) can overcome this deficiency and is capable of detecting analytes at very low concentration. SERS was first observed by Fleischmann in 1974, who observed that Raman signal intensities of pyridine molecules on rough silver electrode are increased [64]. Thus, SERS is known as a very sensitive tool for molecules detection through enhancing the Raman scattering signal of molecules. This enhancement is commonly attributed to two enhancement mechanisms: (1) the electromagnetic (EM) enhancement and (2) the chemical enhancement (CM). The EM mechanism is a result of the excitation of localized surface plasmon resonances (LSPRs) in metal nanostructures. The intense EM fields around the metal nanostructures increase the intensity of the inelastic Raman scattering. The CM enhancement is due to charge transfer between SERS substrates and probe molecules. The EM dominates the total enhancement where the enhancement factor can reach 10^{10} - 10^{11} whereas the enhancement factor in CM is only about 10-

10^2 [65]. The choice and fabrication of the SERS substrates is crucial for Raman scattering enhancement. Numerous efforts have been dedicated to optimize SERS substrates for high Raman scattering enhancement. Various developed substrates for SERS are discussed in the next section (3.2).

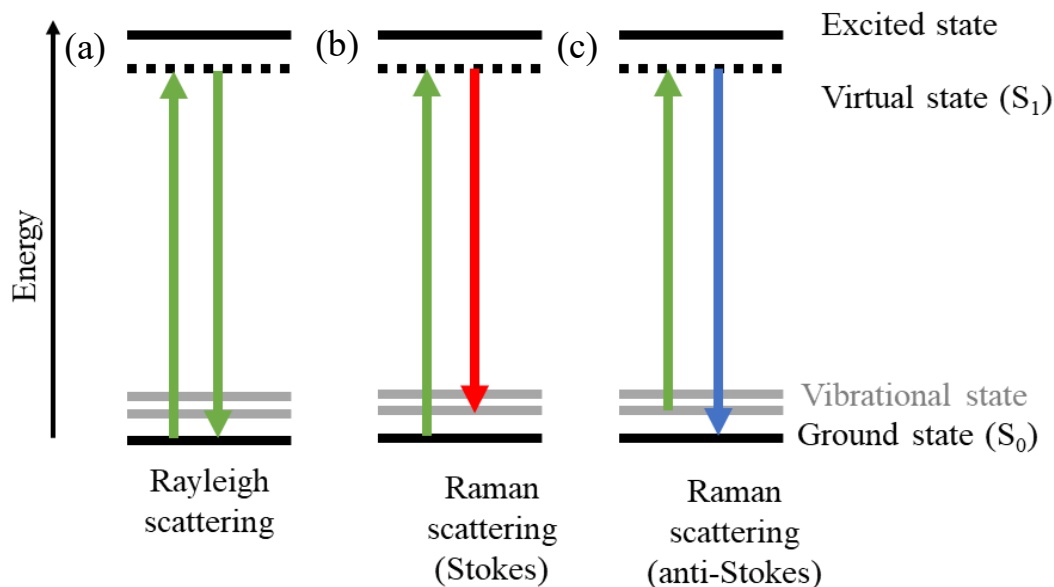


Figure 3.1.1 Jablonski diagrams illustrating (a) the Rayleigh and (b-c) Raman scattering processes.

3.2 Current research on SERS

Several different kinds of SERS substrates based on 2D materials in combination with plasmonic metal nanostructures have been reported recently with enhanced sensitivity for biomolecule detection. Ling et al. investigated graphene SERS enhancement using probe molecules such as Rhodamine 6G (R6G) and crystal violet (CV). The observed SERS enhancement factors of 2–17 depending on the vibrational mode symmetry of the molecules on graphene, as compared to that on the SiO_2/Si substrate, are attributed to the CM effect through enhanced charge transfer between

graphene and molecules. They further revealed the dependence of SERS enhancement on the number of graphene layers as the intensities of the Raman signals of the CV molecules decrease with the increasing layer number of graphene [66]. Similarly, Sun et al. reported the dependence of the Raman enhancement on the layer number of MoS₂ [67]. Specifically, the Raman enhancement of monolayer MoS₂ is comparable to but slightly higher than that on MoS₂ of 2 or 3 layers. This means the SERS sensitivity is not expected to vary dramatically on MoS₂ with the layer number in the range of 1–3. However, the enhancement of 1–3 layers of MoS₂ is much higher than the bulk or multilayer MoS₂. This trend could be attributed to the reduction of the bandgap with increasing thickness of MoS₂ as a consequence of the conduction band decrease while the remaining part of the band structure remains essentially unaltered with increasing thickness. Lee et al. reported the CM enhancement of Raman signatures of R6G dip-coated onto single-layer 2D material including graphene, WSe₂, and MoS₂ substrates that were mechanically exfoliated from bulk crystals. The Raman enhancement effects of these three different substrates were observed and attributed to charge transfer and dipole–dipole interactions [68]. The Raman enhancement factors of R6G on MoS₂ and WSe₂ were about 0.5 and 1.7–2, respectively, relative to the enhancement of R6G on graphene. They fabricated R6G/graphene and R6G/MoS₂ hybrid phototransistors to study their electrical properties and observed that the Raman CM factors were correlated to the amount of the transferred charges between R6G and the 2D materials. Likewise, other 2D materials such as black phosphorus (BP), rhenium disulfide (ReS₂), [69] and tin diselenide (SnSe₂) [70, 71] have been used as SERS substrates. Au and Ag are most commonly used metals as SERS substrates due to their chemical stability and have LSPRs that cover the visible and near infrared wavelength range. Lu et al. developed a hybrid AuNP/graphene SERS substrate that combines the benefits of CM enhancement from graphene with the EM enhancement

of the AuNPs [36]. Using R6G probe molecules, we obtained the SERS sensitivity up to 8×10^{-7} M using a nonresonance 633 nm excitation laser [37]. In fact, a higher SERS sensitivity up to 10^{-11} M can be obtained using a resonance excitation of 532 nm for R6G probe molecules using AuNP arrays covered by a single-layer graphene [72]. More recently, Chen et al. reported a SERS substrate consisting of a few layers of MoS₂ grown on AgNPs of an average dimension of 58 nm using the thermal decomposition method. Using R6G probe molecules, they compared the SERS sensitivity of this hybrid substrate to its counterpart without the MoS₂ layer and concluded that the higher sensitivity of 10^{-9} M using 532 nm laser excitation in the former as compared to 10^{-8} M in the latter may be attributed to the combination of the CM and EM enhancements that arise from MoS₂ and AgNPs, respectively [73].

3.3 Plasmonic Au Nanoparticles on 2D MoS₂/Graphene vdW Heterostructures

We explore AuNPs decorated 2D MoS₂/graphene vdW heterostructures for further enhancement of the SERS sensitivity. 2D vdW heterostructures present a unique platform to design SERS substrates of high CM enhancement through interface interaction of different 2D materials. In a recent theoretical work conducted by Xu et al [73], the bonding mechanisms at the interface between graphene and MoS₂ 2D layer were evaluated, which suggests that the vdW interaction can enable enhanced charge transfer and optical adsorption. Theoretically, we show further enhanced interfacial dipole–dipole interaction through AuNPs decoration on 2D MoS₂/graphene vdW heterostructures using the density functional theory (DFT) simulations. Experimentally, we illustrate a SERS sensitivity up to 5×10^{-8} M for R6G probe molecules using the AuNPs/MoS₂/graphene 2D vdW heterostructure substrate, which is an order of magnitude improvement over that on the AuNPs/graphene [37] and AuNPs/MoS₂ counterparts. The R6G

sensitivity of 5×10^{-10} M was obtained on the AuNPs/MoS₂/graphene 2D vdW heterostructure substrate using resonant excitation of 532 nm, which is one order of magnitude higher than that reported on the AgNPs/MoS₂ substrate [74].

3.3.1 Results and Discussions

It should be mentioned that while there have been theoretical studies to examine the interaction between MoS₂ 2D layer and Au adatom or Au (111) surface, a weak hybridization and charge transfer were concluded [75, 76] at the interface, consequently resulting in a fairly large interlayer distance of 3.405 Å, as theoretically calculated, [75] and low adhesion energy (0.307–0.354 eV per surface sulfur atom). However, little is known so far on the electronic structure of the interface between MoS₂ 2D layer with stacks of free-standing Au (111) multilayers which more aptly represent the hybrid heterostructures of the AuNPs/MoS₂/graphene in this work. Intriguingly, we have found the layer thickness of the Au has a remarkable effect on the interatomic distance of the stack, which in turn affects the charge transfer mechanism of the AuNPs/MoS₂/graphene vdW heterostructures.

Figure 3.3.1 shows the side view of the Au/MoS₂ heterostructures of 1, 3, 5, and 6 monolayers of Au after the relaxation process in DFT simulation. The change in the vertical interatomic distance at the Au/MoS₂ interface can be clearly seen with varying Au layer number. While there is an apparent gradual increase with an increasing number of the Au layer at larger Au layer numbers, there is a surprisingly large initial drop (about 20%) going from an Au monolayer (1L) to two layers (2L). For 1L, we did obtain a slightly smaller interatomic distance than that reported by the previous theoretical work on bulk Au or Au adatom. This may have resulted from the use of vdW force correction in our calculations which tends to shorten the calculated bond length relative to the generalized gradient approach (GGA)-based calculations. Nevertheless, the 3.03 Å distance

arguably points to a fairly weak vdW adhesion as expected from Au on MoS₂. In contrast, the remaining hybrid Au/MoS₂ heterostructures show remarkably strong bonding as hinted by the reduced interatomic distances of 2.42 Å (2L), 2.54 Å (3L), 2.57 Å (5L), and 2.59 Å (6L), which are approximately a constant (variation of only 7%) in the Au layer number range of n = 2–6. We further investigated the effect of the interatomic distance in the presence of 2 layers (2L) of MoS₂ to better resemble the experimental work. Here, for a sampling, we repeated the DFT calculations for the case of 2L of Au and 2L of MoS₂. We also tested the case when graphene is in presence underneath the 2L MoS₂. The interatomic distance remains the almost the same as shown in Figure 3.3.1 a-c. This is presumably because of the relatively large distance between the Au–S position and the weak vdW interface between graphene and MoS₂. The addition of Au NPs on the multilayer MoS₂ can enhance dipole–dipole interactions at their interface, which is known to help increase SERS assuming the impact of graphene will be similar for these samples. The agreement between the simulation and experimental observation obtained in this work is therefore interesting to the design of high-sensitivity SERS substrates based on the heterostructures of plasmonic metal nanostructures/MoS₂/graphene. Baia et al. experimentally investigated the dependence of the R6G peak intensities on the size of the Ag NPs. Ag films with nominal thicknesses of 1, 2, 3, 4, 5, and 6 nm were used to obtain the Ag NPs with different diameters. The EM enhancement increases with increasing size of Ag NPs. However, the EM enhancement of substrates with Ag nominal thickness of 1 and 2 nm (Ag NP diameter in the range of 8–20 nm) was much weaker than that with larger thicknesses in the range of 3–6 nm (Ag NP diameter in the range of 30–55 nm). Furthermore, they found that the EM enhancement decreases with increasing the gap between Ag NPs [77].

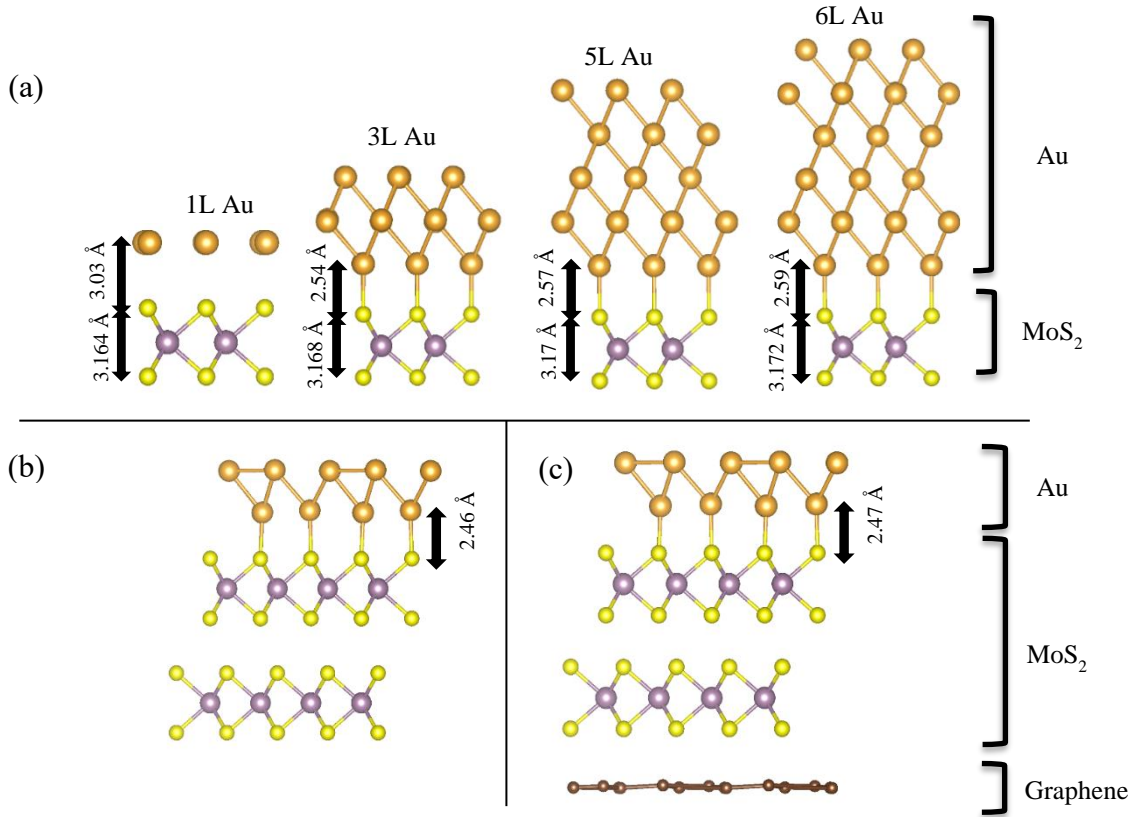


Figure 3.3.1 (a) The atomic layer stacks of Au/MoS₂ hybrid heterostructures with different numbers of Au layers of 1L, 3L, 5L and 6L on monolayer MoS₂. The interface distance between the two materials is also illustrated. The atomic layer stacks of 2L Au/2L MoS₂ hybrid heterostructures (b) without graphene layer, and (c) with graphene layer.

Figure 3.3.2 shows the 3D plots of the electron localization function (ELF) in the same hybrids of Au/MoS₂ heterostructures using the same contour range of 0.1–0.75. It should be noted that the ELF has a normalized scale of 0–1. The higher values (more red) are indicative of more localized electrons. The ELF plots from Figure 3.3.1a shows a consistent picture in that there is limited electron delocalization placed at the interface when only a monolayer of Au is present. The level of electron delocalization in the presence of thicker Au layers (2L or higher L's) is remarkably higher than that in the monolayer Au case and remains relatively the same up to 6 layers, which is consistent with the minimal change in the bond length at the interface of $n = 2-6$. In addition, an

asymmetry in the ELF (red area) surrounding the top sulfur atoms tilted toward the interface for a monolayer Au, while at larger Au layer thicknesses, a clear “C-shape” red contour structure connecting S to Mo can be seen, indicating that the strengthened Au-S bonding may have partly resulted from the weakening of the Mo-S internal bond with the 2D structures when the Au layers get thicker. This is also reflected in the slight increase, on average, of the thickness of the MoS₂ 2D layer marked by the interatomic distance between the two S layers (see Figure 3.3.3).

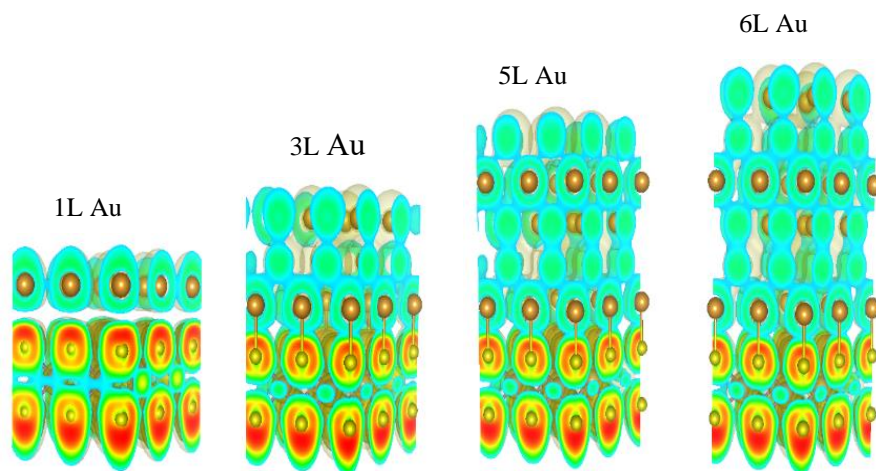


Figure 3.3.2 The 3D ELF plots of the same hybrid AuNP/ MoS₂ heterostructures shown in Figure 3.3.1a.

Figure 3.3.3 shows the difference in the density of states (DOS) for the case of the Au monolayer versus the Au double layers. Specifically, we compare the partial DOS of the d-orbitals from the Au atom at the interface. By comparison of Figure 3.3.3 a,b, it has been found that the d-band's contribution from d_z^2 (green line) which would orientate spatially toward the S atoms is much broader, extending to 8 eV below the Fermi level in Au 2L, in contrast to 5 eV below the Fermi level for the Au 1L. The same, to a lesser extent, can be observed with the d_{xz} and d_{yz} orbitals. This DOS broadening of the z-containing d bands can be understood from the fact that the d orbitals

are overlapped with the p orbitals from the terminating S atoms. As shown in Figure 3.3.3c for Au 1L, the local DOS contribution from S atoms (which also overlaps with Mo atoms as expected) spans up to the same extended energy range. This again confirms the enhanced bonding beyond the normal vdW expected at the Au/MoS₂ interface with 2L or thicker Au. The DOS for thicker Au (3-6 layers) are almost similar. For example, the d-band's contribution from d_z^2 extended to ~8 eV for Au of thickness in the range of 2L-6L. As already mentioned, the main effect as far as the electronic structures as concerned between 1L and 2L of a stand-alone 2D structure of MoS₂ is the change that is associated with the switch from direct (of 1.9 eV) band gap to (smaller) indirect [78]. We should note that the band gap resulting from DFT calculations here using nonhybrid potentials in general is typically underestimated, which is a known effect [79]. Our goal here is mainly to highlight the role Au layers and bonding interactions between Au and terminating S atoms from MoS₂. Previous study has shown that as you increase the number of layers of MoS₂ 2D structure, there is a reduction of the conduction band states and their minimum position in the vicinity of the Γ point (along the $\Gamma \rightarrow K$ direction) [78]. This decrease in the conduction band minimum results in the switch to a smaller direct band gap at the K point to the indirect band gap near halfway of $\Gamma \rightarrow K$. Indeed, as you further increase the number of layers, the band gap will continue (gradually) to reduce and form the reported small band gap of 1.29 eV for a bulk MoS₂. Because all of the samples being used here have relatively the same thickness, i.e., 2L or slightly thicker, a similar effect of a slightly reduced band gap (relative to that of monolayer MoS₂) will be observed for all of the samples, presumably providing relative ease for the charge transfer to take place in comparison, for example, if we were to use a single-layer MoS₂. Nevertheless, the main effect is still the increased hybridization at the top of the MoS₂ layer facilitated by the bonding between the S atoms and the multiple layers of Au.

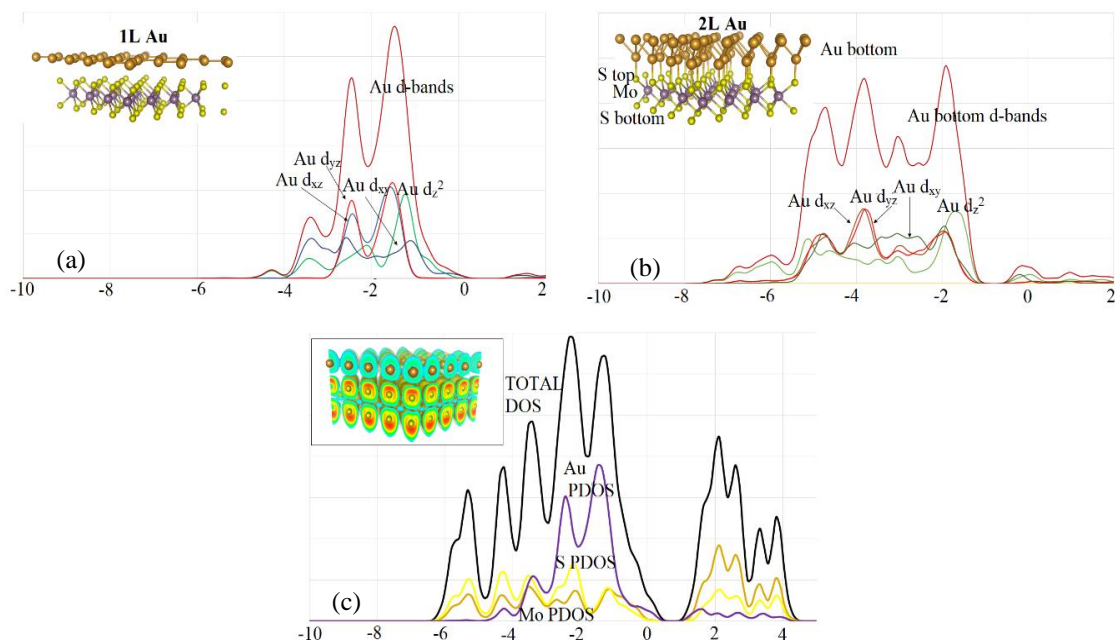


Figure 3.3.3 Comparison on the local DOS of Au atoms for (a) 1L, (b) 2L from the different types of occupied d orbitals, namely d_{xy} , d_{xz} , d_{yz} , d_{z^2} is minimally occupied. The total DOS and each atom-specific contribution for 1L is also shown in (c) The zero point for the energy range is Fermi Energy E_{Fermi} .

We found that the MoS₂/graphene vdW heterostructures showed stronger Raman enhancement effect compared to individual layer of graphene or MoS₂ and the SERS sensitivity reached up to 5×10^{-8} M R6G which is comparable to that of plasmonic AuNPs/graphene SERS substrate. In addition, the theoretical analysis of a MoS₂ flake of a total of 324 atoms on graphene sheet comprised of 288 atoms (Figure 3.3.4a) has been done. The ELF provided a quantitative measure of the spatial delocalized bonds within the hybrid structure (Figure 3.3.4 b). The localized electron concentration below the sulfur atom indicating the charge transfer occurrence.

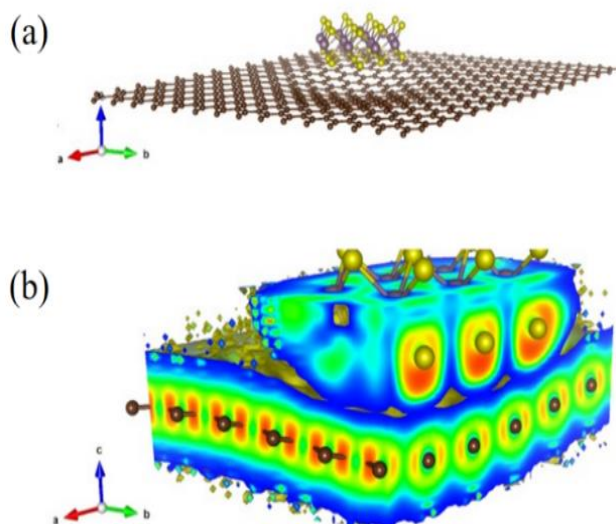


Figure 3.3.4 (a) Vertical MoS₂/graphene bilayer heterostructure. (b) Electron Localization Function (ELF) of the MoS₂/graphene vdW heterostructure.

The optical transmission spectra of the graphene, MoS₂/graphene, and AuNPs/MoS₂/graphene samples over the wavelength range of 400–800 nm were taken to confirm the plasmonic resonance associated with the AuNPs, and the results are illustrated in Figure 3.3.5a. The spectra for the graphene and MoS₂/graphene samples show high transparency with the minimum optical transmittance of ~97% and 90%, respectively (Figure 3.3.5b,c), in the spectral range studied. In contrast, the spectrum AuNPs/MoS₂/graphene shows a broad valley with much reduced transmission between 550 and 700 nm, indicating surface plasmonic resonance near the resonance frequencies at frequency of 650 nm due to the LSPR enhanced the light absorption in the AuNPs where the average size of AuNPs is ~50 nm in diameter. In AuNPs/graphene with average size of 40 nm, the LSPR wavelength is ~570 nm [37] and ~535 nm for MoS₂/AuNPs [80] with an average

size of 6 nm. However, the broad LSPR peak is not a surprise considering the large range of the AuNP dimension formed on MoS₂/graphene samples via self-assembly [38].

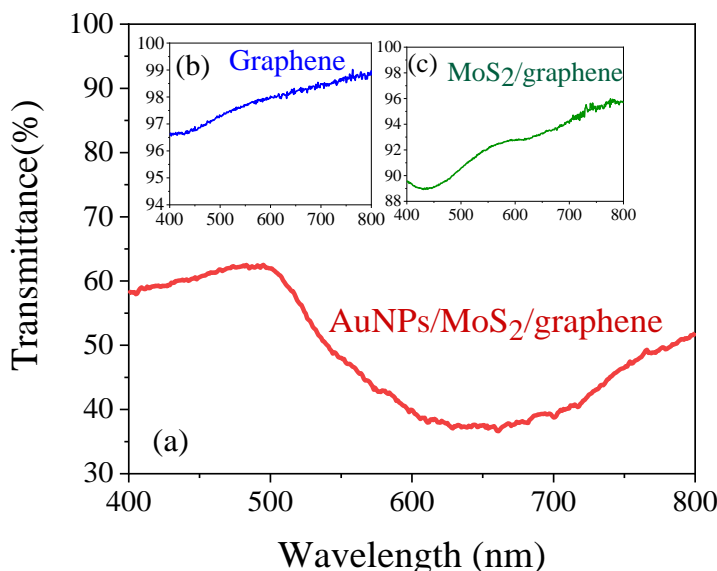


Figure 3.3.5 (a) Optical transmittance spectra of multiple materials on fused silica. (a) AuNPs/MoS₂/graphene, (b) graphene, and (c) MoS₂/graphene.

In Figure 3.3.6, the Raman spectra of R6G (5×10^{-5} M) taken on different substrates are compared. A significant difference in the peak intensity of the R6G Raman signatures on different substrates is illustrated. On the single layer MoS₂ substrate (black), the R6G peaks are not visible, which is not surprising since a semiconductive MoS₂ layer is not expected to have visible CM and EM enhancement. In contrast, the R6G Raman signature peaks can be clearly seen on graphene substrate (red), most probably due to the SERS enhancement via the CM mechanism [66, 68]. Interestingly, further improved R6G signals can be observed on the MoS₂/graphene heterostructure substrate (blue), confirming the further enhanced CM effect predicted in theory through the vdW interaction at the MoS₂/ graphene interface [73]. With decoration of the AuNPs on the

MoS₂/graphene heterostructure substrate (purple), the R6G Raman signals are dramatically enhanced, which can be attributed to the combined benefits of the EM enhancement by the plasmonic AuNPs and the CM enhancement from the MoS₂/graphene vdW heterostructure. Most importantly, this R6G SERS enhancement on the AuNPs/MoS₂/graphene vdW heterostructure is much more significant than on the AuNPs/graphene (green) substrate with similar AuNPs made in the same process on graphene, indicating the interlayer coupling in the hybrid AuNPs/MoS₂/graphene heterostructure indeed plays an critical role in further enhancing the CM effect [81, 82]. Therefore, the Raman signals of R6G on AuNPs/MoS₂/graphene substrate have the highest SERS effect among the five substrates tested in Figure 3.3.6 due to the combination of the EM and CM enhancements [83] arising from AuNPs/MoS₂/graphene heterostructure with the EM enhancement by AuNPs dominating the enhancement [84, 85]. Additional spectral features of R6G, such as R6G peak at $\sim 1088\text{ cm}^{-1}$ in Figure 3.3.6, can be detected only at higher SERS

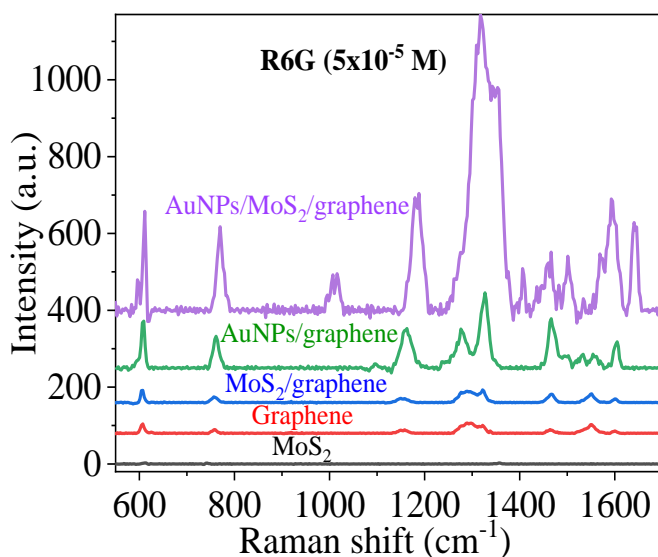


Figure 3.3.6 R6G Raman spectra of 5×10^{-5} M concentration with different substrates: AuNPs/MoS₂/graphene (purple), AuNPs/graphene (green), MoS₂/graphene (blue), graphene (red), and MoS₂ (black).

enhancement on AuNPs/MoS₂/ graphene SERS substrates. All SERS measurements were taken at a low level of the laser power (~1 mW) to avoid any damage to the R6G molecules.

Figure 3.3.7 shows the SERS measurements at different laser power to illustrate the effect of exciting laser power on Raman signals of the R6G molecules. Raman signals increase with increasing laser power (0.05–0.2 mW) and saturated (0.5–5 mW). The decrease in the R6G signals at a higher power (at 10 mW) is attributed to the damage of the molecules during the collection time of 3s. To get reasonable measurements and avoiding molecules damage, a laser power of 1 mW was selected.

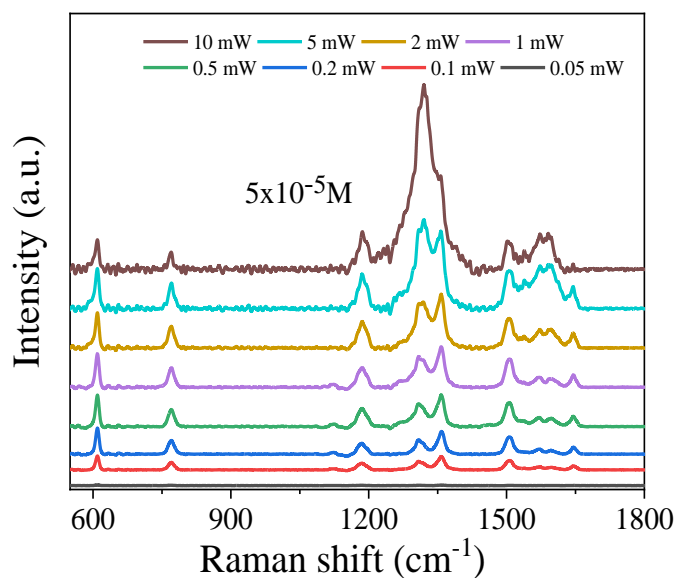


Figure 3.3.7 Raman spectra of the R6G taken by the 633 nm laser with different laser powers (0.05 mW to 10mW).

The R6G Raman spectra of different R6G concentrations on AuNPs/MoS₂/graphene are shown in Figure 3.3.8. These spectra were obtained with both a nonresonance 633 nm excitation (Figure 3.3.8a) and a resonance 532 nm (Figure 3.3.8b) laser. While a higher Raman sensitivity can be typically obtained at the resonance of the probe molecules, the nonresonance excitation provides the practical limit of the SERS sensitivity for a large variety of the molecules that may not have compatible resonance excitations available for SERS. The characteristic Raman peaks of R6G are clearly visible with both types of excitations. Specifically, the 612 cm⁻¹ peak is assigned to C–C–C ring in-plane vibration, 769 and 1088 cm⁻¹ peaks to the C–H out-of-plane bend, 1184 cm⁻¹ peak to C–C stretching vibrations, and the 1320 and 1502 cm⁻¹ peaks to the N–H in plane bend, while the 1361, 1502, and 1663 cm⁻¹ peaks are assigned to C–C stretching [86, 87]. The intensity of R6G Raman peaks decreases monotonically with the R6G concentration. The minimum detectable R6G concentration on the AuNPs/MoS₂/graphene substrate using 633 nm laser is about 5×10^{-8} M, at which not all R6G peaks are observable as shown in Figure 3.3.8a. A lower concentration of 5×10^{-9} M was also tested, but no Raman signal could be detected for R6G. It should be noted that the R6G sensitivity of 5×10^{-8} M on the AuNPs/MoS₂/graphene substrates is about an order of magnitude higher than that of the AuNPs/graphene substrates reported previously [37]. Thus, this result illustrates that inserting a MoS₂ layer between the AuNPs and graphene can improve the SERS sensitivity by enhancing the CM effect through interface electronic structure modification of the AuNPs/ MoS₂/graphene vdW heterostructures. In Figure 3.3.8b, the R6G detection limit of 5×10^{-10} M is obtained using the resonant excitation wavelength of 532 nm, which is one order of magnitude higher than that reported on the AgNPs/MoS₂ substrate using a 532 nm laser [74].

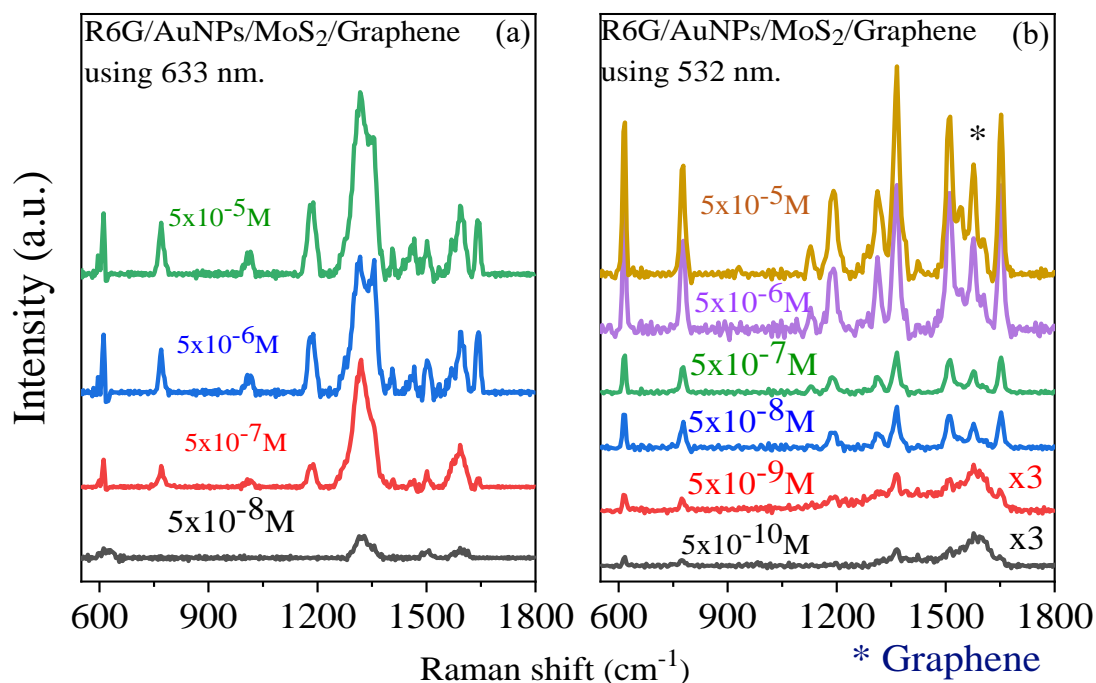


Figure 3.3.8 Raman spectra of the R6G molecules with different concentrations cast on the AuNPs/MoS₂/graphene hybrid using (a) 633 nm laser and (b) 532 laser. Spectra of concentrations 5×10^{-9} M and 5×10^{-10} M were multiplied by factor of 3.

In addition, the Raman spectra of the R6G on AuNPs/MoS₂ were collected as shown in Figure 3.3.9 a with lower sensitivity of about 5×10^{-7} M (Figure 3.3.9 a) and 5×10^{-9} M (Figure 3.3.9 b), respectively using 633 and 532 nm lasers. The AuNPs on MoS₂/graphene heterostructure substrate shows a higher enhancement compared to AuNPs on graphene or MoS₂ only.

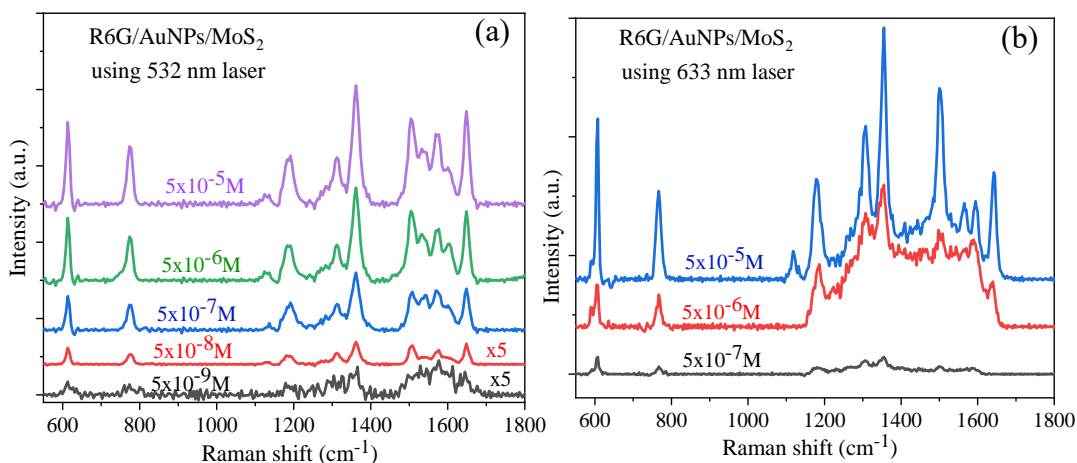


Figure 3.3.9 Raman spectra of the R6G molecules with different concentrations cast on the AuNPs/MoS₂ hybrid using (a) 532 laser. Spectra of concentrations 5×10^{-8} M and 5×10^{-9} M were multiplied by factor of 5. (b) 633 nm laser.

A quantitative analysis was made on three distinct peaks of the R6G at 612 , 767 , and 1184 cm^{-1} to investigate the relationship between the Raman intensity and the concentrations of the R6G molecules with 633 and 532 nm laser excitation. Figure 3.3.10a-c show a linear relation between the Raman peaks intensity as a function of the R6G concentrations. The Raman peaks intensity saturate as the concentration of the R6G is increased. Figure 3.3.10d-f replot the data in the Figure 3.3.10a-c on a log scale, illustrating a good linear relationship between SERS intensity and the R6G concentrations. The trends indicate that the Raman signals intensity decrease with the decreasing R6G concentration as has been reported in several studies [88, 89].

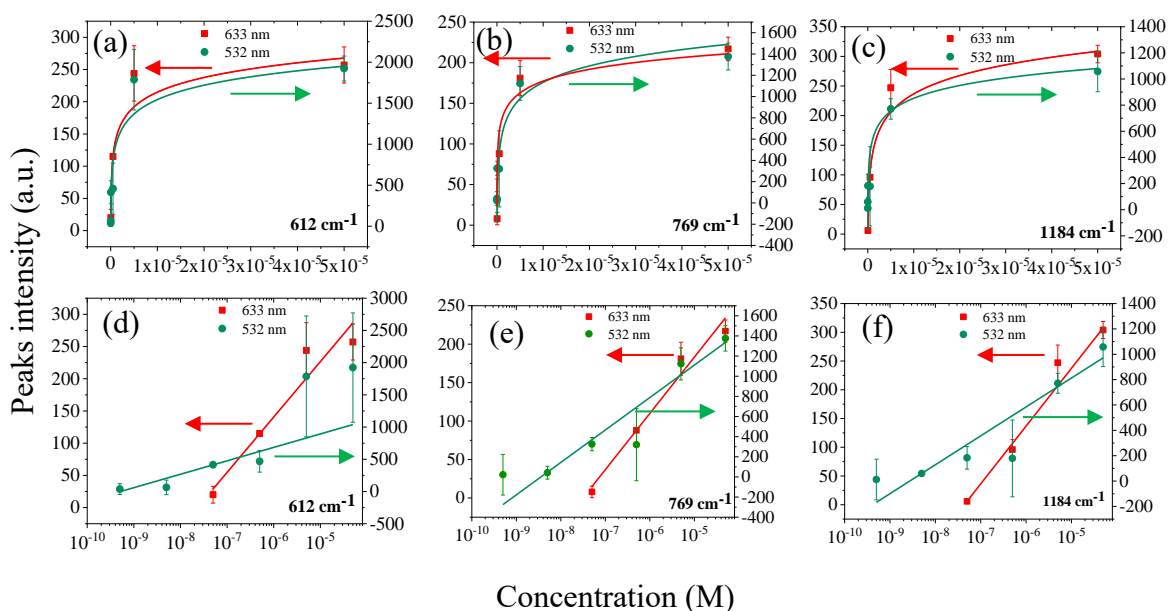


Figure 3.3.10 The intensities of the Raman peaks as a function of the R6G concentrations. at (a,d) 612 cm^{-1} , (b,e) 769 cm^{-1} , and (c,f) 1184 cm^{-1} for the AuNPs/MoS₂/graphene substrates using both 633 nm laser (red) and 532 nm laser (green). (d, e, f) was plotted using a logarithmic scale.

3.3.2 Conclusion

In conclusion, this work reports a new SERS substrate based on plasmonic AuNPs decorated 2D MoS₂/graphene vdW heterostructures made using a transfer-free layer-by-layer process, which has advantages for scale-up to large wafers as well as clean interfaces for optimal charge transfer across the interfaces in the AuNPs/MoS₂/graphene vdW heterostructures. Using R6G as probe molecules, we investigated the SERS sensitivity using both nonresonant excitation of a 633 nm laser and a resonant 532 nm laser. In the former, the R6G SERS sensitivity of $5 \times 10^{-8}\text{ M}$ was obtained, which is an order of magnitude higher than the best reported on AuNPs/ graphene substrates. This enhancement may be attributed to the enhanced dipole–dipole interaction at the Au/MoS₂ interface at large Au thickness in exceeding two monolayers as revealed in the DFT simulation. This enhanced interface interaction results in enhanced electron delocalization and

hence enhanced CM contribution to SERS signatures. By use of resonance excitation of a 532 nm laser, a higher SERS sensitivity of 5×10^{-10} M was achieved for R6G on AuNPs/ MoS₂/graphene substrates, which is also an order of magnitude higher than that reported on AgNPs/MoS₂ substrate using the same 532 nm excitation. This result illustrates a pathway in design high-performance SERS substrates based on 2D vdW heterostructures for optimal CM contribution to SERS, which can be combined with the plasmonic metal nanostructures, such as AuNPs in this work, for high-sensitivity SERS.

4 Chapter 4: WS₂ Nanodisks /Graphene van der Waals Heterostructure Photodetectors

4.1 Photodetection background

Photodetectors are optoelectronic devices that convert the incident photons into electrical signals. The semiconductor materials, in photodetectors, can absorb the incident photons with energy equal to or greater than their band gap (E_g) and produce electron-hole pairs. The generated electron-hole pairs are separated by the "built-in" electric field or the applied electric field and produce an electric current (photocurrent). The 2D materials could overcome the drawback of the traditional semiconductors such as silicon (Si), germanium (Ge) and indium gallium arsenide (InGaAs), including low carrier mobility, inflexibility, and the required large thickness for incident light absorption.

Several important figures-of-merit are used to characterize photodetectors performance and enable the comparison between different devices. These figures-of-merit include responsivity, detectivity, the external quantum efficiency (EQE), response time, etc. The responsivity is very important figures-of-merit for photodetectors characterization. It is defined as the ratio of photocurrent to power of the incident light to determine how efficiently photodetectors respond to an optical signal. More details about these figures-of-merit will be discussed in result and discussion section in this chapter.

4.1.1 Photodetection mechanism

Various physical mechanisms are responsible for photodetection such as photoconductive effect, photovoltaic effect, and photo-thermoelectric effect. In this thesis, we exclusively focus on photoconductive effects mainly photogating effect as it is the dominant mechanism in our devices.

Basically, the photogating effect (special case of the photoconductive effect) is based on light-induced modification of the carrier density. This effect is mostly observed in semiconductor/graphene hybrid. For example, in QDs/graphene hybrid the photocarriers are generated in QDs upon light illumination where one type of carrier transfers to graphene and the other remains trapped in the QDs. The injected photocarriers into graphene are circulate multiple times between source and drain electrodes before they recombine with the trapped carriers in the QDs. That allow one single photon to produce multiple photocarriers resulting in extremely high photoconduction gain.

4.2 2D materials and their heterostructures for photodetection

Photodetectors based on two-dimensional (2D) materials, such as graphene and TMDCs, have received considerable attention recently because of their promising electronic and optical properties. Specifically, vdW heterostructures of graphene and photoactive 2D materials such as TMDCs provide a promising scheme to design high-performance photodetectors that combine the advantage of enhanced light absorption in 2D atomic layers of TMDCs and high charge mobility in graphene. For example, in the TMDC/graphene vdW heterostructure photoconductors, the TMDC layer absorbs the incident light and the generated electron-hole pairs or excitons can be dissociated to free carriers by the built-in electric field at the TMDC/graphene interface. Transferring carriers to graphene can be also facilitated by the interface built-in field, resulting in a photogating effect on graphene, and hence photoresponse as the graphene channel conductivity changes [90] The high mobility of graphene gives rise to a very short transit time (τ_{transit}) of the charge carriers within the life time of the excitons (τ_{exciton}), resulting in a high photoconductive gain, which is proportional to the ratio of the τ_{exciton} and τ_{transit} , up to 10^8 to 10^9 [91-94]. Various

reports have demonstrated high performance of the TMDCs/graphene vdW heterostructures photodetectors [33, 95, 96]. The visible photoresponsivity up to 835 mA/W has been reported for a photodetector based on printed MoS₂ on transfer-free graphene [33]. The high performance of this device is attributed to a clean interface between MoS₂ and the transfer-free graphene. However, a higher photoresponsivity can be obtained by applying a gate voltage to better align the electronic structure at the vdW interface for more efficient free carrier transfer. For example, Xu et al. reported photoresponsivity of 10 A/W on the MoS₂/graphene phototransistor by application of a back-gate voltage $V_{BG} = -20$ V to facilitate the transfer of photo-excited holes from the MoS₂ layer to graphene [90]. This is in contrast to the lower photoresponsivity of 4.3 A/W at $V_{BG} = 0$ V. Interestingly, all of these TMDC/ graphene heterostructure devices provide much higher performance than those based on the TMDCs or graphene only. For example, the reported responsivities are 18.8 mA/W on monolayer WS₂ photodetectors under a gate voltage of 60 V,[97] 7.5 mA/W on monolayer MoS₂ photodetectors at a gate voltage of 50 V, [98] and less than 1 mA/W on bilayer [99, 100] and single-layer graphene photodetector [101]. This illustrates the unique advantage of the TMDC/graphene vdW heterostructures in achieving optimal optoelectronic process of light absorption, exciton dissociation, carrier transfer, and transport through introduction of graphene with high charge mobility. However, light absorption in TMDC/graphene vdW heterostructures is still limited because of the small thickness of the TMDC as the photosensitizer. In fact, the limited light absorption issue represents a fundamental challenge in optoelectronic devices that only use a thin layer of sensitizer, such as QDs of typical diameter of a few nanometers and 2D materials of thickness in the similar range or smaller [33, 93-95, 102-104].

4.3 WS₂ Nanodisks /Graphene van der Waals Heterostructure Photodetectors

Development of new approaches for light trapping is critical to enhance the performance of photodetectors devices. In this work, we report a novel photodetector based on a WS₂ nanodisks (NDs)/graphene vdW heterostructure. We show that the WS₂-NDs with a lateral dimension in the range of about 200–400 nm allows localized surface plasmonic resonance (LSPR) to be generated upon light illumination and hence photo-doping, enabling enhanced light absorption and hence photoresponsivity. Furthermore, the WS₂-NDs were synthesized on transfer-free graphene directly grown on SiO₂/Si substrates using CVD, which is critical to obtain a clean vdW WS₂-NDs/graphene interface to facilitate charge transfer. On the WS₂-NDs/graphene photodetectors, enhanced photoresponsivity by at least seven times has been demonstrated as compared to the continuous WS₂ layer on graphene (WS₂-CL/graphene) heterostructure counterparts’.

4.3.1 Results and Discussions

Figure 4.3.1a shows the schematic diagram of the WS₂-NDs/ graphene vdW heterostructure photodetector with the source and drain electrodes. Under light illumination, the photoexcited electron–hole pairs are generated in the WS₂-NDs and separated at the WS₂-NDs/graphene interface because of the built-in electric field [105]. In the WS₂-NDs, a strong LSPR can be induced via carrier doping of semiconducting WS₂-NDs as depicted schematically in Figure 4.3.1b. This results in enhanced light–solid interaction and hence light absorption in WS₂-NDs as compared to the case of the WS₂-CL. Figure 4.3.1c illustrates the electronic band diagrams of the WS₂-NDs and the p-doped graphene at their interface. The p-type doping effect in CVD graphene is common because of adsorbed polar molecules such as H₂O on graphene in ambient conditions [93, 94, 106].

Based on the interface band diagram, the holes dissociated from electron– hole pairs are injected into graphene and the electrons remain trapped in the WS₂-NDs before they recombine with holes. After the transfer, the holes will drift along the graphene channel with high mobility between source and drain electrodes under a bias voltage (V_{sd}) with a short transit time $\tau_{transit}$, which is given by [91]

$$\tau_{transit} = \frac{L^2}{\mu V_{sd}} \quad (12)$$

where L is the graphene channel length and μ is the carrier mobility. The trapped electrons in the WS₂-NDs have the exciton lifetime $\tau_{exciton}$ that is significantly longer than the $\tau_{transit}$ due to the quantum confinement in the WS₂-NDs and high carrier mobility of graphene, allowing the holes to circulate multiple times before they recombine with electrons. Consequently, a high photoconductive gain (G) defined by

$$G = \tau_{exciton} / \tau_{transit} \quad (13)$$

can be achieved.

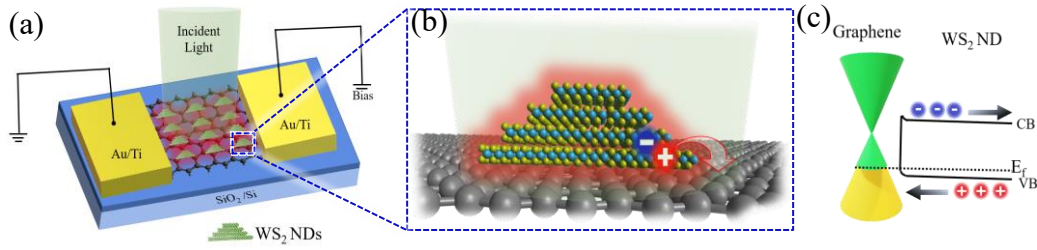


Figure 4.3.1 (a) Schematic illustration of the photodetector based on WS₂-NDs/graphene vdW heterostructure. (b) A zoom-in view of the WS₂-NDs/graphene photodetector with an illustration of the charge transfer process at the vdW interface. (c) Electron band diagram of p doped graphene and the WS₂-NDs (E_f : the Fermi level, CB: conduction band, and VB: valence band).

Figure 4.3.2a shows the I–V characteristic curve of the WS₂-NDs/graphene photodetector in the dark (black) and in response to illumination (at 550 nm) (green) with a fixed optical power of 100 μ W. The illuminated current increases linearly as the bias voltage varies from 0 to 6 V because of the increase in carrier drift velocity and the decrease in transit time of the carrier between the electrodes [107]. The linear I–V curve indicates an Ohmic contact between the heterostructure and electrodes. The difference between the illuminated and dark currents is defined as photocurrent ($I_{ph} = I_{light} - I_{dark}$) Figure 4.3.2b shows the dynamic photocurrent in response to light on and off at different bias voltages and different illumination powers at 550 nm. The photocurrent decreases with decreasing both the bias voltage and the power of the incident light, which is attributed to the decreased number of photogenerated exciton (electron–hole pairs) as the incident optical power decreases from 12 to 0.15 μ W. Figure 4.3.2c illustrates the dynamic photocurrent in response to multiple pulses of the 550 nm light illumination, illustrating a fast and stable photoresponse. The temporal photoresponse of the photodetector is characterized by a typical rise and fall time (t_{rise}

and t_{fall}). The t_{rise} is the required time for photocurrent to rise from 10 to 90% of its maximum and the t_{fall} is the time the photocurrent takes to decay from 90 to 10% [108]. For the WS₂-NDs/graphene devices, the $t_{\text{rise}} = 10$ ms and $t_{\text{fall}} = 20$ ms at $V_{\text{sd}} = 5$ V is depicted in Figure 4.3.2d by the magnified part from Figure 4.3.2c, which is slightly faster than MoS₂-CL/transfer-free graphene (20–30 ms) [33] under the same conditions and also faster than MoS₂/transferred-graphene (3.2–1.2 s) [108]. To elucidate the impact of the LSPR effect in the WS₂-NDs/graphene on the performance of the photodetectors, a comparative study of the photoresponse was carried out on the WS₂-NDs/graphene photodetectors with different WS₂-ND areal density and WS₂-CL/graphene photodetectors. The photodetectors are fabricated and measured under the same conditions.

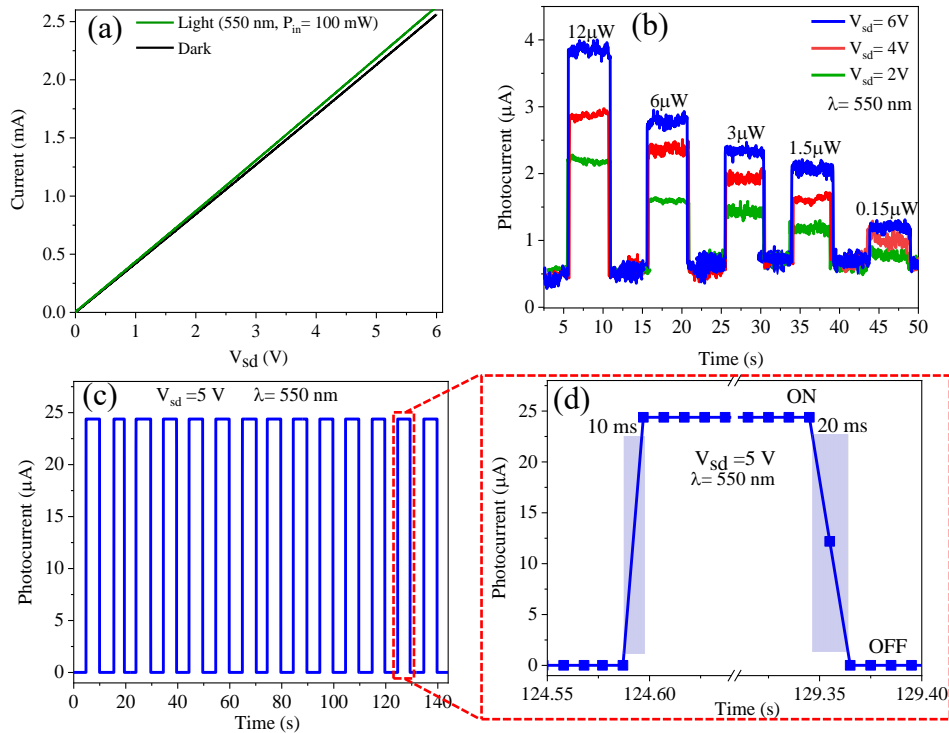


Figure 4.3.2 (a) I–V characteristics measured in the dark and upon 550 nm illumination at $V_{\text{sd}} = 0\text{--}6$ V. (b) Photoresponse of the device at various bias voltages under various incident optical power. (c) Dynamic photocurrent measured in response to 550 nm light ON and OFF for WS₂-NDs/graphene photodetector. (d) The enlarged part of (c).

Figure 4.3.3a-f illustrates the optical images and Raman maps for the WS₂ on graphene: with higher WS₂-NDs areal density (a,b), lower WS₂-NDs areal density (c,d), and WS₂-CL (e,f). The dynamic photoresponse and photoresponsivity of these three samples are compared in Figure 4.3.3g,h. The highest measured values for photocurrent and the photoresponsivity (23 μA, 6.4 A/W) were observed on the WS₂-NDs/graphene sample with denser and smaller lateral size (200–400 nm). In the case of a less dense and larger size WS₂-NDs (~500–1200 nm) shown in Figure 4.3.3c,d, the photocurrent and the photoresponsivity are decreased to 18 μA and 2.5 A/W, respectively. The lowest measured values for the photocurrent (11 μA) and the photoresponsivity (0.912 A/W) were found on the photodetector with a continuous layer of WS₂ on graphene, Figure 4.3.3e,f. The obtained values demonstrate the dependence of photocurrent and photoresponsivity on the WS₂ morphology. The photodetector with smaller and denser WS₂-NDs shows a better performance. The observed photoresponse in this work is because of the photogating effect. In the presence of the LSPR effect on the WS₂-NDs, the enhanced light absorption by the WS₂-NDs would result in higher photogating effect and hence photoresponse. We attributed the superior performance of WS₂-NDs/graphene photodetector to enhanced photogating effect because of the LSPR effect generated by WS₂-NDs. The photoresponsivity (R) is an important figure-of-merit for a photodetector and is defined as [108], where P_{in} is the illumination power.

$$R = \frac{I_{ph}}{P_{in}} \quad (14)$$

where P_{in} is the illumination power.

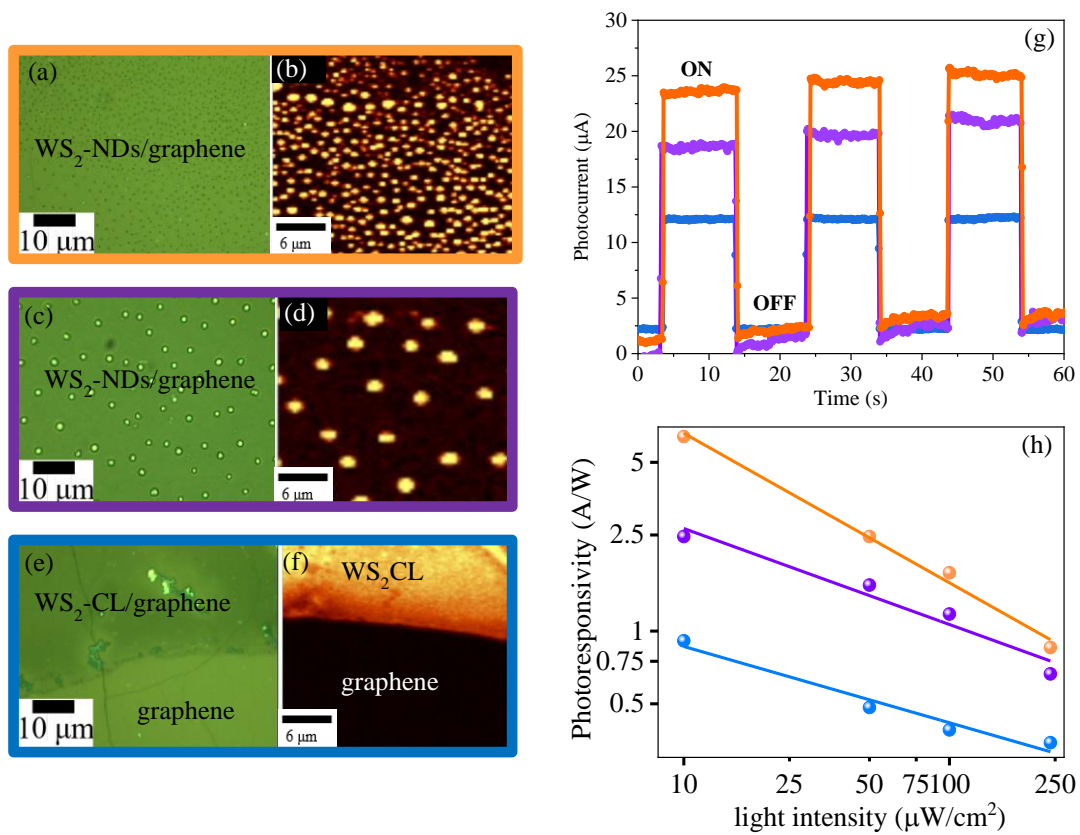


Figure 4.3.3 (a,c,e) Optical and (b,d,f) Raman mapping images of WS₂ with smaller and denser WS₂-NDs in WS₂-NDs/graphene (orange); larger and more dilute WS₂-NDs WS₂-NDs/graphene (purple) samples, and WS₂-CL/graphene (blue). (g) The corresponding dynamic photocurrents measured in response to 550 nm light on and off and (h) photoresponsivity as a function of the incident light intensity on the three devices.

Figure 4.3.4a,b compare the R values measured on WS₂-NDs/graphene and WS₂-CL/graphene devices as a function of incident light intensity. The R values of both devices decrease monotonically with increasing incident power, while the photocurrent increases with increasing the power of incident light. The decrease in the R value is ascribed to the decreasing of charge carrier concentration which result in a lower e-h recombination [33]. At lowest power density of 10 μW/cm², the WS₂-NDs/graphene photodetector has a photoresponsivity of 6.4 A/W, which is

seven times higher than the 0.91 A/W on the WS₂-CL/graphene counterpart. This illustrates the impact of the enhanced light absorption in WS₂-NDs as compared to the WS₂-CL. It should be noted that the R values on the WS₂/graphene vdW heterostructure photodetectors are considerably higher than that reported for WS₂ (0.0188 A/W) [97] and for graphene (0.0061 A/W) [100]. Figure 4.3.4c illustrates photocurrent response of both photodetectors to light illumination ($\lambda = 550$ nm) at a bias of 5 V. The enhancement of photocurrent is clearly observed. The optimized performance of the WS₂-NDs/graphene photodetector can be attributed to the LSPR of WS₂-NDs. The spectral photoresponsivity of the WS₂-NDs/graphene and WS₂-CLs/graphene photodetectors are compared in Figure 4.3.4d. Overall, the photoresponsivity over the entire wavelength range of 400–800 nm is higher in the WS₂-NDs/graphene devices as compared to that of the WS₂-CLs/graphene. This enhanced photoresponsivity is attributed to the enhanced light absorption by the LSPR WS₂-NDs. It should be noticed that a broad peak of photoresponsivity is present at ~500–550 nm, most probably corresponding to the LSPR wavelength of the WS₂-NDs upon photodoping. The results revealed that the LSPR WS₂-NDs can provide promising photosensitizers for enhanced performance in vdW photodetectors.

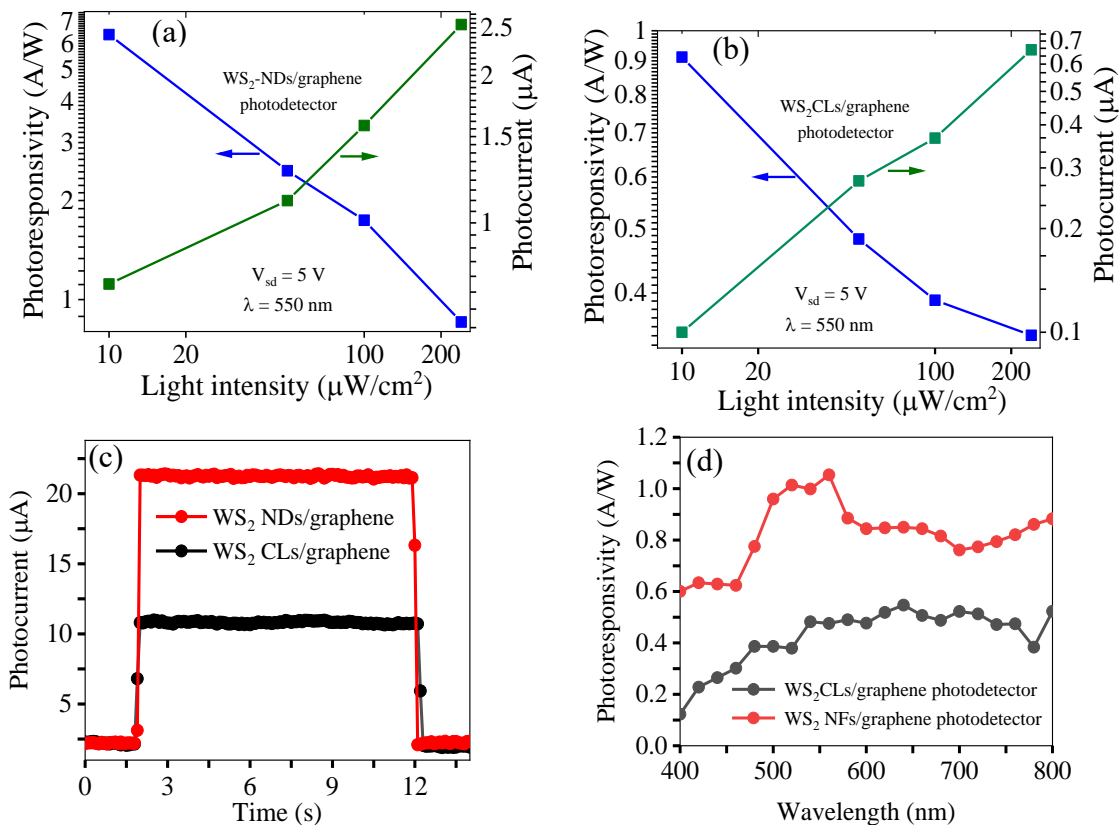


Figure 4.3.4 Photoresponsivity and photocurrent as a function of the incident light intensity of (a) the WS₂-NDs/graphene heterostructure photodetector; and (b) WS₂-CLs/graphene photodetector. (c) The dynamic photoresponse of the WS₂-NDs/graphene heterostructure photodetector (red) and WS₂-CLs/graphene photodetector (black) measured in response to 550 nm. (d) Spectral photoresponsivity of the WS₂-NDs /graphene photodetector (red) and WS₂-CLs /graphene photodetector (black).

Figure 4.3.5a displays the reduction of the photocurrent as the light power decreases from 12 to 0.15 μW, measured at a 5 V bias and 550 nm illumination. The photocurrent reduction is due to the decrease of photo-generated excitons and hence free carriers. The measured external quantum

efficiency (EQE) of the WS₂-NDs/graphene photodetector is illustrated in Figure 4.3.5b. The EQE can be calculated by [105],

$$EQE = \frac{(I_{ph}/e)}{(P_{in}/h\nu)} \quad (15)$$

where h is Planck's constant, ν is the frequency of incident light, and e is the electron charge. An EQE of 1800% was observed at the lowest power intensity and it decreases with increase the power intensity. The detectivity (D^*) is another figure of merit of photodetectors and it can be defined as [91],

$$D^* = \frac{A^{1/2}}{NEP} = R A^{1/2} / i_n^{2^{1/2}} \quad (16)$$

where A is the active area of the device, NEP is the noise equivalent power, and i_n^2 is the noise current. We assume that the total noise limiting the detectivity is dominated by shot noise from I_{dark} , hence the D^* can be expressed as [105],

$$D^* = R \left[\left(\frac{A}{2eI_{dark}} \right) \right]^{1/2} \quad (17)$$

where I_{dark} is the dark current. The calculated D^* for the WS₂-NDs/graphene photodetector was about 2.8×10^{10} Jones. The EQE and D^* were measured at a 5 V bias under light illumination of 550 nm with a light intensity of $3 \mu\text{W}/\text{cm}^2$. It should be mentioned that at this low light power density of $3 \mu\text{W}/\text{cm}^2$, the WS₂-CLs detectors did not show any measurable responses, indicating the WS₂-NDs/graphene photodetectors have larger dynamic range extending to lower light.

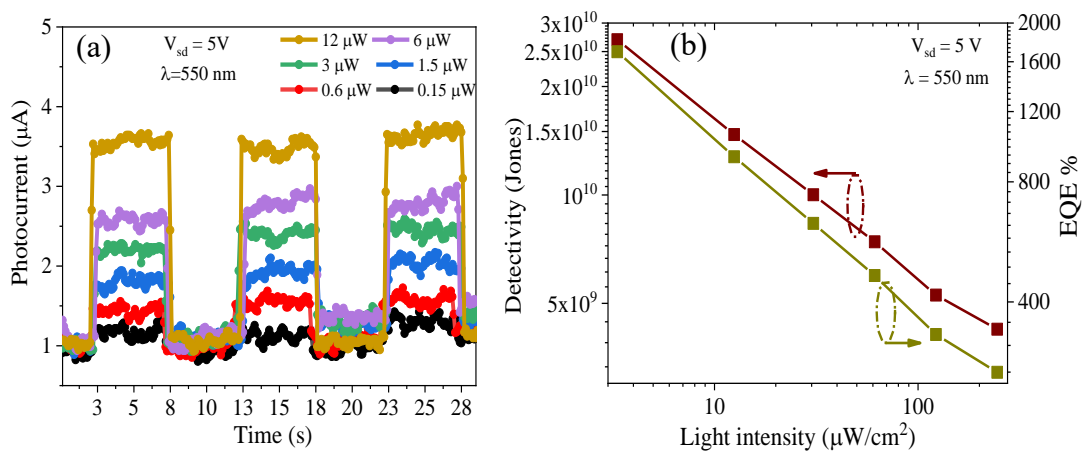


Figure 4.3.5 (a) Dynamic photoresponse of the WS₂-NDs/graphene heterostructure photodetector measured in response to 550 nm light on and off with different incident light powers; (b) The Detectivity and the EQE as a function of the incident light intensity.

The results have revealed that the TMDC-NDs/graphene photodetectors can improve the photodetection as compared to the previously reported on photodetectors based only on continuous 2D material sheets as well as on the TMDC-CLs/graphene photodetectors (Table 1).

Table 1 Comparison of the performance of photodetectors composed of graphene, 2D TMDC layers and their heterostructures.

Device structure	V _{SD} (V)	V _{BG} (V)	R (A/W)	$\tau_{\text{rise}}/\tau_{\text{fall}}$ (ms)	λ (nm)	Channel Length (μm)	Refs.
Graphene	0	60	0.001	-	632.8	1.45	[101]
WS ₂	-	20	0.0188	60/190	532	30	[97]
MoS ₂	1	50	0.0075	0/50	550	5	[98]
MoS ₂ /graphene	0.1	-20	10	280/0	632.8	~20	[90]
MoS ₂ /graphene	5	0	0.835	20/30	540	250	[33]
MoTe ₂ /graphene	-2	0	0.02	30/30	532	~10	[96]
WS ₂ -CLs /graphene	5	0	0.91	10/20	550	250	[47] our work
WS ₂ -NDs /graphene	5	0	6.4	10/20	550	250	[47] our work

4.3.2 Conclusion

In conclusion, we have successfully synthesized WS₂-NDs on transfer-free graphene using a layer-by-layer CVD process. Specifically, the WS₂-NDs with a lateral dimension of ~200–400 nm and WS₂ layer number of 4–7 were obtained by coating a very thin layer of the (NH₄)₂WS₄ precursor solution followed by annealing at 450 °C under a flow of mixed gases of Ar and H₂. In contrast, a continuous layer of WS₂ was typically obtained using a thicker precursor solution layer. Photodetectors of WS₂-NDs/graphene and WS₂-CL/graphene heterostructures were fabricated and characterized in the visible spectrum. Interestingly, the lateral confinement of the electrons in WS₂-NDs leads to a strong LSPR effect as illustrated in enhanced Raman signatures of graphene by up to 3.4 in the WS₂-NDs/graphene heterostructures, which is similar to that on the metal nanoparticles/graphene heterostructures. In contrast, no such enhancement was observed on WS₂-

CL/graphene. The LSPR effect enhances the photoresponse of the WS₂-NDs/graphene photodetectors considerably as compared to their counterparts based on the WS₂-CL/graphene. Under 550 nm light illumination of power intensity of 3 μW/cm² and bias voltage of 5 V, the WS₂-NDs/graphene photodetectors exhibited photoresponsivity of 8.05 A/W, an EQE of 1800%, and a detectivity of 2.8×10^{10} Jones. Because the light intensity of 3 μW/cm² is beyond the detection limit of the WS₂-CL/graphene photodetectors, the performance of the two photodetectors were compared at a higher intensity of 10 μW/cm² at 550 nm. The WS₂-NDs/graphene photodetectors exhibited seven-time higher photoresponsivity of 6.4 A/W than the 0.91 A/W of the WS₂-CL/graphene vdW heterostructures photodetectors. This result demonstrates the important role of the LSPR effect in enhancing the light absorption in WS₂-NDs and hence the performance of the WS₂-NDs/graphene photodetectors. Finally, the layer-by-layer transfer-free approach developed for fabrication of the WS₂-NDs/graphene heterostructures is low-cost and scalable for commercialization of high-performance optoelectronic devices.

5 Chapter 5: WS₂ Nano Disk/Graphene on plasmonic Ag Nanoparticles for Photodetection

5.1 Strategies to enhance light-matter interaction in the 2D materials for optoelectronic applications

Two-dimensional atomic materials such as graphene and TMDCs have received much attention due to their superior optical and electronic properties. The combination of graphene and TMDCs in the so-called TMDC/graphene vdW heterostructure nanohybrids can take advantage of graphene's high charge carrier mobility [109] and broadband, low optical absorption ($\sim 2.3\%$ for single-layer graphene) [3] with TMDCs' strong light absorption tunable by their band gaps [110, 111] providing an excellent scheme for the design of high-performance optoelectronic devices. In these TMDC/graphene or more generally semiconductor sensitizer/graphene nanohybrids [47, 92, 94, 96, 112-114] light is absorbed by the semiconductor photosensitizer (such as TMDCs), generating excitons or electron-hole pairs in the sensitizer. The built-in electric field at the sensitizer/graphene interface assists both exciton dissociation to free charge carriers and charge transfer from the sensitizer to graphene. The high mobility of the charge carriers in graphene leads to a very short transit time, τ_{transit} , of the transferred carriers (one type depending on the built-in field at the sensitizer/graphene interface) between the two electrodes on graphene, while the other type of charge carriers remains trapped in the sensitizer during the exciton lifetime (τ_{lifetime}). The exciton lifetime regards the time scale the electron-hole recombination occurs. The holes would be trapped in the WS₂-NDs after the electrons transfer to graphene within the exciton lifetime before the electron-hole recombination. It should be pointed out that graphene may not be a good choice as active optical materials since it does not have a band gap. However, graphene can provide

an excellent transport pathway for photoexcited carriers due to its high mobility. Therefore, a nanohybrid structure of the graphene and semiconductor material combines the advantage of the semiconductor sensitizer to absorb the incident light and graphene acts as an efficient channel to transport the photoexcited carriers. Since photoconductive gain (G) in the sensitizer/graphene nanohybrids is proportional to the ratio of the τ_{lifetime} to the τ_{transit} , G up to 10^8 – 10^{10} in the semiconductor quantum dot/graphene nanohybrid photodetectors through a combination of the strong quantum confinement in the QDs and high carrier mobility in graphene has been achieved [47, 92, 94, 96, 111-113]. Consequently, a significant improvement in photoresponse has been reported in the QD/graphene and TMDC/graphene nanohybrids [33, 94, 96]. Konstantatos et al. reported the first PbS QD/graphene nanohybrid photodetector [92]. A high gain of $\sim 10^8$ and a photoresponsivity of $\sim 10^7$ A/W in the visible spectrum were demonstrated. Comparable photoconductive gains and high photoresponsivity have also been reported in other nanohybrids [94, 112, 113]. For example, a ZnO QD/graphene nanohybrid photodetector was reported to exhibit a high ultraviolet photoresponsivity of $>10^8$ A/W due to the high gain exceeding 10^9 [94, 112]. On the MoS₂ (few-layer)/transfer-free graphene nanohybrid photodetectors, a high responsivity of 835 mA/W was reported in the visible spectrum [33]. Kuiri et al. reported a responsivity of 20 mA/W on an infrared photodetector based on MoTe₂/graphene heterostructures nanohybrids [96]. A clean interface is required between the semiconductor sensitizer and graphene for charge transfer and to establish a native electric field due to the electronic band edge alignment across the interface. Defects and impurities at the interface, which can occur especially at the vdW interface formed through mechanical stacking of the semiconductor sensitizer/graphene heterostructures, can significantly degrade the photodetector performance resulting in low and slow photoresponse. Indeed, transfer-free or post annealed TMDC/graphene vdW heterostructure

nanohybrids have exhibited fast and high photoresponse due to the significant reduction of interfacial defects [33, 47, 115]. One of the fundamental issues limiting further enhancement of the performance of the TMDC/graphene and QDs/graphene nanohybrid photodetectors is the limited light absorption due to the small thickness of the sensitizer (subnm for the monolayer TMDCs, few nm in the few-layer TMDCs or single-layer QDs). To address this issue, various approaches have been explored (Figure 5.1.1). One promising approach is implementation of plasmonic metallic nanostructures for light trapping in the vicinity of the metal surface [116-120] to enhance light absorption in the semiconductor sensitizer in close proximity. For example, the photoresponsivity of graphene was enhanced by about 400% by transferring the prefabricated AuNPs on graphene [118]. In addition, J. Miao et al. demonstrated a 3-fold enhancement of the photoresponse after AuNPs were deposited onto few-layer MoS₂ phototransistors [119]. A similar light-trapping benefit on the sensitivity of Raman spectroscopy was also reported through SERS via implementation of the plasmonic metal nanostructures on graphene [36, 37] MoS₂, [74] and MoS₂/graphene heterostructures [121]. Another approach is to generate LSPR effects directly in the nanostructured semiconductor sensitizers via carrier doping [122] thereby enhancing their light absorption. For example, in Fe_{1-x}S₂ QD/graphene nanohybrid photodetectors, a strong LSPR effect was induced in the Fe_{1-x}S₂ QDs via carrier doping, resulting in significantly enhanced light absorption in plasmonic Fe_{1-x}S₂ QDs and thereby enhancing responsivity in the Fe_{1-x}S₂ QDs/graphene photodetectors [123-125]. Similarly, LSPR can be induced in the TMDC NDs in the TMDC-NDs/graphene nanohybrids. Interestingly, SERS sensitivity considerably higher than that of the AuNP/graphene SERS substrates was achieved on TMDCNDs/graphene [126]. In the TMDC-ND/graphene nanohybrid photodetectors, a seven-fold enhancement in the photoresponsivity was achieved with respect to the counterpart with a TMDC continuous layer

sensitizer [47]. These results illustrate that coupling plasmons and excitons can provide an effective scheme to enhance the light absorption of the thin sensitizers in the sensitizer/graphene nano hybrids using either metallic plasmonic nanostructures or LSPR in the semiconductor nanostructure sensitizers. A question arises as to whether these two approaches could be combined to yield further enhanced light absorption and device performance of the TMDC/graphene nano hybrid photodetectors. Also, microcavity can increase of the optical field inside a resonant cavity, giving rise to increased absorption in low dimensional materials [127].

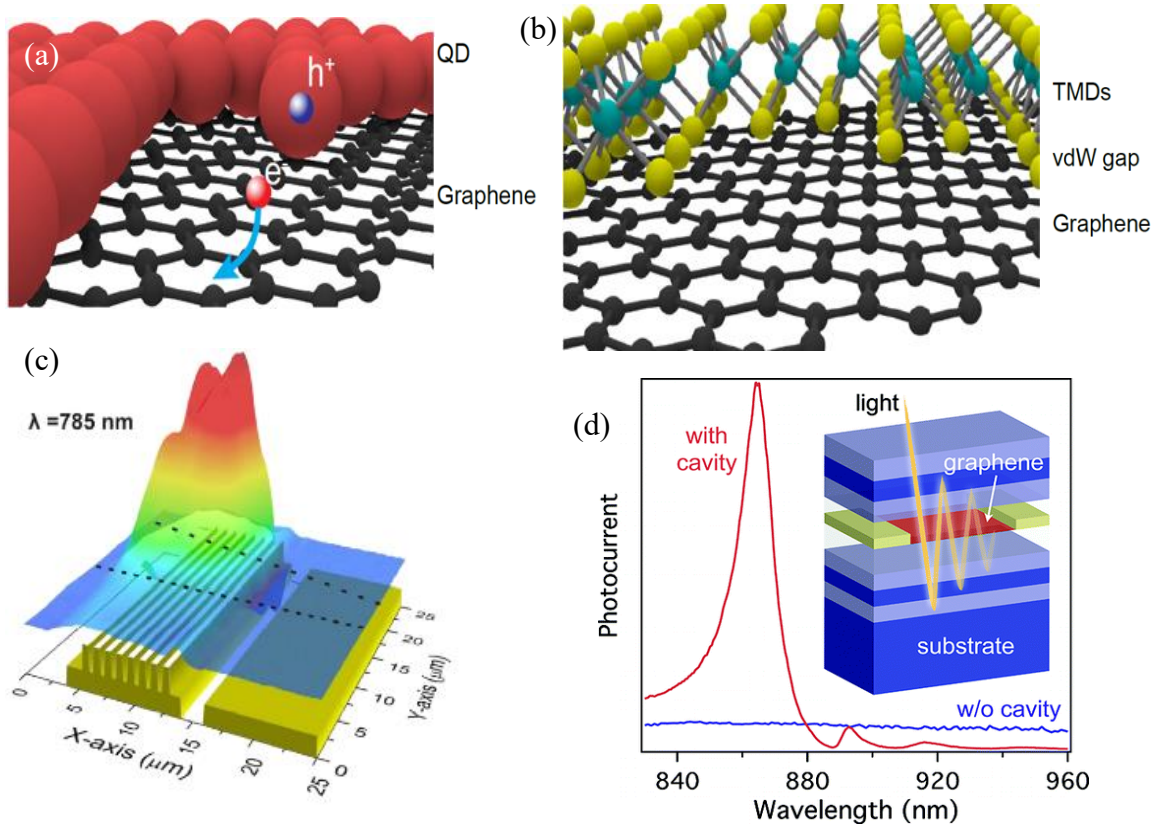


Figure 5.1.1 (a) QD/graphene hybrid and (b) TMDCs /graphene vdW) heterostructures [114]. (c) Scanning photovoltage maps for excitations at 785 nm [120] (d) Spectral response of graphene device integrated with a Micro-optical-cavity [127].

5.2 WS₂ Nano Disk/Graphene on plasmonic Ag Nanoparticles for Photodetection

In this work, we explore integration of the two approaches. Specifically, a graphene/WS₂-ND heterostructure was transferred on a AgNP-metafilm consisting of a layer of AgNPs embedded in a 20 nm thick SiO₂ overlayer, [128] aiming to further enhance the optical absorption and hence the photoresponse of the graphene/WS₂-ND/AgNP-metafilm photodetector. A key step is the development of a new process to obtain the transferrable graphene/WS₂-ND heterostructures, which has resolved the issue of the AgNP-metafilm degradation during the WS₂-ND growth through exposure to sulfur vapor at elevated temperatures. The obtained transferrable graphene/WS₂-NDs heterostructures are intact with comparable optoelectronic performance to their counterpart obtained through layer-by-layer growth of WS₂-NDs on graphene using the CVD. This process was further developed to transfer the graphene/WS₂-NDs on a variety of substrates including SiO₂/Si with prefabricated Au electrodes and the AgNP-metafilm located in the channel between the electrodes. In the obtained graphene/WS₂-ND/AgNP-metafilm nanohybrid photodetectors, the strong plasmon–exciton coupling is illustrated through broadband enhancement of light absorption and photoresponsivity in the spectral range of 400–700 nm, with a maximum 5-fold enhancement in the photoresponsivity at the LSPR frequency (~442 nm) of the AgNP-metafilm compared with reference devices of the graphene/WS₂-NDs without the AgNP metafilm.

5.2.1 Results and Discussions

Figure 5.2.2 compares the photocurrents measured on the graphene/WS₂-ND photodetectors with (red) and without (black) the AgNP-metafilm under the illumination of 450 nm wavelength selected to be near the LSPR frequency of the AgNP-metafilm. The light intensity was 0.15

mW/cm² and the source–drain bias was 0.8 V. Remarkably, the photocurrent is enhanced by about five times in the graphene/WS₂-NDs with the AgNP-metafilm as compared to its counterpart without the AgNP-metafilm, which can be ascribed to the LSPR effect of the AgNP-metafilm. The t_{rise} and t_{fall} are 0.3 and 1.0 s for the graphene/WS₂-ND photodetector with the AgNP-metafilm, while shorter t_{rise} and t_{fall} of 0.1 and 0.2 s were observed on its counterpart without the AgNP-metafilm. The longer $t_{\text{rise}} \sim 0.3\text{s}$ and $t_{\text{fall}} \sim 1.0\text{ s}$ together with the asymmetry of the dynamic response in the graphene/WS₂-ND/AgNP-metafilm photodetector could be attributed to unfavorable residual contamination at the graphene/WS₂-ND interface left during the graphene transfer on the WS₂-NDs and the second transfer of the graphene/WS₂-NDs on the AgNP-metafilm. While further investigation is necessary, this argument is consistent with the trend that shorter response times can be obtained on the similar samples with cleaner interfaces [47, 94, 115]. For example, in the graphene/WS₂-ND vdW heterostructure photodetectors with the WS₂-NDs directly grown on graphene, $t_{\text{rise}} \sim 10\text{ ms}$ and $t_{\text{fall}} \sim 20\text{ ms}$ were obtained [47]. On the graphene/WS₂-ND photodetectors with graphene transferred on WS₂-NDs, longer response times of $t_{\text{rise}} \sim 100\text{ ms}$ and $t_{\text{fall}} \sim 200\text{ ms}$ (black curve in Figure 5.2.2) are about an order of magnitude larger. Since AgNPs degrade under the growth condition for WS₂-NDs, an additional transfer of the graphene/WS₂-NDs by dissolving the SiO₂ layer on the SiO₂/Si substrate was employed in this work to transfer the graphene/WS₂-ND assembly on the AgNP-metafilm. This additional transfer can certainly introduce more residues of chemicals to the graphene/WS₂-ND nanohybrid interface, which is most likely responsible for the further increased response times to $t_{\text{rise}} \sim 300\text{ ms}$ and $t_{\text{fall}} \sim 1000\text{ ms}$ as well as the asymmetry of the dynamic response due to the charge trapping at the interface (red curve in Figure 5.2.2). This result therefore indicates that further research to improve the graphene/WS₂-ND interface is important and could lead to higher device performance. Figure

5.2.1 illustrates dynamic responses of the photocurrent of the graphene/WS₂-ND/AgNP-metafilm photodetector at three illumination wavelengths of 650, 550, and 450 nm. It is noticed that the amplitude of the photocurrent is the highest at the 450 nm illumination, which is anticipated from the peak at ~450 nm in the spectral photoresponsivity shown in Figure 5.2.2a with the AgNP-metafilm due to the plasmonic light trapping by the AgNP-metafilm. In addition, the higher photocurrent amplitude at 650 nm, as compared to that at 550 nm, can also be attributed to the broad plasmonic peak at ~650 nm in Figure 5.2.2b. At these three wavelengths, the t_{rise} and t_{fall} are comparable in the range of 0.3–1 s, respectively.

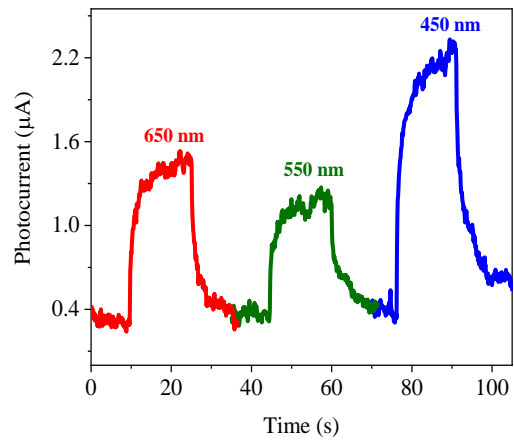


Figure 5.2.1 Dynamic photocurrent in response to light on/off with three incident light wavelengths of: 650 nm (red), 550 nm (green), and 450 nm (blue).

The photoresponsivity (R) is defined as $R = \frac{I_{\text{ph}}}{P_{\text{in}}}$, where I_{ph} is the photocurrent ($I_{\text{ph}} = I_{\text{light}} - I_{\text{dark}}$), and P_{in} is the illumination power. In Figure 5.2.2b, the spectral photoresponsivity of the two devices is compared in the visible wavelength range from 400 nm to 750 nm. For the

graphene/WS₂-NDs/AgNPs-metafilm photodetector (red), the overall photoresponsivity in this spectrum range exhibits an obvious enhancement as compared to that of the counterpart device without the AgNPs-metafilm (black). The enhanced photoresponsivity in the graphene/WS₂-NDs/AgNPs-metafilm photodetector can be attributed to the strong LSPR effect that originates from the AgNPs-metafilm. There are two peaks in the spectral responsivity of this sample. The higher peak observed in the wavelength range of ~400-475 nm is around the LSPR wavelength (~ 442 nm) of the AgNPs-metafilm can be directly ascribed to the LSPR effect of the AgNPs-metafilm on the absorption enhancement of the WS₂-NDs. This leads to the highest enhancement factor of ~ 5 times as shown in Figure 5.2.2b. This enhancement is anticipated from the LSPR effect of the AgNPs-metafilm and confirms the LSPR evanescent field generated by the AgNPs-metafilm is indeed coupled effectively to the graphene/WS₂-NDs in the close proximity. In addition, a second peak of the responsivity at around 650 nm also exhibits a considerable enhancement of ~ 2.7 times. This could be attributed to the large lateral size distribution of the AgNPs to allow the LSPR benefit to be extended to longer wavelengths (see more details in the FDTD simulation below) and the higher external quantum efficiency nearer the band gap of the WS₂-NDs. It should be realized that the band gap E_g for the few-layer WS₂ is 1.94 eV, which typically is observed as a shoulder in the absorption spectrum in the range of 640–700 nm (see Figure 5.2.2a). At longer wavelengths beyond the band gap cutoff of the WS₂-NDs, their light absorption decreases significantly, which seems consistent with the significantly reduced response at longer wavelengths beyond the cutoff at around 640–700 nm. Therefore, our results have demonstrated that the AgNP-metafilm can significantly enhance light absorption and hence broadband photoresponse over wavelengths from 400 to 700 nm through generation of a strong LSPR evanescent field using the AgNP-metafilm around the WS₂-NDs. Note that the SEM in Figure 5.2.2b shows a wide distribution of lateral

dimensions (20–120 nm) and shapes of the AgNPs. In the simulation, the AgNPs were treated as semispheres with diameters in the range of 20–120 nm or radius in the range of 10–60 nm to illustrate their broadband LSPR effect.

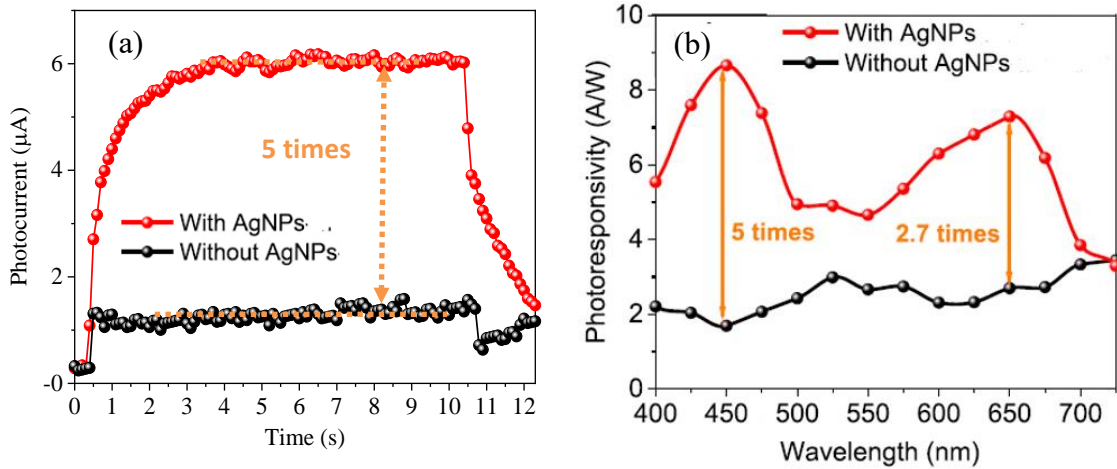


Figure 5.2.2 (a) Photocurrent response of the photodetectors with (red) and without (black) AgNPs-metofilm at 450 nm and light intensity of 0.15 mW/cm² under 0.8V bias. (b) Photoresponsivity as a function of wavelength for graphene/WS₂-NDs photodetector photodetectors with (red) and without (black) the AgNPs-metofilm. The source-drain bias voltage was 0.8V for both devices.

Figure 5.2.3a depicts photoresponsivity as a function of the 450 nm illumination power. The highest photoresponsivities are 11.7 and 3.5 A/W, respectively, at the lowest incident power of 5.5×10^{-8} W for the graphene/WS₂-ND/AgNP-metofilm and graphene/WS₂-ND photodetectors. The photoresponsivity of both devices decreases monotonically with increasing illumination power, due to the higher quantum efficiencies from lower e-h pair recombination at lower illumination powers. However, the graphene/WS₂-ND/AgNP-metofilm device exhibits overall higher

responsivity in this illumination power range than its counterpart without the AgNP-metofilm. This can be seen clearly from the enhancement factors, defined as the ratio of the photoresponsivities of the graphene/WS₂-ND photodetectors with and without the AgNP-metofilm (Figure 5.2.3b). The spectral photocurrent enhancement factor of the two devices, which is derived from the ratio between the black and red curves in Figure 5.2.2b, is displayed in Figure 5.2.3c. Quantitatively, the enhancement factor varies between the maximum value of 5 at around 450 nm near the LSPR peak of the AgNP-metofilm (442 nm) and the minimum value of 1.6 (525 nm) at the valley between the two peaks in Figure 5.2.2b. The smaller peak of the enhancement factor at around 650 nm may be explained by the fast fall of light absorption at longer wavelengths beyond the cutoff of WS₂ (on the right side of the peak) and the increasing quantum efficiency as the incident illumination wavelength is approaching the cutoff (from the left side of the peak).

The external quantum efficiency (EQE) and detectivity as a function of wavelength of graphene/WS₂-NDs/AgNPs-metofilm nanohybrid photodetectors are plotted in Figure 5.2.3d. The

EQE is defined as $EQE = \frac{(I_{ph}/e)}{(P_{in}/h\nu)}$, where h is the Planck constant, ν is the frequency of

incident light, and e is the electron charge. The detectivity (D^*) can be defined as $D^* = \frac{A^{1/2}}{NEP} =$

$R A^{1/2}/i_n^{2^{1/2}}$ where A is the active area of the photodetector, NEP is the noise equivalent power,

and i_n^2 is the noise current. With the assumption that the noise limiting the detectivity is dominated by shot noise from the dark current I_{dark} in graphene channel, the detectivity can be given by

Equation 6. The maximum EQEs and D^* of 2390% and 4.3×10^{10} Jones are found at the wavelength of 450 nm.

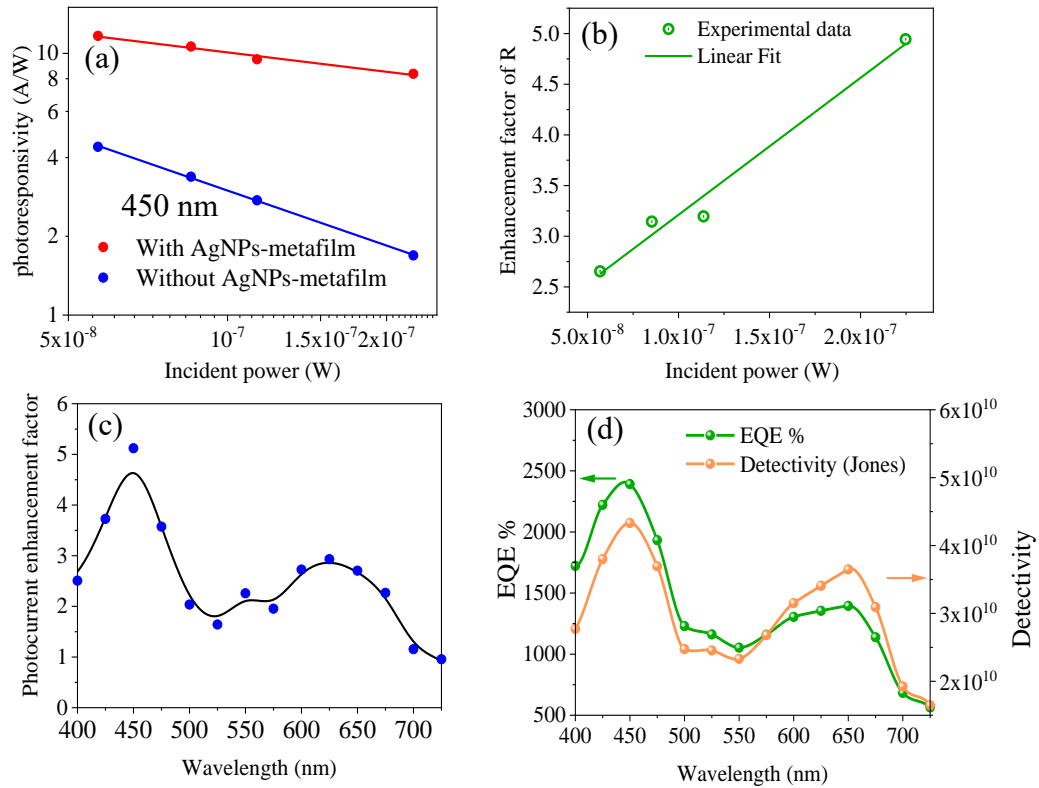


Figure 5.2.3 (a) photoresponsivity of graphene/WS₂-NDs photodetectors with (red) and without (blue) the AgNPs-metafilm at different intensities of the 450 nm illumination. The source-drain bias was 0.8 V. (b) Photoresponsivity enhancement as a function of light intensity. (c) Photocurrent enhancement as a function of wavelength. (d) The measured external quantum efficiency (EQE) and detectivity D^* as a function of the wavelength under $V_{sd} = 0.8V$.

In Figure 5.2.4, the photoresponsivity of the graphene/WS₂-ND/AgNP-metafilm photodetector was measured under different incident power (5.5×10^{-8} , 8.5×10^{-8} , and 1.2×10^{-7} W) and different bias voltages (0.4, 0.6, and 0.8 V) with 450 nm illumination. The measured photoresponsivity increases monotonically with the bias voltage at all different illumination powers and decreases with increasing the illumination power.

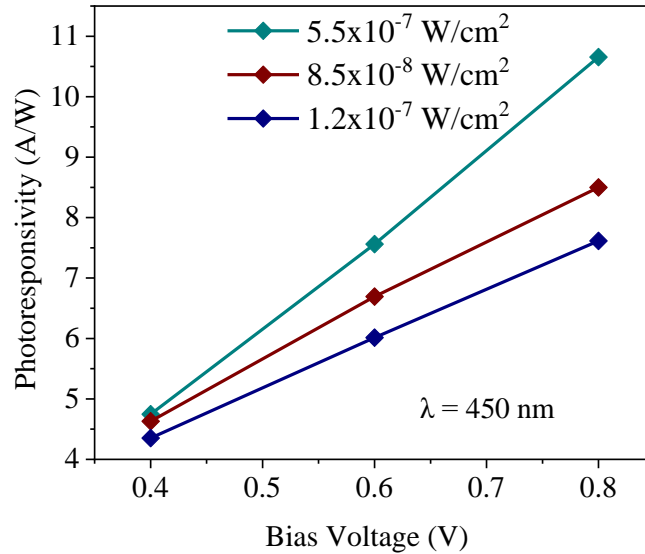


Figure 5.2.4 Photoresponsivity of graphene/WS₂-NDs/AgNPs-metafilm nano hybrid photodetectors at different irradiated power and different bias voltages, $\lambda=450$ nm.

To further study the impact of plasmonic effects, FDTD simulations were carried out on AgNPs. For simplicity, the AgNPs were treated as semispheres with diameters in the range of 20–120 nm or radius in the range of 10–60 nm considering the wide distribution of lateral dimension (20–120 nm) and shapes of AgNPs revealed in SEM analysis in Figure 2.2.6b. To see how such a feature plays a key role in the enhancement of photoresponsivity reported in Figure 5.2.2b, we used FDTD simulation (Lumerical) to study the plasmonic mode profiles and absorption cross sections of AgNPs with different lateral sizes. The system considered in this paper is schematically shown in Figure 5.2.5a based on the device structure shown in Figure 2.2.3e. The structure includes a semispherical AgNP with radius r on a glass substrate. The AgNPs are considered to be embedded in a silica layer, and on the top, there is a thin layer with a thickness (D) of 6 nm. This layer has

an effective refractive index of 4.5 and effectively represents the top WS₂-NDs and graphene. It should be realized that the dimension of the WS₂-NDs may correlate to their optical properties and affect the graphene/WS₂-ND photodetector's spectral range and responsivity. A future research on such an effect of the WS₂-ND dimension will be interesting to both understanding the underlying physics and facilitating the practical applications of the WS₂-NDs.

The results of the calculations for the absorption cross section are shown in Figure 5.2.5b. For small r , e.g., $r = 10$ nm (solid line), the absorption contains a single peak at about 520 nm. As the size of the AgNP increases, this peak is red-shifted as another peak is formed at a shorter wavelength. For $r = 60$ nm (dashed-dotted line), the spectrum includes two peaks with a main broad peak at 685 nm and another peak at 465 nm. Therefore, the spectrum seen in Figure 2.2.6a (graphene/ WS₂ ND/AgNP-metafilm) is the result of a weighted average of the spectra seen in Figure 5.2.5b, considering the size distribution of the AgNPs (Figure 2.2.6b). Considering the results shown in Figure 5.2.5b, we believe that the photoresponsivity presented in Figure 3b is the result of plasmonic enhancement of optical excitation at two major wavelength ranges [129-132]. The first happens around the band gap of WS₂-NDs and can be involved with the interband excitons. The second occurs at the upper band edge (or excited states above the band gap) of the WS₂-NDs, close to the overall major plasmonic peak of the AgNP-metafilm seen in Figure 2.2.6a (or that of graphene/WS₂- ND/AgNP-metafilm), i.e., at 450 nm. In this wavelength range, one expects that the plasmon field enhancement promotes excitation of the electron/hole pairs [131, 132]. Considering the wide ranges of AgNP sizes (20–120 nm), as shown in Figure 2.2.6b, the contributions of the stronger peaks beyond 520 nm in Figure 5.2.5b are most probably suppressed to some extent by the relatively smaller number of AgNPs with larger sizes. Despite this, since such peaks are quite broad, their presence can explain the broad spectrum of graphene/WS₂-

ND/AgNP metafilm in Figure 2.2.6a (purple line), particularly the feature on its longer wavelength side. On the other hand, such a peak can be associated with the combined contribution of the main peaks around 520 and the secondary peaks of the larger AgNPs around 450 nm seen in Figure 5.2.6b. This may explain the slope of the shorter wavelength side of the peak seen in Figure 2.2.6a (purple line). Of course, in terms of the overall wavelength, there are some discrepancies between the simulation results and those presented in Figure 2.2.6. A main reason for this is the fact that we approximated the shapes of the AgNPs as semispheres.

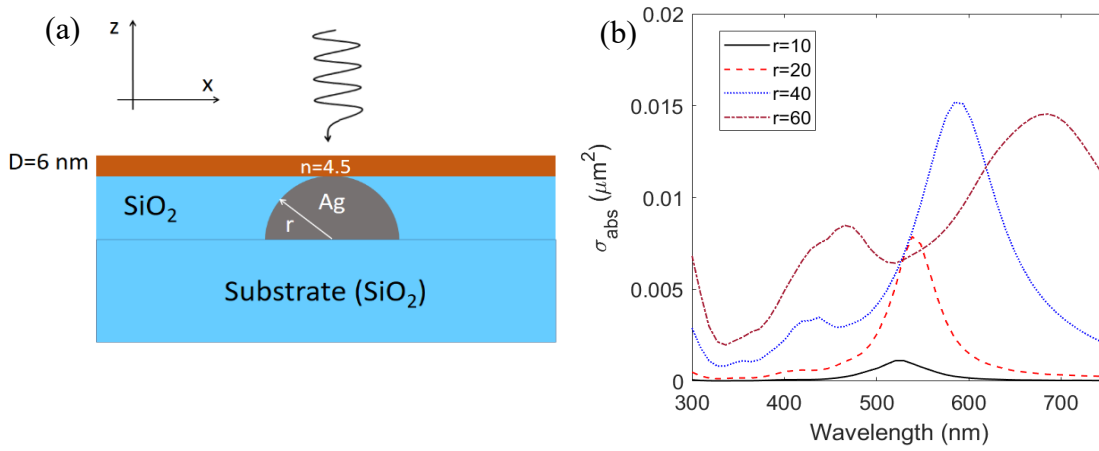


Figure 5.2.5 (a) Diagram of the structure adopted for FDTD simulations of plasmonic response of the AgNP. The AgNP (semisphere) has the radius of r and embedded on SiO_2 . The thin layer on the top with thickness of $D=6$ nm represents the WS_2 -ND and graphene. (b) Absorption cross section of the structure shown in (a) for different radius values of 10,20,40, and 60 nm of the AgNP, r (legends in nm).

To see this better, in Figure 5.2.6 we show the mode profiles of the structure for $r = 60$ and 10 nm. Here, a and b refer to the profiles for $r = 60$ nm and at 685 and 465 nm, respectively. Figure 5.2.6c shows the mode profile for $r = 10$ nm at 520 nm. Note that in all of these cases we consider the incident beam is polarized along the x axis (Figure 5.2.5). The results represented in Figure 5.2.6 offer two main observations. The first is the fact that the upper thin layer ($D = 6$ nm), which represents the WS_2 -NDs and graphene, pulls the plasmonic modes of the AgNP-metafilm upward.

The second observation is the penetration of the plasmonic field into this layer. The combination of these two suggests that the AgNP-metafilm with 60 nm radius can support the plasmonic enhancement of the optical excitations of the WS₂-NDs at 685 nm, [129] which contributes to the photoresponsivity rise at 650 nm. Additionally, the plasmon modes of such AgNPs at 465 nm can also support formation of the peak of the photoresponsivity seen at 450 nm (Figure 5.2.2b). The photoresponsivity peak at 450 nm is also promoted by the AgNP-metafilm with smaller sizes. In fact, as shown in Figure 5.2.6c, for $r = 10$ nm, the plasmon mode penetration into the WS₂-NDs is expected to be significant.

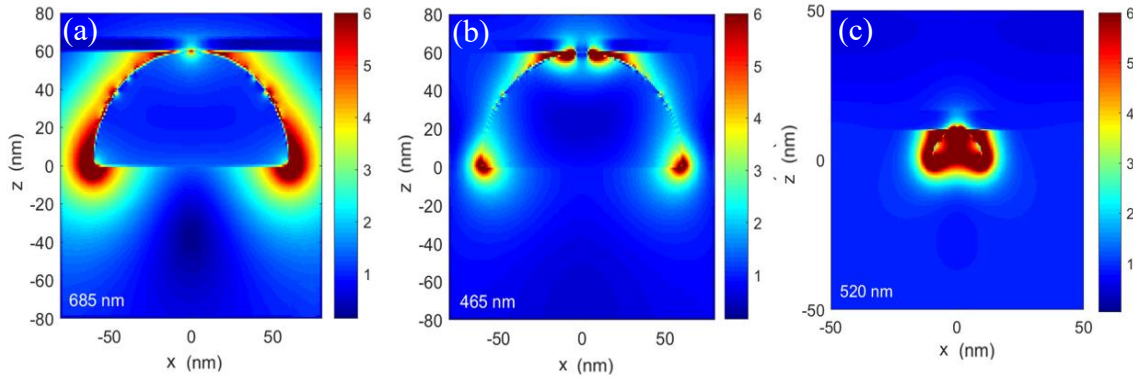


Figure 5.2.6 FDTD simulated electromagnetic field mode profiles of a AgNP with $r = 60$ nm (a, b) and 10 nm (c).

5.2.2 Conclusion

In summary, a graphene/WS₂-ND/AgNP-metafilm vdW heterostructure nanohybrid has been developed in this work to enable a strong exciton–plasmon coupling. This nanohybrid integrates a nonmetallic plasmonic WS₂-ND/graphene vdW heterostructure with a metallic plasmonic AgNP-metafilm for superposition of the plasmonic-enhanced absorption of visible light. A critical step in this integration is the development of a process for fabrication of the transferrable

graphene/WS₂-ND nanohybrids that can be transferred on to the AgNP-metafilm. This can prevent degradation of the LSPR effect of the AgNPmetafilm from the contamination by the sulfur vapor required for the growth of the WS₂-NDs. In the obtained graphene/ WS₂-ND/AgNP-metafilm heterostructures, the controlled spacing of ~20 nm between graphene/WS₂-NDs and the AgNP-metafilm by the SiO₂ overlayer on the AgNPs allows effective coupling of excitons generated upon light illumination in the WS₂-NDs and the plasmonic evanescent EM field in the vicinity of the AgNP-metafilm, resulting in a significantly enhanced photoresponsivity. Under the light illumination of 450 nm of an incident power of 5.5×10^{-8} W, high photoresponsivity of 11.7 A/W, EQE of 2390%, and detectivity D* of 4.3×10^{10} Jones have been obtained at a bias voltage of 0.8 V, which represent a significant improvement over that of the counterpart devices without the plasmonic AgNP-metafilm. For example, the responsivity of the former is more than five times of that on the latter, confirming that a significantly enhanced light absorption can be achieved by integrating the graphene/WS₂-NDs and AgNP-metafilm in the graphene/ WS₂-ND/AgNP-metafilm heterostructure nanohybrids. Considering that both WS₂-NDs (or in general TMDC-NDs)/graphene and AgNP-metafilm can be obtained using chemical or physical vapor deposition in wafer size as illustrated in this work, the developed approach is promising for the practical photodetectors and other optoelectronic applications.

6 Chapter 6: Enhanced H₂ sensitivity in ultraviolet-activated Pt nanoparticle/SWCNT /graphene nanohybrids

6.1 An Overview of Carbon nanostructure-based gas sensor

Carbon nanostructures, especially CNTs and graphene, are promising for gas sensing [133-136] due to their unique physical properties including high electron mobility and large specific surface area [137, 138]. This has motivated an intensive effort in designing various three-dimensional (3D) electrodes based on carbon nanostructures to achieve a large specific sensor area with highly efficient charge transfer and transport for high sensitivity [134, 139, 140]. Various gas sensors based on carbon nanostructures have been developed for detecting different gases such as H₂, NO₂, and NH₃ with promising performance [135, 141, 142].

H₂ sensing is an important research topic in gas sensing due to the safety concerns with H₂ gas storage and utilization. H₂ concentrations higher than 4% are flammable and explosive [135, 136, 143]. Therefore, developing highly sensitive H₂ sensors is indispensable for H₂-related applications. For H₂ gas sensing, a strong interaction between the CNTs and H₂ gas is necessary for efficient H₂ detection. However, un-functionalized CNTs only weakly interact with H₂ gas molecules [133]. In order to enhance the interaction with H₂ gas molecules at the CNT surface, integration of metal catalytic NPs such as palladium (Pd) [134, 144, 145] and platinum (Pt) [135, 136] has been exploited to improve the H₂ sensitivity. The role of metal NPs is to facilitate H₂ molecules adsorbing via two different mechanisms, namely physisorption and chemisorption (physical and chemical adsorption) [136]. In the former, hydrogen molecules bound to CNTs by weak vdW forces. In contrast, in chemisorption, they are bond to the metal NPs by strong covalent bonds. In the case of Pt-NPs, the adsorbed H₂ molecules dissociate on the Pt-NPs surface and

lower the work function to facilitate electron transfer from the Pt-NPs to the CNTs thus lowering the resistance of CNTs [146]. For example, D. Jung *et al*, fabricated semiconducting SWCNTs decorated with Pt-NPs and obtained H₂ responsivity up to ~ 9% at H₂ concentration of 10%, in contrast to a negligible H₂ response on the counterpart devices without Pt-NPs due to the poor interaction of H₂ molecules with the SWCNT [146].

It should be noted that various molecules, including those in ambient conditions and processing chemicals, can adsorb readily on the carbon nanostructures of the gas sensors. For example, O₂ molecules in air adsorb onto SWCNTs with a binding energy of ~ 0.28 eV, leading to a significant amount of charge transfer to the SWCNTs [147]. The O₂ adsorption not only induces electronic structure change via hole doping, but also affects H₂ interaction with the carbon surface, resulting in degraded H₂ sensitivity and response speed [148-151]. Thermal annealing is commonly used to remove O₂ and other molecular adsorbates from the surface of carbon nanostructures [149-151]. For example, S. Chen *et al*, used vacuum-annealing by heating graphene up to 150 °C for 2 hours to get rid of adsorbed molecules on Gr [150]. Photo-induced removal of adsorbed molecules on graphene or CNTs offers an alternative approach over the thermal annealing since it is convenient and could be non-destructive [151-153].

6.2 Ultraviolet-activation improved H₂ gas sensing using ALD Pt decorated 3D carbon nanostructures

Here, we explore C-band ultraviolet (UVC) irradiation for non-destructive activation of a 3D SWCNT film/graphene electrode decorated with Pt-NPs using conformal atomic layer deposition (Pt-NPs/SWCNTs/graphene) for H₂ sensing. The focus of this study is to understand the effectiveness of UVC irradiation on desorbing the adsorbed molecules from the carbon

nanostructure surface for further enhancement of the H₂ sensor performance in terms of both sensitivity and response time. By varying the UVC exposure times in the range of 0-20 minutes, an interesting trend of improved performance of both responsivity and response speed with UVC exposure time in the short time range, followed with an opposite trend after the peak performance at 10 minutes UVC exposure was observed. Remarkably, the enhancement of the H₂ gas response up to 4.3 times together with the reduction of the response time by 3.6 times were achieved with the Pt-NPs/SWCNTs/ graphene H₂ sensor after the UVC irradiation.

The responsivity of the ALD Pt-NPs/SWCNT/graphene H₂ gas sensor was measured after exposing it to UVC radiation for 0, 2, 5, 10, 15, and 20 minutes. The responsivity is defined from the relative change of resistance using the following equation:

$$\text{Responsivity } (\Delta R/R_0\%) = \frac{R-R_0}{R_0} \times 100 \quad (18)$$

where R_0 and R are the resistances of the sensor before and after the exposure to H₂, respectively [154].

6.2.1 Results and Discussions

Figure 6.2.1a compares the dynamic resistance change normalized to the original resistance ($\Delta R/R_0$) of the Pt-NPs/SWCNTs/graphene sensor in response to 10% of H₂ concentration before (black) and after (colored) the sensor was exposed to the UVC radiation for different periods up to 20 minutes. The electric bias voltage across the sensor was maintained at 0.1 V. Interestingly, both H₂ sensitivity and response speed were improved dramatically after the UVC irradiation. For short (up to 10 minutes) exposures to the UVC irradiation, the H₂ sensitivity increases monotonically with the UVC exposure time. The H₂ gas sensitivity was increased by a maximum of 430 % after the device was exposed to UVC light for 5 minutes (blue). This sensitivity was

maintained when extending the UVC exposure time to 10 minutes (green) while the response speed was further enhanced. This improvement may be attributed to SWCNT surface activation most likely due to the desorption of residual molecules from the SWCNT surface by the UVC photons. This increases the effective sensing surface area and therefore the H₂ response. Longer UV exposure times of the Pt-NPs/SWCNTs/graphene sensors, however, yield a reduced H₂ sensitivity. As we shall discuss later, this may be ascribed to the degradation of the carbon nanostructures by high-energy UVC photons. Nevertheless, the improved H₂ sensitivity of the Pt-NPs/SWCNTs/graphene device, even after UVC irradiation for 15-20 minutes is still considerably higher by a factor of 2 as compared to that of the as-synthesized device. Figure 6.2.1b illustrates the H₂ sensitivity as function of the UVC irradiation time (blue) for the Pt-NPs/SWCNTs/graphene sensors. Overall, the sensitivity was improved after the UVC irradiation.

Besides the sensitivity, the response speed is also affected by the UVC irradiation as shown in Figure 6.2.1b. In order to quantify this, the response time, defined as the time required to reach 70% of the maximum resistance change, was calculated from the dynamic response shown in Figure 6.2.1a [155]. Figure 6.2.1b shows the response time of the Pt-NPs/SWCNTs/graphene sensor as function of the UVC irradiation time (red). The response time for the as-synthesized Pt-NPs/SWCNTs/graphene sensor is around 15 minutes. With increasing UVC irradiation time up to 10 minutes, the time constant decreases monotonically to about 4.2 minutes, which represents 3.6 times improvement over that for the as-synthesized counterparts. At longer UVC irradiation times of 15 and 20 minutes, the time constants of 4.4 and 10.5 minutes, respectively, remain considerably better than that of the as-synthesized Pt-NPs/SWCNTs/graphene sensors. The trend of the H₂ sensitivity and response time as functions of the UVC irradiation time in Figure 6.2.1b raises a question on the underlying microscopic mechanism associated with the UVC irradiation on carbon

nanostructures such as SWCNTs and graphene. It should be noted that the UVC photons carry high energies. For example, in the UVC spectrum of 280-100 nm wavelengths, the photon energy is in the range of 4.43-12.4 eV. This means that the UVC light used in this work with wavelengths of 254 nm and 185 nm can not only induce residual molecules desorption from surface of the carbon nanostructures, or SWCNTs and graphene specifically [156-160], but also break the carbon-carbon bonds of ~ 4.9 eV [161] in the carbon nanostructures to activate the carbon nanostructure surface for improved H_2 sensitivity. However, the UV light of 360 nm - 400 nm (in UVA band) was found to not be effective for activation of the Pt-NPs/SWCNTs/graphene sensors since the improvement of the sensitivity and response speed is negligible. Considering the photon energy up to 3.44 eV in this UVA light is adequate for residual molecule desorption while inadequate to affect the carbon-carbon bonds, the improved H_2 sensing performance of the Pt-NPs/SWCNTs/graphene sensors suggests that the additional surface activation of the SWCNTs surface by the UVC irradiation is important to the H_2 sensing.

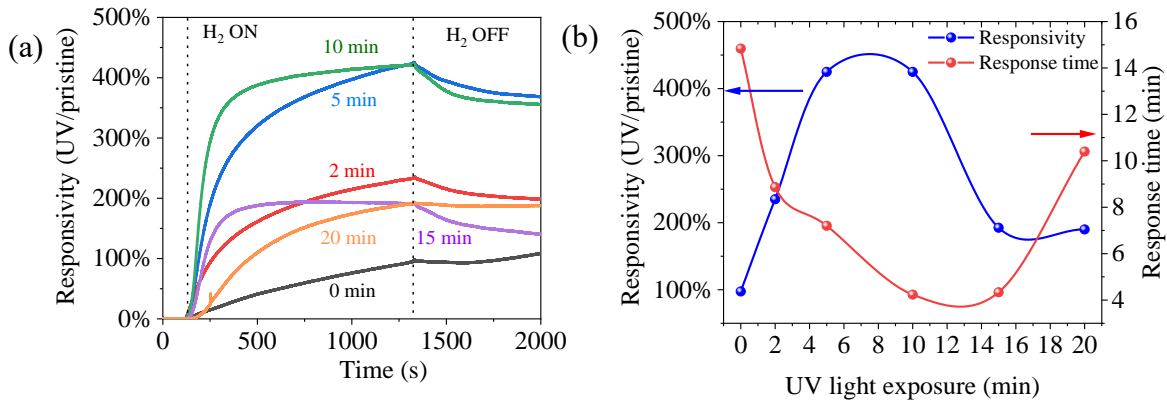


Figure 6.2.1 (a) The normalized dynamic H_2 response (responsivity (UV/pristine)) of the Pt-NPs/SWCNTs/graphene gas sensor as function of UV light exposure at room temperature before (black) and after UV irradiation for different time of 2, 5, 10, 15, and 20 minutes. (b) The maximum response (blue) and response time as a function of UV light exposure time.

The fabricated device was exposed to different concentrations of H₂ gas at room temperature to demonstrate its sensing performance. Figure 6.2.2a shows the dynamic response of H₂ gas sensor to H₂ at five different concentrations of H₂ gas. The responsivity of the Pt-NPs/SWCNTs/graphene sensor increases linearly with the increasing H₂ concentration from 1% to 10% as shown in Figure 6.2.2b, which is desirable for high sensitivity H₂ detection. The decrease in sensitivity with decreasing H₂ concentration is due to the reduction of the number of the H₂ molecules absorbed on the Pt-NPs/SWCNTs/graphene sensors [162]. Detecting lower concentrations was restricted by our instrument. However, the sensitivity to 1% H₂ concentration by the Pt-NPs/SWCNTs/graphene sensors is already lower than the threshold of inflammable H₂ concentration of 4% [143].

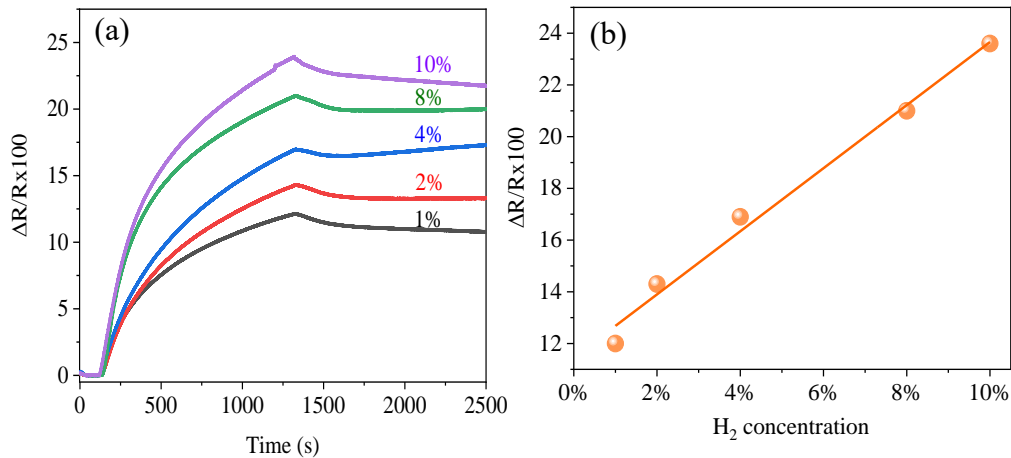


Figure 6.2.2 (a-b) Sensitivity of Pt-NPs @ SWCNTs/graphene H₂ gas sensor as a function of the H₂ concentration ranging from 1% to 10%.

Figure 6.2.3a, illustrates the dynamic response of a Pt-NPs/SWCNTs/graphene to 10% of H₂ gas. The responsivity was measured when the device was freshly prepared without UVC irradiation (black) and after exposed to ambient conditions for 50 days (red). The H₂ responsivity reduced slightly after exposure to ambient conditions for about 50 days. This is most probably due to the

adsorption of air molecules on the active sensor surface. This argument is supported by the improved performance of the aged device using UVC irradiation. Interestingly, the H₂ response of the device was restored and even improved by the UVC irradiation for 2 (blue) and 5 minutes (green) as shown in Figure 6.2.3a and b. In fact, the responsivity of the device was improved after the UVC irradiation for 2 and 5 minutes by 20% and 53%, respectively, as compared to the responsivity of the device after being stored in ambient environment for 50 days (red). This can be attributed to the desorption of the air molecules attached during the sensor storage in air for 50 days (minor) and residual molecules attached to the pristine Pt-NPs/SWCNTs/graphene sensor (major).

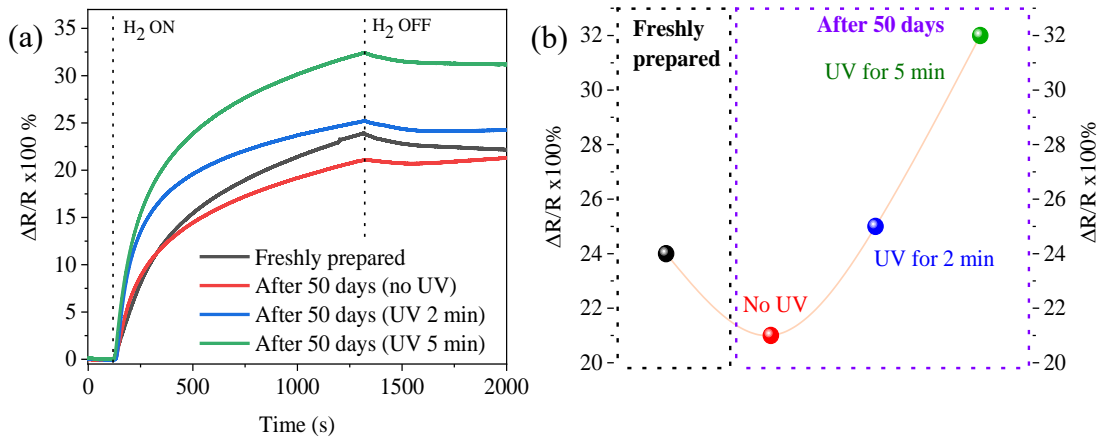


Figure 6.2.3 (a) Dynamic H₂ Response of the Pt-NPs/SWCNTs/Gr gas sensor as function of UV light exposure at room temperature before (black) and after UV irradiation for different time of 2, 5, 10, 15, and 20 minutes.

Figure 6.2.4 provides an experimental confirmation of this hypothesis through a set of Raman spectra taken on SWCNTs and graphene. In order to delineate the UV irradiation effect on SWCNTs and Gr, Raman spectra were collected separately on them as function of UVC irradiation times. Figure 6.2.4a compares the Raman spectra taken on an SWCNT film after UVC irradiation

for different periods. Overall, no significant change was observed after the UVC irradiation except a moderate enhancement of the 2D peak at 2692.5 cm^{-1} with increasing UVC irradiation time up to 10 minutes. Figure 6.2.4b displays Raman spectra of graphene after UVC exposure of different periods. From the Raman spectra, graphene maintains its high quality after the UV exposure for 2 and 5 minutes (negligible I_D/I_G ratio). However, a pronounced increase in D peak intensity was observed with 10 minutes UVC irradiation which indicates the formation of defects on graphene with excessive UV irradiation at > 5 minutes. The source of defects may include formation of amorphous carbon on the graphene lattice and the chemisorption of oxygen atoms onto dangling carbon bonds on graphene at the sites the carbon-carbon bonds are broken [163]. A monotonic increase in the amount of defects was observed as the time of UVC exposure is further increased. The D peak is remarkably increased when graphene was exposed to UVC for 15 and 20 minutes. A small additional D+G peak at $\sim 2935\text{ cm}^{-1}$ can be observed after UVC exposure for 10 minutes and increases at longer exposure times of the UVC light. The presence of this peak is also ascribed to the formation of defects on graphene particularly by oxidation [163-166]. Therefore, since there is a minor adverse effect on the quality of the main sensing material of SWCNT films in our devices, the degradation of graphene is the major reason responsible for the degradation of the Pt-NPs/SWCNTs/graphene sensor's performance at > 10 minutes UV irradiation. This result, on the other hand, has revealed the critical importance of graphene in the 3D SWCNTs/graphene electrode for charge carrier transfer and transport. While the degradation of carrier mobility by UVC irradiation on graphene can be avoided by controlling the UVC irradiation time, this result also indicates that further improvement of the ALD Pt-NPs/SWCNTs/graphene sensor's performance could be achieved by improving the carrier mobility of the CVD graphene via eliminating various charge scattering mechanisms.

In order to quantify the UVC irradiation effect on SWCNTs and graphene, the ratio of the I_D to I_G was calculated and the result is depicted in Figure 6.2.4c-d. In short, the I_D/I_G ratio of the SWCNTs increases slightly from 0.88 before UVC irradiation to 0.92 after 10 minutes of UVC irradiation, indicative of negligible damage of the SWCNTs by the UVC irradiation (Figure 6.2.4c). With a further increase of the UVC exposure time to 15-20 minutes, the I_D/I_G ratio experienced an abrupt increase to 0.12 at 15 and 20 minutes, suggesting increased damage of the UVC on the SWCNTs. Nevertheless, the I_D/I_G ratios remain fairly low in the range of 0.8-0.12, which means that only a small number of defects were formed on SWCNTs due to the UV irradiation. This is in contrast to the dramatic increase of the I_D/I_G ratio (blue) in graphene (Figure 6.2.4d). From 0-5 minutes UVC irradiation, the I_D/I_G ratio of Gr is around 0.7. It increases to 1.1 and 3.3 at 10 and 15 minutes UVC irradiation, respectively, indicative of considerable defect formation in graphene under the UVC irradiation. The I_D/I_G intensity ratio in graphene increases exponentially to 3.3 at 15 minutes and decreased to 2 after 20 minutes because the D peak intensity is saturated and the G peak is still increasing. Concurrently, the I_{2D}/I_G ratios (red in Figure 6.2.4d) of graphene decreased monotonically from 1.8 to 0.1 after UVC irradiation for 0 to 20 minutes and the curve could be fitted approximately by a linear line. This confirms the graphene degradation under the UVC irradiation of 20 minutes. It should be pointed out that the damage of graphene in the ALD Pt-NPs/SWCNTs/graphene sensors would be significantly lower since graphene is protected by the SWCNTs as shown in Figure 6.2.4b. This seems consistent with the H_2 sensitivity in exceeding 197% remained after the UV irradiation of 20 minutes shown in Figure 6.2.4b.

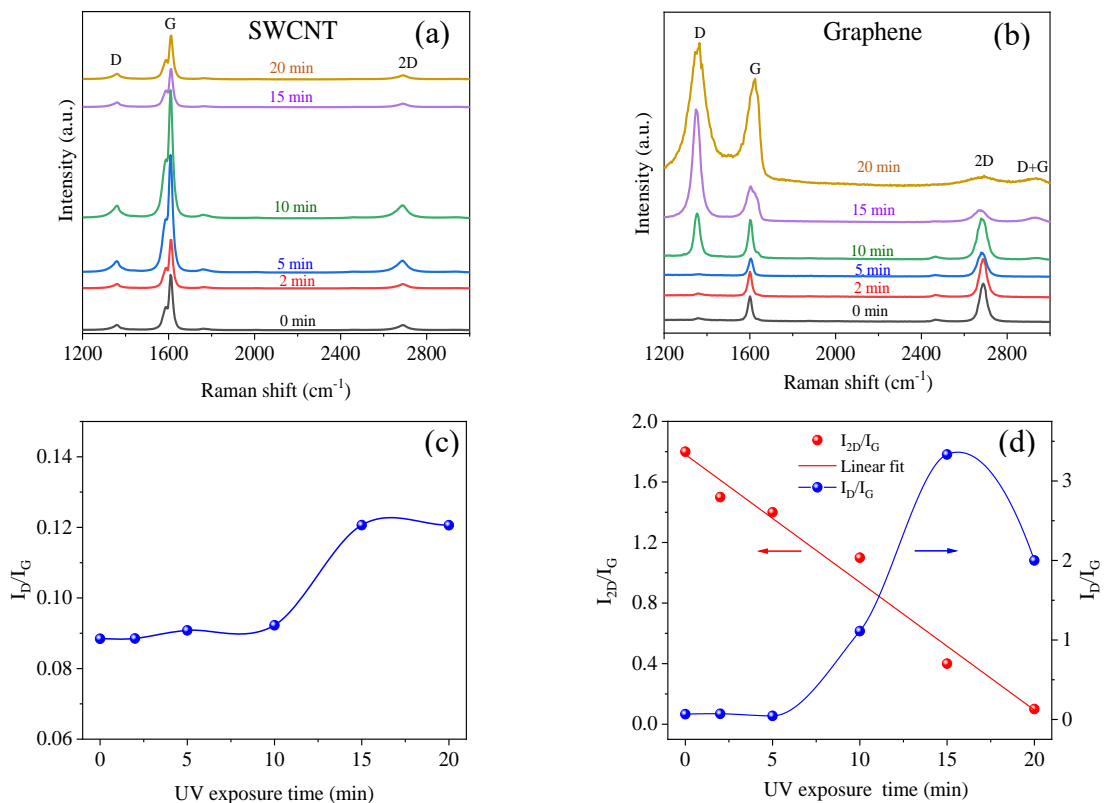


Figure 6.2.4 Raman spectra of (a) SWCNT film and (b) graphene after different UVC irradiation for different periods of 2, 5, 10, 15 and 20 minutes. (c) The I_D/I_G ratio as function of the UVC irradiation time on SWCNTs (d) The I_{2D}/I_G (red) and I_D/I_G (blue) ratio as function of the UVC irradiation time on graphene.

Figure 6.2.5a,b illustrate schematically the effect of the UVC irradiation. The residual molecules, such as O₂ and H₂O, attach to the surface of SWCNTs and graphene in ambient conditions with weak binding energy ~ 0.28 eV typical to physisorption [147]. The desorption of these residual molecules at the initial stage of the UVC irradiation increases the specific sensor area, resulting in much enhanced H₂ sensitivity as shown in Figure 6.2.1 and Figure 6.2.3. Microscopically, the UVC-assisted photodesorption of residual molecules may be attributed to photo-activated plasmons in SWCNTs and possibly in graphene [154]. Plasmon excitation breaks the adsorbed residual molecule–CNT (or graphene) binding energy and results in residual molecule desorption

[57]. It should be noted that O_2 molecules can also adsorb on the Pt-NPs surface and react with H atoms to form water molecules [133]. The removal of the residual molecules on the surface of the carbon nanostructures also leads to considerably enhanced response speed in H_2 sensing most likely through reduction of the charge scattering and trapping in carbon nanostructures by the adsorbed residual molecules [34, 167]. An excessive UVC irradiation beyond the optimal point of thorough removal of residual molecules may further activate the carbon nanostructures by breaking the carbon-carbon bonds, and therefore facilitate defect formation and possible oxidation in SWCNTs and graphene as shown schematically in Figure 6.2.5c. It should be realized that minor oxidization of the SWCNTs could enhance the curvature of SWCNTs and consequently promote the weak physisorption of H_2 molecules [168], resulting in improved sensor performance. This argument seems to be consistent with the considerable H_2 sensing performance of the Pt-NPs/SWCNTs/graphene sensors after the UVC irradiation, in contrast to a negligible effect by the UVA irradiation. However, graphene plays a critical role in charge transport in the 3D SWCNTs/graphene electrode, the defect formation and oxidation under extensive UVC irradiation would result in decreased charge carrier mobility of graphene due to increased carrier scattering and charge recombination. Consequently, this will lead to reduced H_2 sensitivity of the Pt-NPs/SWCNTs/graphene sensors with the UVC irradiation for > 10 minutes as illustrated in Figure 6.2.5a.

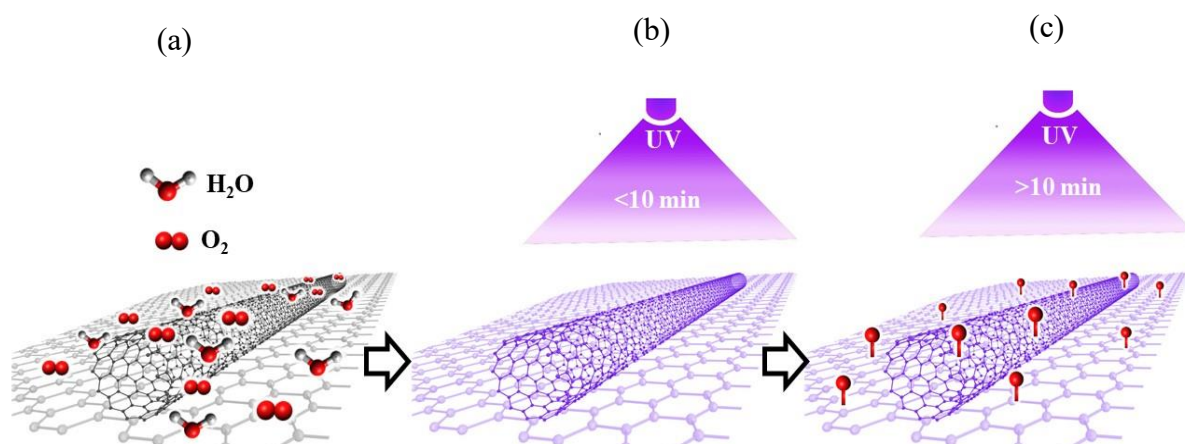


Figure 6.2.5 Schematic illustration of photo-activated desorption of residual molecules, such as O₂ and H₂O, molecules from the SWCNTs and graphene with (a) zero (b) less than 10 minutes, and (c) more than 10 minutes of the UVC irradiation. In the case (c), oxidation of SWCNTs and graphene is illustrated with defects formation and oxygen (red spheres) binding to SWCNTs and graphene.

To further understand the mechanism that how UV worked on the CNT film, we took the X-ray photoelectron spectroscopy (XPS) measurement on two SWCNT/graphene samples of which one is as prepared and the other is after UV irradiation. Figure 6.2.6 shows the full XPS spectral of these two samples and C 1s and O 1s peaks were observed on both samples. Figure 6.2.6 b and c are high resolution scan of C 1s peak. A C 1s peak fitting was done using CasaXPS in order to extract binding information of C and results are also shown Figure 6.2.6 9b and c, respectively. It should be noted that XPS won't be able to detect physical adsorbed small molecules such as H₂O and O₂, since high energy X-ray photons will serve the similar function to remove these adsorbed molecules from CNT surface as UV does. The O 1s peak and C-O, C=O and O-C=O bonds appeared in XPS spectral are speculated from polymer molecules resided on the SWCNT surface during fabrication. For example, C-O bonds in possibly from Triton-X 100 molecule while C=O

and O-C=O are possible originates from MCE membrane used in vacuum filtration, based on their molecule structure. The result clearly shows that the percentage of all carbon-oxygen bonds are reduced after UV irradiation, indicating that the surface polymer molecules are partially removed by UV, which seems in accordance with early reports.[169, 170] The removal of polymers residues exposes more surfaces to the H₂ molecule when in detection thus contributes to the enhanced hydrogen detectivity.

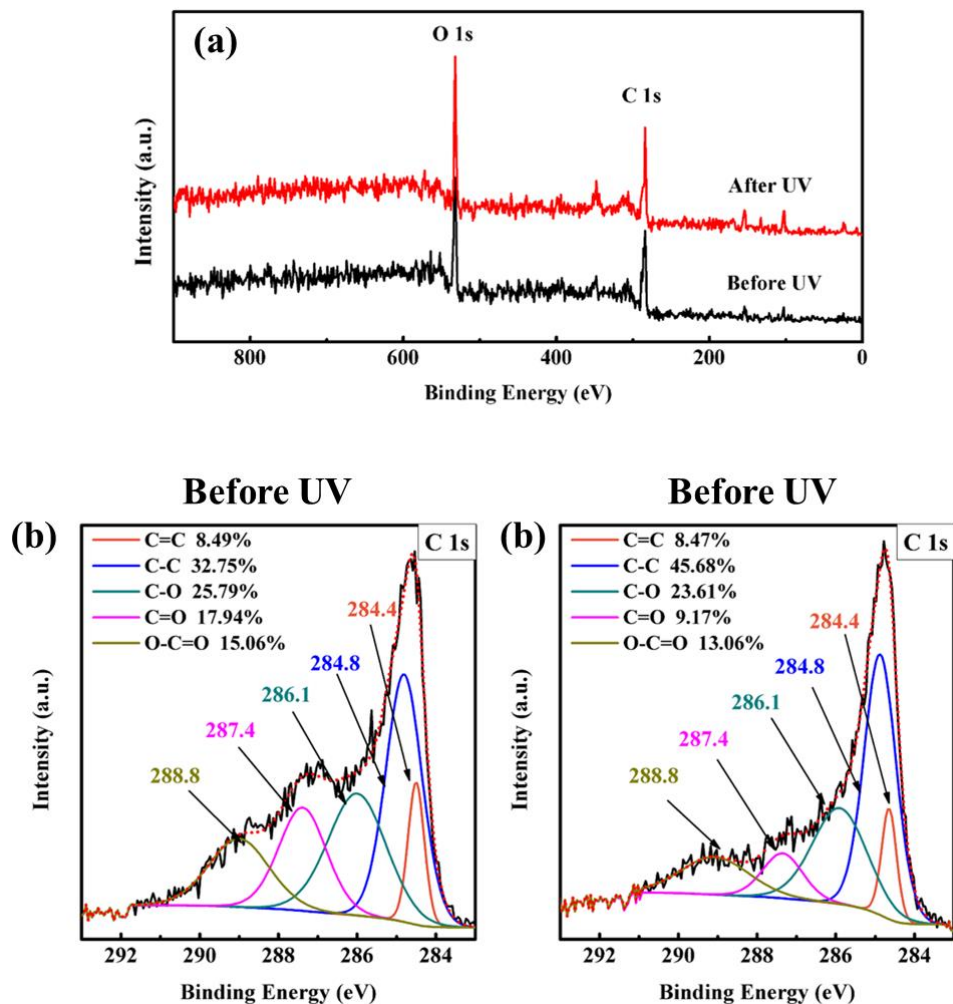


Figure 6.2.6 (a) XPS spectra taken on SWCNT/graphene samples without (black) and with (red) UV irradiation treatment. (b) and (c) are C 1s peak high-resolution scan on the two SWCNT/graphene samples. Red dashed lines represent the fitted C 1s peaks, and the C 1s peak.

6.2.2 Conclusion

In summary, a new process to activate SWCNT and graphene surface using UVC (185 nm and 254 nm) light irradiation has been developed to enhance the performance of the Pt-NPs/SWCNTs/graphene H₂ gas sensors. By varying the UVC irradiation time in the range of 5-20

minutes at a fixed UVC power of 4.6 mW/cm^2 , a monotonic increase of the H_2 response and response speed has been observed in the UVC irradiation period up to 10 minutes. The best responsivity of $\sim 24\%$ to 10% H_2 concentration was obtained after the Pt-NPs/SWCNTs/graphene was treated with 10 minutes UVC irradiation. In addition, the best response time of ~ 4 minutes was observed after UVC irradiation for 10-15 minutes. Quantitatively, the UVC enhanced H_2 gas responsivity and speed are up to 4.3 times and 3.6 times larger, respectively, as compared to that for the as-synthesized Pt-NPs/SWCNTs/graphene sensors. At longer UVC irradiation times (>10 minutes), graphene has been found to be damaged as confirmed from the increasing defect peak intensity in the Raman spectra of graphene, which is not surprising since the UVC photons have enough energy to overcome carbon-carbon binding energy of 4.9 eV . The formation of defects would reduce the carrier mobility of the graphene and hence H_2 sensitivity, which, on the other hand, illustrates the importance of the graphene in the 3D SWCNTs/graphene electrodes to provide a high-efficiency charge transport channel. In contrast, the defect formation is minimal in SWCNTs under the UVC irradiation up to 20 minutes. Considering the negligible enhancement of the sensor performance by the UVA irradiation, the enhanced performance of the Pt-NPs/SWCNTs/graphene H_2 gas sensors after the UVC irradiation is ascribed to the effective sensor surface activation of the Pt-NPs/SWCNTs by higher energy UVC photons. This result illustrates that the approach of the UVC-assisted activation of the SWCNTs and graphene surfaces provides a feasible and convenient approach towards high-performance in the Pt-NPs/SWCNTs/graphene H_2 gas sensors for practical applications.

7 Chapter 7: Conclusions and future perspectives

VdW heterostructures and hybrid systems of low dimensional materials are very advantageous to improve the efficiency of electronic devices. This thesis revealed that the performance of the devices based on 2D materials can be improved by combining two different materials to form vdW heterostructures.

We utilized 2D MoS₂/graphene vdW heterostructures decorated with plasmonic AuNPs as a novel substrate for Surface-enhanced Raman spectroscopy (SERS). The plasmonic AuNPs and the interlayer interaction between MoS₂ and graphene layers enhanced the Raman scattering of the R6G molecule on the surface of this hybrid system of the heterostructure. The plasmonic AuNPs enhance the evanescent field near the AuNPs (enhance the EM effect) and the 2D MoS₂/graphene vdW heterostructures enhance the CM enhancement through interface interaction of different 2D Materials (MoS₂/graphene). We demonstrated a SERS sensitivity for R6G probe molecules that is an order of magnitude improvement over that on the AuNPs/graphene and AuNPs/MoS₂ counterparts. The R6G sensitivity of 5×10^{-10} M was obtained using resonant excitation of 532 nm, which is also one order of magnitude higher than that reported on the AgNPs/MoS₂ substrate. This enhancement can be attributed to the enhanced dipole–dipole interaction at the Au/MoS₂ interface at large Au thickness as revealed in the DFT simulation. This enhanced interface interaction results in enhanced electron delocalization and hence enhanced CM contribution to Raman signatures of R6G molecules.

Additionally, the TMDCs/graphene heterostructure was also employed for photodetection. For instance, the WS₂/graphene heterostructure exhibited a good performance. Still, light absorption in WS₂/graphene vdW heterostructures is limited because of the small thickness of the WS₂ as the

photosensitizer. To enhance the light absorption in the WS₂, we synthesized plasmonic WS₂ nanodisks in lateral dimension of 200–400 nm and layer number of 4–7 using a layer-by-layer, transfer-free CVD. These small WS₂ nanodisks allows LSPR to be generated upon light illumination and thus photo-doping, enabling enhanced light absorption and consequently photoresponsivity. The WS₂-NDs were synthesized WS₂-NDs were grown directly on transfer-free graphene to obtain a clean vdW WS₂-NDs/graphene interface to facilitate charge transfer. On the WS₂-NDs/graphene photodetectors, enhanced photoresponsivity of the WS₂-NDs/graphene photodetector was increased by about seven times as compared to the continuous WS₂ layer on graphene.

The performance of WS₂-NDs/graphene photodetector was improved through the integration of plasmonic AgNPs for light trapping in the vicinity of the AgNPs to enrich light absorption in the WS₂-NDs in proximity. Therefore, coupling plasmons and excitons can provide an effective approach to enhance the light absorption of the thin sensitizer layers using plasmonic metal nanostructures or LSPR in the semiconductor nanostructure. The LSPR effect of the plasmonic AgNP lead to a considerably enhanced electromagnetic field (evanescent field) around the WS₂-NDs, and hence enhanced light absorption by the WS₂-NDs for improved photocurrent and photoresponsivity. This leads to about 500% enhancement over that of the WS₂-NDs/graphene photodetector without the AgNP. The finite element time-domain simulation of confirmed that the enhancement can be attributed to the enhancement of exciton (electron–hole pair) excitation and exciton–plasmon coupling in the graphene/WS₂-NDs/AgNP-metafilm photodetector.

Owing to the extremely high surface-to-volume ratio, high electron mobility, and the sensitivity of electrical properties to changes in the surroundings, graphene and CNTs are promising candidates for gas sensors. The electrical conductivity of the device channel changes when

exposed to the different target gases as a result of the adsorption of gas molecules inducing the charge transfer between the gas molecules and the carbon nanostructures. It is important to design a sensor that can accurately detect the inflammable, colorless, and odorless H₂ gas. We developed a novel H₂ gas sensor consisting of a SWCNTs/graphene 3D electrode decorated with catalytic Pt-NPs. Atomic layer deposition (ALD) technique was used to allow conformal deposition of Pt-NPs on the surface of SWCNTs/graphene in order to enhance the interaction with H₂ gas molecules. High H₂ response of 32% was obtained. The performance of the device was greatly improved after the UVC irradiation. The H₂ gas response enhancement is up to 4.3 times and the reduction of response time was reduced to 3.6 times as compared to that before UV irradiation. This enhancement is due to the desorption of air molecules adsorbed on the SWCNTs and graphene surfaces when expose to ambient.

Further work is required to optimize the design of optoelectronic devices for higher performance. The limited light absorption of atomically thin 2D materials needs to be enhanced by employing different hybrid systems including combining the advantages of various VdW heterostructures based on 2D materials.

8 References

- [1] K.S. Novoselov, A.K. Geim, S.V. Morozov, D. Jiang, M.I. Katsnelson, I. Grigorieva, S. Dubonos, Firsov, AA, Two-dimensional gas of massless Dirac fermions in graphene, *nature*, 438 (2005) 197-200.
- [2] X. Du, I. Skachko, A. Barker, E.Y. Andrei, Approaching ballistic transport in suspended graphene, *Nature nanotechnology*, 3 (2008) 491-495.
- [3] R.R. Nair, P. Blake, A.N. Grigorenko, K.S. Novoselov, T.J. Booth, T. Stauber, N.M. Peres, A.K. Geim, Fine structure constant defines visual transparency of graphene, *Science*, 320 (2008) 1308-1308.
- [4] A.K. Geim, K.S. Novoselov, The rise of graphene, *Nanoscience and technology: a collection of reviews from nature journals*, World Scientific 2010, pp. 11-19.
- [5] N. Peres, The electronic properties of graphene and its bilayer, *Vacuum*, 83 (2009) 1248-1252.
- [6] K.F. Mak, L. Ju, F. Wang, T.F. Heinz, Optical spectroscopy of graphene: From the far infrared to the ultraviolet, *Solid State Communications*, 152 (2012) 1341-1349.
- [7] C. Lee, X. Wei, J.W. Kysar, J. Hone, Measurement of the elastic properties and intrinsic strength of monolayer graphene, *science*, 321 (2008) 385-388.
- [8] A.A. Balandin, S. Ghosh, W. Bao, I. Calizo, D. Teweldebrhan, F. Miao, C.N. Lau, Superior thermal conductivity of single-layer graphene, *Nano letters*, 8 (2008) 902-907.
- [9] B. Vedhanarayanan, V.K. Praveen, G. Das, A. Ajayaghosh, Hybrid materials of 1D and 2D carbon allotropes and synthetic π -systems, *NPG Asia Materials*, 10 (2018) 107-126.
- [10] C.-M. Tilmaci, M.C. Morris, Carbon nanotube biosensors, *Frontiers in chemistry*, 3 (2015) 59.
- [11] M.-F. Yu, Fundamental mechanical properties of carbon nanotubes: current understanding and the related experimental studies, *J. Eng. Mater. Technol.*, 126 (2004) 271-278.
- [12] X. Lei, T. Natsuki, J. Shi, Q.-Q. Ni, Analysis of carbon nanotubes on the mechanical properties at atomic scale, *Journal of Nanomaterials*, 2011 (2011).
- [13] A. Lekawa-Raus, J. Patmore, L. Kurzepa, J. Bulmer, K. Koziol, Electrical properties of carbon nanotube based fibers and their future use in electrical wiring, *Advanced Functional Materials*, 24 (2014) 3661-3682.
- [14] T. Dürkop, B. Kim, M. Fuhrer, Properties and applications of high-mobility semiconducting nanotubes, *Journal of Physics: Condensed Matter*, 16 (2004) R553.
- [15] S. Berber, Y.-K. Kwon, D. Tománek, Unusually high thermal conductivity of carbon nanotubes, *Physical review letters*, 84 (2000) 4613.
- [16] J.Y. Lee, J.-H. Shin, G.-H. Lee, C.-H. Lee, Two-dimensional semiconductor optoelectronics based on van der Waals heterostructures, *Nanomaterials*, 6 (2016) 193.
- [17] A. Kue, N. Zibouche, T. Heine, How does quantum confinement influence the electronic structure of transition metal sulfides TmS_2 , *Physical Review B*, 83 (2011) 245213.
- [18] G. Eda, S.A. Maier, Two-dimensional crystals: managing light for optoelectronics, *ACS nano*, 7 (2013) 5660-5665.
- [19] D. Lembke, A. Kis, Breakdown of high-performance monolayer MoS_2 transistors, *ACS nano*, 6 (2012) 10070-10075.
- [20] K. Novoselov, A. Mishchenko, A. Carvalho, A.C. Neto, 2D materials and van der Waals heterostructures, *Science*, 353 (2016).

- [21] A.K. Geim, I.V. Grigorieva, Van der Waals heterostructures, *Nature*, 499 (2013) 419-425.
- [22] M. Baranowski, A. Surrente, L. Klopotoski, J. Urban, N. Zhang, D.K. Maude, K. Wiwatowski, S. Mackowski, Y.-C. Kung, D. Dumcenco, Probing the interlayer exciton physics in a MoS₂/MoSe₂/MoS₂ van der Waals heterostructure, *Nano letters*, 17 (2017) 6360-6365.
- [23] X. Hong, J. Kim, S.-F. Shi, Y. Zhang, C. Jin, Y. Sun, S. Tongay, J. Wu, Y. Zhang, F. Wang, Ultrafast charge transfer in atomically thin MoS₂/WS₂ heterostructures, *Nature nanotechnology*, 9 (2014) 682-686.
- [24] M.M. Furchi, A. Pospischil, F. Libisch, J. Burgdörfer, T. Mueller, Photovoltaic effect in an electrically tunable van der Waals heterojunction, *Nano letters*, 14 (2014) 4785-4791.
- [25] P. Rivera, J.R. Schaibley, A.M. Jones, J.S. Ross, S. Wu, G. Aivazian, P. Klement, K. Seyler, G. Clark, N.J. Ghimire, Observation of long-lived interlayer excitons in monolayer MoSe₂-WS₂ heterostructures, *Nature communications*, 6 (2015) 1-6.
- [26] C.R. Dean, A.F. Young, I. Meric, C. Lee, L. Wang, S. Sorgenfrei, K. Watanabe, T. Taniguchi, P. Kim, K.L. Shepard, Boron nitride substrates for high-quality graphene electronics, *Nature nanotechnology*, 5 (2010) 722-726.
- [27] J.S. Ross, P. Rivera, J. Schaibley, E. Lee-Wong, H. Yu, T. Taniguchi, K. Watanabe, J. Yan, D. Mandrus, D. Cobden, Interlayer exciton optoelectronics in a 2D heterostructure p-n junction, *Nano letters*, 17 (2017) 638-643.
- [28] M.-H. Chiu, C. Zhang, H.-W. Shiu, C.-P. Chuu, C.-H. Chen, C.-Y.S. Chang, C.-H. Chen, M.-Y. Chou, C.-K. Shih, L.-J. Li, Determination of band alignment in the single-layer MoS₂/WSe₂ heterojunction, *Nature communications*, 6 (2015) 1-6.
- [29] K. Kośmider, J. Fernández-Rossier, Electronic properties of the MoS₂-WS₂ heterojunction, *Physical Review B*, 87 (2013) 075451.
- [30] M.E. Stewart, C.R. Anderton, L.B. Thompson, J. Maria, S.K. Gray, J.A. Rogers, R.G. Nuzzo, Nanostructured plasmonic sensors, *Chemical reviews*, 108 (2008) 494-521.
- [31] I. Kriegel, F. Scotognella, L. Manna, Plasmonic doped semiconductor nanocrystals: Properties, fabrication, applications and perspectives, *Physics Reports*, 674 (2017) 1-52.
- [32] Q. Liu, Y. Gong, T. Wang, W.-L. Chan, J. Wu, Metal-catalyst-free and controllable growth of high-quality monolayer and AB-stacked bilayer graphene on silicon dioxide, *Carbon*, 96 (2016) 203-211.
- [33] Q. Liu, B. Cook, M. Gong, Y. Gong, D. Ewing, M. Casper, A. Stramel, J. Wu, Printable transfer-free and wafer-size MoS₂/graphene van der Waals heterostructures for high-performance photodetection, *ACS applied materials & interfaces*, 9 (2017) 12728-12733.
- [34] R. Lu, G. Xu, J.Z. Wu, Effects of thermal annealing on noise property and temperature coefficient of resistance of single-walled carbon nanotube films, *Applied Physics Letters*, 93 (2008) 213101.
- [35] Z. Wu, Z. Chen, X. Du, J.M. Logan, J. Sippel, M. Nikolou, K. Kamaras, J.R. Reynolds, D.B. Tanner, A.F. Hebard, Transparent, conductive carbon nanotube films, *Science*, 305 (2004) 1273-1276.
- [36] R. Lu, A. Konzelmann, F. Xu, Y. Gong, J. Liu, Q. Liu, M. Xin, R. Hui, J.Z. Wu, High sensitivity surface enhanced Raman spectroscopy of R6G on in situ fabricated Au nanoparticle/graphene plasmonic substrates, *Carbon*, 86 (2015) 78-85.
- [37] R. Goul, S. Das, Q. Liu, M. Xin, R. Lu, R. Hui, J.Z. Wu, Quantitative analysis of surface enhanced Raman spectroscopy of Rhodamine 6G using a composite graphene and plasmonic Au nanoparticle substrate, *Carbon*, 111 (2017) 386-392.

- [38] G. Xu, J. Liu, Q. Wang, R. Hui, Z. Chen, V.A. Maroni, J. Wu, Plasmonic graphene transparent conductors, *Advanced Materials*, 24 (2012) OP71-OP76.
- [39] G. Deokar, J. Avila, I. Razado-Colambo, J.-L. Codron, C. Boyaval, E. Galopin, M.-C. Asensio, D. Vignaud, Towards high quality CVD graphene growth and transfer, *Carbon*, 89 (2015) 82-92.
- [40] G.B. Barin, Y. Song, I. de Fátima Gimenez, A.G. Souza Filho, L.S. Barreto, J. Kong, Optimized graphene transfer: Influence of polymethylmethacrylate (PMMA) layer concentration and baking time on graphene final performance, *Carbon*, 84 (2015) 82-90.
- [41] B. Marta, C. Leordean, T. Istvan, I. Botiz, S. Astilean, Efficient etching-free transfer of high quality, large-area CVD grown graphene onto polyvinyl alcohol films, *Applied Surface Science*, 363 (2016) 613-618.
- [42] Y.H. Lee, X.Q. Zhang, W. Zhang, M.T. Chang, C.T. Lin, K.D. Chang, Y.C. Yu, J.T.W. Wang, C.S. Chang, L.J. Li, Synthesis of large-area MoS₂ atomic layers with chemical vapor deposition, *Advanced materials*, 24 (2012) 2320-2325.
- [43] W. Zhang, J.K. Huang, C.H. Chen, Y.H. Chang, Y.J. Cheng, L.J. Li, High-gain phototransistors based on a CVD MoS₂ monolayer, *Advanced materials*, 25 (2013) 3456-3461.
- [44] A.R. Botello Méndez, N. Perea López, A.L. Elías Arriaga, V. Crespi, F. López Urías, H. Terrones Maldonado, M. Terrones Maldonado, Identification of individual and few layers of WS₂ using Raman Spectroscopy, (2013).
- [45] R. Saito, Y. Tatsumi, S. Huang, X. Ling, M. Dresselhaus, Raman spectroscopy of transition metal dichalcogenides, *Journal of Physics: Condensed Matter*, 28 (2016) 353002.
- [46] A. McCreary, A. Berkdemir, J. Wang, M.A. Nguyen, A.L. Elías, N. Perea-López, K. Fujisawa, B. Kabius, V. Carozo, D.A. Cullen, Distinct photoluminescence and Raman spectroscopy signatures for identifying highly crystalline WS₂ monolayers produced by different growth methods, *Journal of Materials Research*, 31 (2016).
- [47] M. Alamri, M. Gong, B. Cook, R. Goul, J.Z. Wu, Plasmonic WS₂ Nanodiscs/Graphene van der Waals Heterostructure Photodetectors, *ACS applied materials & interfaces*, 11 (2019) 33390-33398.
- [48] D. Paria, H.-H. Jeong, V. Vadakkumbatt, P. Deshpande, P. Fischer, A. Ghosh, A. Ghosh, Graphene-silver hybrid devices for sensitive photodetection in the ultraviolet, *Nanoscale*, 10 (2018) 7685-7693.
- [49] S. Heeg, R. Fernandez-Garcia, A. Oikonomou, F. Schedin, R. Narula, S.A. Maier, A. Vijayaraghavan, S. Reich, Polarized plasmonic enhancement by Au nanostructures probed through Raman scattering of suspended graphene, *Nano letters*, 13 (2013) 301-308.
- [50] R. Maiti, S. Haldar, D. Majumdar, A. Singha, S. Ray, Hybrid opto-chemical doping in Ag nanoparticle-decorated monolayer graphene grown by chemical vapor deposition probed by Raman spectroscopy, *Nanotechnology*, 28 (2017) 075707.
- [51] G. Prakash, R.K. Srivastava, S.N. Gupta, A. Sood, Plasmon-induced efficient hot carrier generation in graphene on gold ultrathin film with periodic array of holes: Ultrafast pump-probe spectroscopy, *The Journal of Chemical Physics*, 151 (2019) 234712.
- [52] K. Balasubramanian, L. Zuccaro, K. Kern, Tunable Enhancement of Raman Scattering in Graphene-Nanoparticle Hybrids, *Advanced Functional Materials*, 24 (2014) 6348-6358.
- [53] B.G. Ghamsari, A. Olivieri, F. Variola, P. Berini, Enhanced Raman scattering in graphene by plasmonic resonant Stokes emission, *Nanophotonics*, 3 (2014) 363-371.

- [54] Z.J. Wu, A.J. Elliot, G.A. Malek, R. Lu, S. Han, H. Yu, S. Zhao, J.Z. Wu, Integrating atomic layer deposition and ultra-high vacuum physical vapor deposition for in situ fabrication of tunnel junctions, (2014).
- [55] G.A. Malek, E. Brown, S.A. Klankowski, J. Liu, A.J. Elliot, R. Lu, J. Li, J. Wu, Atomic layer deposition of Al-doped ZnO/Al₂O₃ double layers on vertically aligned carbon nanofiber arrays, *ACS applied materials & interfaces*, 6 (2014) 6865-6871.
- [56] A.C. Ferrari, J. Meyer, V. Scardaci, C. Casiraghi, M. Lazzeri, F. Mauri, S. Piscanec, D. Jiang, K. Novoselov, S. Roth, Raman spectrum of graphene and graphene layers, *Physical review letters*, 97 (2006) 187401.
- [57] S. Pyo, J. Choi, J. Kim, A Fully Transparent, Flexible, Sensitive, and Visible-Blind Ultraviolet Sensor Based on Carbon Nanotube–Graphene Hybrid, *Advanced Electronic Materials*, 5 (2019) 1800737.
- [58] S. Piscanec, M. Lazzeri, J. Robertson, A.C. Ferrari, F. Mauri, Optical phonons in carbon nanotubes: Kohn anomalies, Peierls distortions, and dynamic effects, *Physical Review B*, 75 (2007) 035427.
- [59] E.I. Braun, A. Huang, C.A. Tusa, M.A. Yukica, P. Pantano, Use of Raman spectroscopy to identify carbon nanotube contamination at an analytical balance workstation, *Journal of occupational and environmental hygiene*, 13 (2016) 915-923.
- [60] S. Brown, A. Jorio, M. Dresselhaus, G. Dresselhaus, Observations of the D-band feature in the Raman spectra of carbon nanotubes, *Physical Review B*, 64 (2001) 073403.
- [61] L. Deng, R.J. Young, I.A. Kinloch, R. Sun, G. Zhang, L. Noé, M. Monthieux, Coefficient of thermal expansion of carbon nanotubes measured by Raman spectroscopy, *Applied Physics Letters*, 104 (2014) 051907.
- [62] G. Duesberg, I. Loa, M. Burghard, K. Syassen, S. Roth, Polarized Raman spectroscopy on isolated single-wall carbon nanotubes, *Physical review letters*, 85 (2000) 5436.
- [63] B. Liu, M. Alamri, M. Walsh, J.L. Doolin, C.L. Berrie, J.Z. Wu, Development of an ALD-Pt@ SWCNT/Graphene 3D Nanohybrid Architecture for Hydrogen Sensing, *ACS Applied Materials & Interfaces*, (2020).
- [64] M. Fleischmann, P.J. Hendra, A.J. McQuillan, Raman spectra of pyridine adsorbed at a silver electrode, *Chemical physics letters*, 26 (1974) 163-166.
- [65] B. Sharma, R.R. Frontiera, A.-I. Henry, E. Ringe, R.P. Van Duyne, SERS: Materials, applications, and the future, *Materials today*, 15 (2012) 16-25.
- [66] X. Ling, L. Xie, Y. Fang, H. Xu, H. Zhang, J. Kong, M.S. Dresselhaus, J. Zhang, Z. Liu, Can graphene be used as a substrate for Raman enhancement?, *Nano letters*, 10 (2010) 553-561.
- [67] L. Sun, H. Hu, D. Zhan, J. Yan, L. Liu, J.S. Teguh, E.K. Yeow, P.S. Lee, Z. Shen, Plasma modified MoS₂ nanoflakes for surface enhanced Raman scattering, *small*, 10 (2014) 1090-1095.
- [68] Y. Lee, H. Kim, J. Lee, S.H. Yu, E. Hwang, C. Lee, J.-H. Ahn, J.H. Cho, Enhanced Raman scattering of rhodamine 6G films on two-dimensional transition metal dichalcogenides correlated to photoinduced charge transfer, *Chemistry of Materials*, 28 (2016) 180-187.
- [69] J. Lin, L. Liang, X. Ling, S. Zhang, N. Mao, N. Zhang, B.G. Sumpter, V. Meunier, L. Tong, J. Zhang, Enhanced Raman scattering on in-plane anisotropic layered materials, *Journal of the American Chemical Society*, 137 (2015) 15511-15517.
- [70] Y. Zhang, Y. Shi, M. Wu, K. Zhang, B. Man, M. Liu, Synthesis and surface-enhanced Raman scattering of ultrathin SnSe₂ nanoflakes by chemical vapor deposition, *Nanomaterials*, 8 (2018) 515.

- [71] M. Liu, Y. Shi, G. Zhang, Y. Zhang, M. Wu, J. Ren, B. Man, Surface-enhanced Raman spectroscopy of two-dimensional tin diselenide nanoplates, *Applied Spectroscopy*, 72 (2018) 1613-1620.
- [72] S. Xu, S. Jiang, J. Wang, J. Wei, W. Yue, Y. Ma, Graphene isolated Au nanoparticle arrays with high reproducibility for high-performance surface-enhanced Raman scattering, *Sensors and Actuators B: Chemical*, 222 (2016) 1175-1183.
- [73] L. Xu, W.-Q. Huang, W. Hu, K. Yang, B.-X. Zhou, A. Pan, G.-F. Huang, Two-dimensional MoS₂-graphene-based multilayer van der Waals heterostructures: enhanced charge transfer and optical absorption, and electric-field tunable Dirac point and band gap, *Chemistry of Materials*, 29 (2017) 5504-5512.
- [74] P. Chen, H. Qiu, S. Xu, X. Liu, Z. Li, L. Hu, C. Li, J. Guo, S. Jiang, Y. Huo, A novel surface-enhanced Raman spectroscopy substrate based on a large area of MoS₂ and Ag nanoparticles hybrid system, *Applied Surface Science*, 375 (2016) 207-214.
- [75] H. Zhong, R. Quhe, Y. Wang, Z. Ni, M. Ye, Z. Song, Y. Pan, J. Yang, L. Yang, M. Lei, Interfacial properties of monolayer and bilayer MoS₂ contacts with metals: beyond the energy band calculations, *Scientific reports*, 6 (2016) 21786.
- [76] J. Chang, S. Larentis, E. Tutuc, L.F. Register, S.K. Banerjee, Atomistic simulation of the electronic states of adatoms in monolayer MoS₂, *Applied physics letters*, 104 (2014) 141603.
- [77] Y. Bai, L. Yan, J. Wang, L. Su, N. Chen, Z. Tan, Highly reproducible and uniform SERS substrates based on Ag nanoparticles with optimized size and gap, *Photonics and Nanostructures-Fundamentals and Applications*, 23 (2017) 58-63.
- [78] R. Ganatra, Q. Zhang, Few-layer MoS₂: a promising layered semiconductor, *ACS nano*, 8 (2014) 4074-4099.
- [79] J.M. Crowley, J. Tahir-Kheli, W.A. Goddard III, Resolution of the band gap prediction problem for materials design, *The journal of physical chemistry letters*, 7 (2016) 1198-1203.
- [80] M.-K. Chuang, S.-S. Yang, F.-C. Chen, Metal nanoparticle-decorated two-dimensional molybdenum sulfide for plasmonic-enhanced polymer photovoltaic devices, *Materials*, 8 (2015) 5414-5425.
- [81] Y. Tan, L. Ma, Z. Gao, M. Chen, F. Chen, Two-dimensional heterostructure as a platform for surface-enhanced Raman scattering, *Nano letters*, 17 (2017) 2621-2626.
- [82] K. Chang, Z. Mei, T. Wang, Q. Kang, S. Ouyang, J. Ye, MoS₂/graphene cocatalyst for efficient photocatalytic H₂ evolution under visible light irradiation, *ACS nano*, 8 (2014) 7078-7087.
- [83] Y. Zhao, X. Pan, L. Zhang, Y. Xu, C. Li, J. Wang, J. Ou, X. Xiu, B. Man, C. Yang, Dense AuNP/MoS₂ hybrid fabrication on fiber membranes for molecule separation and SERS detection, *RSC advances*, 7 (2017) 36516-36524.
- [84] C. Qiu, H. Zhou, H. Yang, M. Chen, Y. Guo, L. Sun, Investigation of n-layer graphenes as substrates for Raman enhancement of crystal violet, *The Journal of Physical Chemistry C*, 115 (2011) 10019-10025.
- [85] W.-H. Park, Z.H. Kim, Charge transfer enhancement in the SERS of a single molecule, *Nano letters*, 10 (2010) 4040-4048.
- [86] S. Huh, J. Park, Y.S. Kim, K.S. Kim, B.H. Hong, J.-M. Nam, UV/ozone-oxidized large-scale graphene platform with large chemical enhancement in surface-enhanced Raman scattering, *ACS nano*, 5 (2011) 9799-9806.

- [87] H. Meng-Jing, Z. Xian, C. Xiao-Yang, L. Can, L. Zheng-Cao, Z. Zheng-Jun, Preparation of SiO₂@ Au nanorod array as novel surface enhanced Raman substrate for trace pollutants detection, *Chinese Physics B*, 24 (2015) 034203.
- [88] X. Wang, W. Shi, G. She, L. Mu, S. Lee, High-performance surface-enhanced Raman scattering sensors based on Ag nanoparticles-coated Si nanowire arrays for quantitative detection of pesticides, *Applied Physics Letters*, 96 (2010) 053104.
- [89] H. Qiu, Z. Li, S. Gao, P. Chen, C. Zhang, S. Jiang, S. Xu, C. Yang, H. Li, Large-area MoS₂ thin layers directly synthesized on Pyramid-Si substrate for surface-enhanced Raman scattering, *RSC advances*, 5 (2015) 83899-83905.
- [90] H. Xu, J. Wu, Q. Feng, N. Mao, C. Wang, J. Zhang, High responsivity and gate tunable graphene-MoS₂ hybrid phototransistor, *Small*, 10 (2014) 2300-2306.
- [91] L. Wu, L. Qin, Y. Zhang, M. Alamri, M. Gong, W. Zhang, D. Zhang, W.-L. Chan, J.Z. Wu, High-Sensitivity Light Detection via Gate Tuning of Organometallic Perovskite/PCBM Bulk Heterojunctions on Ferroelectric Pb_{0.92}La_{0.08}Zr_{0.52}Ti_{0.48}O₃ Gated Graphene Field Effect Transistors, *ACS applied materials & interfaces*, 10 (2018) 12824-12830.
- [92] G. Konstantatos, M. Badioli, L. Gaudreau, J. Osmond, M. Bernechea, F.P.G. De Arquer, F. Gatti, F.H. Koppens, Hybrid graphene–quantum dot phototransistors with ultrahigh gain, *Nature nanotechnology*, 7 (2012) 363-368.
- [93] W. Zhang, C.-P. Chuu, J.-K. Huang, C.-H. Chen, M.-L. Tsai, Y.-H. Chang, C.-T. Liang, Y.-Z. Chen, Y.-L. Chueh, J.-H. He, Ultrahigh-gain photodetectors based on atomically thin graphene-MoS₂ heterostructures, *Scientific reports*, 4 (2014) 3826.
- [94] M. Gong, Q. Liu, B. Cook, B. Kattel, T. Wang, W.-L. Chan, D. Ewing, M. Casper, A. Stramel, J.Z. Wu, All-printable ZnO quantum dots/graphene van der Waals heterostructures for ultrasensitive detection of ultraviolet light, *ACS nano*, 11 (2017) 4114-4123.
- [95] C. Lan, C. Li, S. Wang, T. He, Z. Zhou, D. Wei, H. Guo, H. Yang, Y. Liu, Highly responsive and broadband photodetectors based on WS₂–graphene van der Waals epitaxial heterostructures, *Journal of Materials Chemistry C*, 5 (2017) 1494-1500.
- [96] M. Kuri, B. Chakraborty, A. Paul, S. Das, A. Sood, A. Das, Enhancing photoresponsivity using MoTe₂-graphene vertical heterostructures, *Applied Physics Letters*, 108 (2016) 063506.
- [97] C. Lan, C. Li, Y. Yin, Y. Liu, Large-area synthesis of monolayer WS₂ and its ambient-sensitive photo-detecting performance, *Nanoscale*, 7 (2015) 5974-5980.
- [98] Z. Yin, H. Li, H. Li, L. Jiang, Y. Shi, Y. Sun, G. Lu, Q. Zhang, X. Chen, H. Zhang, Single-layer MoS₂ phototransistors, *ACS nano*, 6 (2012) 74-80.
- [99] F. Xia, T. Mueller, Y.-m. Lin, A. Valdes-Garcia, P. Avouris, Ultrafast graphene photodetector, *Nature nanotechnology*, 4 (2009) 839-843.
- [100] T. Mueller, F. Xia, P. Avouris, Graphene photodetectors for high-speed optical communications, *Nature photonics*, 4 (2010) 297-301.
- [101] F. Xia, T. Mueller, R. Golizadeh-Mojarad, M. Freitag, Y.-m. Lin, J. Tsang, V. Perebeinos, P. Avouris, Photocurrent imaging and efficient photon detection in a graphene transistor, *Nano letters*, 9 (2009) 1039-1044.
- [102] M. Gong, R. Sakidja, R. Goul, D. Ewing, M. Casper, A. Stramel, A. Elliot, J.Z. Wu, High-performance all-inorganic CsPbCl₃ perovskite nanocrystal photodetectors with superior stability, *ACS nano*, 13 (2019) 1772-1783.
- [103] D. Levy, E. Castellón, *Transparent Conductive Materials: Materials, Synthesis, Characterization, Applications*, John Wiley & Sons 2018.

- [104] L. Turyanska, O. Makarovskiy, S.A. Svatek, P.H. Beton, C.J. Mellor, A. Patanè, L. Eaves, N.R. Thomas, M.W. Fay, A.J. Marsden, Ligand-Induced Control of Photoconductive Gain and Doping in a Hybrid Graphene–Quantum Dot Transistor, *Advanced Electronic Materials*, 1 (2015) 1500062.
- [105] W. Yu, S. Li, Y. Zhang, W. Ma, T. Sun, J. Yuan, K. Fu, Q. Bao, Near-infrared photodetectors based on MoTe₂/graphene heterostructure with high responsivity and flexibility, *Small*, 13 (2017) 1700268.
- [106] S. Ryu, L. Liu, S. Berciaud, Y.-J. Yu, H. Liu, P. Kim, G.W. Flynn, L.E. Brus, Atmospheric oxygen binding and hole doping in deformed graphene on a SiO₂ substrate, *Nano letters*, 10 (2010) 4944-4951.
- [107] Y. Liu, B.N. Shivananju, Y. Wang, Y. Zhang, W. Yu, S. Xiao, T. Sun, W. Ma, H. Mu, S. Lin, Highly efficient and air-stable infrared photodetector based on 2D layered graphene–black phosphorus heterostructure, *ACS applied materials & interfaces*, 9 (2017) 36137-36145.
- [108] B. Sun, T. Shi, Z. Liu, Y. Wu, J. Zhou, G. Liao, Large-area flexible photodetector based on atomically thin MoS₂/graphene film, *Materials & Design*, 154 (2018) 1-7.
- [109] K.I. Bolotin, K.J. Sikes, Z. Jiang, M. Klima, G. Fudenberg, J. Hone, P. Kim, H. Stormer, Ultrahigh electron mobility in suspended graphene, *Solid state communications*, 146 (2008) 351-355.
- [110] X. Liu, J. Hu, C. Yue, N. Della Fera, Y. Ling, Z. Mao, J. Wei, High performance field-effect transistor based on multilayer tungsten disulfide, *ACS nano*, 8 (2014) 10396-10402.
- [111] H. Huang, J. Wang, W. Hu, L. Liao, P. Wang, X. Wang, F. Gong, Y. Chen, G. Wu, W. Luo, Highly sensitive visible to infrared MoTe₂ photodetectors enhanced by the photogating effect, *Nanotechnology*, 27 (2016) 445201.
- [112] D. Shao, J. Gao, P. Chow, H. Sun, G. Xin, P. Sharma, J. Lian, N.A. Koratkar, S. Sawyer, Organic–inorganic heterointerfaces for ultrasensitive detection of ultraviolet light, *Nano letters*, 15 (2015) 3787-3792.
- [113] Y. Gong, Q. Liu, J.S. Wilt, M. Gong, S. Ren, J. Wu, Wrapping cytochrome c around single-wall carbon nanotube: engineered nanohybrid building blocks for infrared detection at high quantum efficiency, *Scientific reports*, 5 (2015) 11328.
- [114] A. De Sanctis, J.D. Mehew, M.F. Craciun, S. Russo, Graphene-based light sensing: fabrication, characterisation, physical properties and performance, *Materials*, 11 (2018) 1762.
- [115] R. Lu, J. Liu, H. Luo, V. Chikan, J.Z. Wu, Graphene/GaSe-nanosheet hybrid: towards high gain and fast photoresponse, *Scientific reports*, 6 (2016) 19161.
- [116] J. He, C. Fan, J. Wang, Y. Cheng, P. Ding, E. Liang, Plasmonic Nanostructure for Enhanced Light Absorption in Ultrathin Silicon Solar Cells, *Advances in OptoElectronics*, (2012).
- [117] D. Schaadt, B. Feng, E. Yu, Enhanced semiconductor optical absorption via surface plasmon excitation in metal nanoparticles, *Applied Physics Letters*, 86 (2005) 063106.
- [118] Y. Liu, R. Cheng, L. Liao, H. Zhou, J. Bai, G. Liu, L. Liu, Y. Huang, X. Duan, Plasmon resonance enhanced multicolour photodetection by graphene, *Nature communications*, 2 (2011) 1-7.
- [119] J. Miao, W. Hu, Y. Jing, W. Luo, L. Liao, A. Pan, S. Wu, J. Cheng, X. Chen, W. Lu, Surface plasmon-enhanced photodetection in few layer MoS₂ phototransistors with Au nanostructure arrays, *small*, 11 (2015) 2392-2398.
- [120] T. Echtermeyer, S. Milana, U. Sassi, A. Eiden, M. Wu, E. Lidorikis, A. Ferrari, Surface plasmon polariton graphene photodetectors, *Nano Letters*, 16 (2016) 8-20.

- [121] M. Alamri, R. Sakidja, R. Goul, S. Ghopry, J.Z. Wu, Plasmonic Au nanoparticles on 2D MoS₂/Graphene van der Waals heterostructures for high-sensitivity surface-enhanced Raman spectroscopy, *ACS Applied Nano Materials*, 2 (2019) 1412-1420.
- [122] J.M. Luther, P.K. Jain, T. Ewers, A.P. Alivisatos, Localized surface plasmon resonances arising from free carriers in doped quantum dots, *Nature materials*, 10 (2011) 361-366.
- [123] M. Gong, D. Ewing, M. Casper, A. Stramel, A. Elliot, J.Z. Wu, Controllable Synthesis of Monodispersed Fe_{1-x}S₂ Nanocrystals for High-Performance Optoelectronic Devices, *ACS applied materials & interfaces*, 11 (2019) 19286-19293.
- [124] M. Gong, R. Sakidja, Q. Liu, R. Goul, D. Ewing, M. Casper, A. Stramel, A. Elliot, J.Z. Wu, Broadband photodetectors enabled by localized surface plasmonic resonance in doped iron pyrite nanocrystals, *Advanced Optical Materials*, 6 (2018) 1701241.
- [125] J.Z. Wu, Explore uncooled quantum dots/graphene nanohybrid infrared detectors based on quantum dots/graphene heterostructures, *Infrared Technology and Applications XLVI*, International Society for Optics and Photonics, 2020, pp. 1140706.
- [126] S.A. Ghopry, M.A. Alamri, R. Goul, R. Sakidja, J.Z. Wu, Extraordinary Sensitivity of Surface-Enhanced Raman Spectroscopy of Molecules on MoS₂ (WS₂) Nanodomes/Graphene van der Waals Heterostructure Substrates, *Advanced Optical Materials*, 7 (2019) 1801249.
- [127] M. Furchi, A. Urich, A. Pospischil, G. Lilley, K. Unterrainer, H. Detz, P. Klang, A.M. Andrews, W. Schrenk, G. Strasser, Microcavity-integrated graphene photodetector, *Nano letters*, 12 (2012) 2773-2777.
- [128] B. Liu, R.R. Gutha, B. Kattel, M. Alamri, M. Gong, S.M. Sadeghi, W.-L. Chan, J.Z. Wu, Using Silver Nanoparticles-Embedded Silica Metafilms as Substrates to Enhance the Performance of Perovskite Photodetectors, *ACS applied materials & interfaces*, 11 (2019) 32301-32309.
- [129] J. Kern, A. Trügler, I. Niehues, J. Ewering, R. Schmidt, R. Schneider, S. Najmaei, A. George, J. Zhang, J. Lou, Nanoantenna-enhanced light-matter interaction in atomically thin WS₂, *Acs Photonics*, 2 (2015) 1260-1265.
- [130] H. Chen, J. Yang, E. Rusak, J. Straubel, R. Guo, Y.W. Myint, J. Pei, M. Decker, I. Staude, C. Rockstuhl, Manipulation of photoluminescence of two-dimensional MoSe₂ by gold nanoantennas, *Scientific reports*, 6 (2016) 22296.
- [131] S.M. Sadeghi, W.J. Wing, R.R. Gutha, R.W. Goul, J.Z. Wu, Functional metal-oxide plasmonic metastructures: Ultrabright semiconductor quantum dots with polarized spontaneous emission and suppressed Auger recombination, *Physical Review Applied*, 11 (2019) 024045.
- [132] W.J. Wing, S.M. Sadeghi, R.R. Gutha, Q. Campbell, C. Mao, Metallic nanoparticle shape and size effects on aluminum oxide-induced enhancement of exciton-plasmon coupling and quantum dot emission, *Journal of applied physics*, 118 (2015) 124302.
- [133] J. García-Aguilar, I. Miguel-García, Á. Berenguer-Murcia, D. Cazorla-Amorós, Single wall carbon nanotubes loaded with Pd and NiPd nanoparticles for H₂ sensing at room temperature, *Carbon*, 66 (2014) 599-611.
- [134] Y. Du, Q. Xue, Z. Zhang, F. Xia, Z. Liu, W. Xing, Enhanced hydrogen gas response of Pd nanoparticles-decorated single walled carbon nanotube film/SiO₂/Si heterostructure, *AIP Advances*, 5 (2015) 027136.
- [135] M.K. Kumar, S. Ramaprabhu, Nanostructured Pt functionlized multiwalled carbon nanotube based hydrogen sensor, *The Journal of Physical Chemistry B*, 110 (2006) 11291-11298.
- [136] A. Kaniyoor, R.I. Jafri, T. Arockiadoss, S. Ramaprabhu, Nanostructured Pt decorated graphene and multi walled carbon nanotube based room temperature hydrogen gas sensor, *Nanoscale*, 1 (2009) 382-386.

- [137] T. Ando, The electronic properties of graphene and carbon nanotubes, *NPG asia materials*, 1 (2009) 17-21.
- [138] V. Meunier, A. Souza Filho, E. Barros, M. Dresselhaus, Physical properties of low-dimensional sp²-based carbon nanostructures, *Reviews of Modern Physics*, 88 (2016) 025005.
- [139] Y. Sun, H.H. Wang, M. Xia, Single-walled carbon nanotubes modified with Pd nanoparticles: unique building blocks for high-performance, flexible hydrogen sensors, *The Journal of Physical Chemistry C*, 112 (2008) 1250-1259.
- [140] J. Li, Y. Lu, Q. Ye, M. Cinke, J. Han, M. Meyyappan, Carbon nanotube sensors for gas and organic vapor detection, *Nano letters*, 3 (2003) 929-933.
- [141] J. Kong, N.R. Franklin, C. Zhou, M.G. Chapline, S. Peng, K. Cho, H. Dai, Nanotube molecular wires as chemical sensors, *science*, 287 (2000) 622-625.
- [142] J.-H. Kim, Q. Zhou, J. Chang, Suspended graphene-based gas sensor with 1-mW energy consumption, *Micromachines*, 8 (2017) 44.
- [143] I. Sayago, E. Terrado, E. Lafuente, M. Horrillo, W.K. Maser, A. Benito, R. Navarro, E. Urriolabeitia, M. Martinez, J. Gutierrez, Hydrogen sensors based on carbon nanotubes thin films, *Synthetic Metals*, 148 (2005) 15-19.
- [144] S. Ju, J.M. Lee, Y. Jung, E. Lee, W. Lee, S.-J. Kim, Highly sensitive hydrogen gas sensors using single-walled carbon nanotubes grafted with Pd nanoparticles, *Sensors and Actuators B: Chemical*, 146 (2010) 122-128.
- [145] J.-H. Lee, W.-S. Kang, C.K. Najeeb, B.-S. Choi, S.-W. Choi, H.J. Lee, S.S. Lee, J.-H. Kim, A hydrogen gas sensor using single-walled carbon nanotube Langmuir–Blodgett films decorated with palladium nanoparticles, *Sensors and Actuators B: Chemical*, 188 (2013) 169-175.
- [146] D. Jung, M. Han, G.S. Lee, Fast-response room temperature hydrogen gas sensors using platinum-coated spin-capable carbon nanotubes, *ACS applied materials & interfaces*, 7 (2015) 3050-3057.
- [147] D.C. Sorescu, K.D. Jordan, P. Avouris, Theoretical study of oxygen adsorption on graphite and the (8, 0) single-walled carbon nanotube, *The Journal of Physical Chemistry B*, 105 (2001) 11227-11232.
- [148] S.-H. Jhi, S.G. Louie, M.L. Cohen, Electronic properties of oxidized carbon nanotubes, *Physical Review Letters*, 85 (2000) 1710.
- [149] R.T. Lu, G.W. Xu, J.Z. Wu, Effects of thermal annealing on noise property and temperature coefficient of resistance of single-walled carbon nanotube films, *Applied Physics Letters*, 93 (2008) 213101.
- [150] S. Chen, W. Cai, D. Chen, Y. Ren, X. Li, Y. Zhu, J. Kang, R.S. Ruoff, Adsorption/desorption and electrically controlled flipping of ammonia molecules on graphene, *New Journal of Physics*, 12 (2010) 125011.
- [151] Y. Miyamoto, N. Jinbo, H. Nakamura, A. Rubio, D. Tománek, Photodesorption of oxygen from carbon nanotubes, *Physical Review B*, 70 (2004) 233408.
- [152] R.T. Lu, J.W. Liu, H.F. Luo, V. Chikan, J.Z. Wu, Graphene/GaSe-Nanosheet Hybrid: Towards High Gain and Fast Photoresponse, *Scientific Reports*, 6 (2016) 19161.
- [153] Y. Zhang, G. Hu, M. Gong, M. Alamri, C. Ma, M. Liu, J.Z. Wu, Lateral Graphene p–n Junctions Realized by Nanoscale Bipolar Doping Using Surface Electric Dipoles and Self-Organized Molecular Anions, *Advanced Materials Interfaces*, 6 (2019) 1801380.
- [154] R.J. Chen, N.R. Franklin, J. Kong, J. Cao, T.W. Tombler, Y. Zhang, H. Dai, Molecular photodesorption from single-walled carbon nanotubes, *Applied Physics Letters*, 79 (2001) 2258-2260.

- [155] M. Zhao, H. Zhu, J. Zhang, M. Li, Z. Cai, Synthesis and gas sensor application of nanostructure Cr₂O₃ hollow spheres, IOP Conference Series: Materials Science and Engineering, IOP Publishing, 2017, pp. 012030.
- [156] L. Yang, M. Ouyang, W.J. Li, X. Han, UV-illumination induced desorption of CNT sensors, 2008 8th IEEE Conference on Nanotechnology, IEEE, 2008, pp. 284-287.
- [157] C.G. Kang, S.K. Lee, S. Choe, Y.G. Lee, C.-L. Lee, B.H. Lee, Intrinsic photocurrent characteristics of graphene photodetectors passivated with Al₂O₃, Optics express, 21 (2013) 23391-23400.
- [158] E.S. Muckley, A.J. Nelson, C.B. Jacobs, I.N. Ivanov, Multimodal probing of oxygen and water interaction with metallic and semiconducting carbon nanotube networks under ultraviolet irradiation, Journal of Photonics for Energy, 6 (2016) 025506.
- [159] G. Chen, T.M. Paronyan, E.M. Pigos, A.R. Harutyunyan, Enhanced gas sensing in pristine carbon nanotubes under continuous ultraviolet light illumination, Scientific reports, 2 (2012) 1-7.
- [160] S.J. Kim, J.-W. Han, B. Kim, M. Meyyappan, Single walled carbon nanotube based air pocket encapsulated ultraviolet sensor, ACS sensors, 2 (2017) 1679-1683.
- [161] K. Erickson, R. Erni, Z. Lee, N. Alem, W. Gannett, A. Zettl, Determination of the local chemical structure of graphene oxide and reduced graphene oxide, Advanced Materials, 22 (2010) 4467-4472.
- [162] L. Hao, Y. Liu, Y. Du, Z. Chen, Z. Han, Z. Xu, J. Zhu, Highly enhanced H₂ sensing performance of few-layer MoS₂/SiO₂/Si heterojunctions by surface decoration of Pd nanoparticles, Nanoscale research letters, 12 (2017) 567.
- [163] F. GÜNEŞ, G.H. Han, H.-J. Shin, S.Y. Lee, M. Jin, D.L. Duong, S.J. Chae, E.S. Kim, F. Yao, A. Benayad, UV-light-assisted oxidative sp³ hybridization of graphene, Nano, 6 (2011) 409-418.
- [164] M. Iqbal, M. Iqbal, M. Khan, J. Eom, Ultraviolet-light-driven doping modulation in chemical vapor deposition grown graphene, Physical Chemistry Chemical Physics, 17 (2015) 20551-20556.
- [165] S. Zhao, S.P. Surwade, Z. Li, H. Liu, Photochemical oxidation of CVD-grown single layer graphene, Nanotechnology, 23 (2012) 355703.
- [166] M.Z. Iqbal, S. Siddique, A. Rehman, Structural defects controlled oxidation of UV irradiated graphene-based field effect transistors, Diamond and Related Materials, 85 (2018) 112-116.
- [167] R. Lu, J.J. Shi, F.J. Baca, J.Z. Wu, High performance multiwall carbon nanotube bolometers, Journal of Applied Physics, 108 (2010) 084305.
- [168] Z.K. Horastani, S.J. Hashemifar, S.M. Sayedi, M.H. Sheikhi, First-principles study of H₂ adsorption on the pristine and oxidized (8, 0) carbon nanotube, international journal of hydrogen energy, 38 (2013) 13680-13686.
- [169] A. Suhail, K. Islam, B. Li, D. Jenkins, G. Pan, Reduction of polymer residue on wet-transferred CVD graphene surface by deep UV exposure, Applied Physics Letters, 110 (2017).
- [170] T. Mukherjee, S.A. Berhe, A. Goswami, O. Chyan, K.J. Singh, I. Brown, UV-assisted modification and removal mechanism of a fluorocarbon polymer film on low-k dielectric trench structure, ACS Appl Mater Interfaces, 7 (2015) 5051-5055.